



ATTITUDE CONTROL OF MULTIPLE RIGID BODY SPACECRAFT WITH FLEXIBLE  
HINGE JOINTS

A THESIS SUBMITTED TO  
THE GRADUATE SCHOOL OF NATURAL AND APPLIED SCIENCES  
OF  
MIDDLE EAST TECHNICAL UNIVERSITY

BY

BURAK AKBULUT

IN PARTIAL FULFILLMENT OF THE REQUIREMENTS  
FOR  
THE DEGREE OF MASTER OF SCIENCE  
IN  
MECHANICAL ENGINEERING

SEPTEMBER 2009

Approval of the thesis:

**ATTITUDE CONTROL OF MULTIPLE RIGID BODY SPACECRAFT WITH  
FLEXIBLE HINGE JOINTS**

submitted by **BURAK AKBULUT** in partial fulfillment of the requirements for the degree of  
**Master of Science in Mechanical Engineering Department, Middle East Technical Uni-**  
**versity** by,

Prof. Dr. Canan Özgen  
Dean, Graduate School of **Natural and Applied Sciences**

---

Prof. Dr. Süha Oral  
Head of Department, **Mechanical Engineering**

---

Prof. Dr. M. Kemal Özgören  
Supervisor, **Mechanical Engineering Department, METU**

---

Prof. Dr. Ozan Tekinalp  
Co-supervisor, **Aerospace Engineering Department, METU**

---

**Examining Committee Members:**

Prof. Dr. Reşit Soylu  
Mechanical Engineering Department, METU

---

Prof. Dr. M. Kemal Özgören  
Mechanical Engineering Department, METU

---

Prof. Dr. Ozan Tekinalp  
Aerospace Engineering Department, METU

---

Prof. Dr. Kemal İder  
Mechanical Engineering Department, METU

---

Asst. Prof. Dr. Yiğit Yazıcıoğlu  
Mechanical Engineering Department, METU

---

**Date:**

---

**I hereby declare that all information in this document has been obtained and presented in accordance with academic rules and ethical conduct. I also declare that, as required by these rules and conduct, I have fully cited and referenced all material and results that are not original to this work.**

Name, Last Name: BURAK AKBULUT

Signature :

# **ABSTRACT**

## **ATTITUDE CONTROL OF MULTIPLE RIGID BODY SPACECRAFT WITH FLEXIBLE HINGE JOINTS**

Akbulut, Burak

M.S., Department of Mechanical Engineering

Supervisor : Prof. Dr. M. Kemal Özgören

Co-Supervisor : Prof. Dr. Ozan Tekinalp

September 2009, 101 pages

Control algorithm is developed for a satellite with flexible appendages to achieve a good pointing performance. Detailed modeling activity was carried out that consists of sensor and actuator models, disturbances and system dynamics. Common hardware found in the spacecraft such as reaction wheels, gyroscopes, star trackers etc. were included in the model. Furthermore, the Newton-Euler method is employed for the derivation of multi-body equations of motion. Evaluation of the pointing accuracy with proper pointing performance metrics such as accuracy, jitter and stability during slew maneuvers are obtained through simulations. Control strategies are proposed to improve pointing performance.

**Keywords:** Attitude Control, Multi-body Dynamics, Pointing Accuracy, Spacecraft Jitter

# ÖZ

## ESNEK MAFSALLARA SAHİP ÇOK CİSİMLİ BİR UZAY ARACININ YÖNELİM KONTROLÜ

Akbulut, Burak

Yüksek Lisans, Makina Mühendisliği Bölümü

Tez Yöneticisi : Prof. Dr. M. Kemal Özgören

Ortak Tez Yöneticisi : Prof. Dr. Ozan Tekinalp

Eylül 2009, 101 sayfa

Esnek mafsallarla bağlanmış uzuvlara sahip bir uyduda uygun bir yönelim başarımı sağlanması için kontrol algoritması geliştirilmiştir. Ayrıntılı bir modelleme çalışması yapılmış; algılayıcılar, eyleticiler, saptırıcı girdiler ve sistem dinamiği modellenmiştir. Uzay araçlarında sıklıkla bulunan tepki tekerleri, jiroskoplar, yıldız izlerler vb. gibi donanımlar modele dahil edilmiştir. Ayrıca, çok cisimli hareketlilik denklemlerinin elde edilmesi için Newton-Euler yöntemi kullanılmıştır. Yönelim hassasiyetinin değerlendirilmesi; hassasiyet, titreşim ve kararlılık gibi uygun yönelim başarımı ölçütlerinin dönme manevrası benzetimlerinde elde edilmeleriyle gerçekleştirilmiştir. Yönelim başarımını geliştirecek kontrol stratejileri önerilmiştir.

Anahtar Kelimeler: Yönelim Kontrolü, Çok Cisimli Dinamik, Yönelim Hassasiyeti, Uzay Aracı Titreşimleri

*To my family...*

## ACKNOWLEDGMENTS

First and foremost, my deepest gratitudes go to my supervisor Prof. Dr. Kemal Özgören and co-supervisor Prof. Dr. Ozan Tekinalp for their unrelenting support and encouragement.

My family is the integral part of my accomplishments. I would like to thank my father for the 23 chromosomes he provided and my mother for the rest, which probably included the gene for stubbornness. Of course I can not oversee the contribution from my elder brother by being my primary source of joy and fun. My sun would have been as dark and cold as moon if not for him.

My colleagues in Satellite Systems Directorate of Turkish Aerospace Industries deserve the warmest appreciations on my behalf. I learned a lot from them and hope I have contributed to the projects with my full potential.

Last but not the least, I would also like to thank the Scientific and Technological Research Council of Turkey (TÜBİTAK) for awarding me their prestigious master of science studies scholarship.



## TABLE OF CONTENTS

ABSTRACT . . . . .	iv
ÖZ . . . . .	v
DEDICATION . . . . .	vi
ACKNOWLEDGMENTS . . . . .	vii
TABLE OF CONTENTS . . . . .	viii
LIST OF TABLES . . . . .	xi
LIST OF FIGURES . . . . .	xii
LIST OF SYMBOLS . . . . .	xv
CHAPTERS	
1 INTRODUCTION . . . . .	1
1.1 Motivation . . . . .	1
1.2 Literature Survey . . . . .	3
1.3 Contributions . . . . .	4
1.4 Thesis Overview . . . . .	5
2 SATELLITE MODEL . . . . .	7
2.1 Dynamics . . . . .	7
2.1.1 Single Rigid Body Dynamics . . . . .	7
2.1.2 Multiple Rigid Body Dynamics . . . . .	8
Vector derivation of equations of motion . . . .	10
Equations of motion in matrix notation . . . .	14
Linear algebraic motion equation . . . . .	18
Verification of the multi-body model . . . . .	25
Nonlinear spring model . . . . .	27

2.2	Kinematics . . . . .	28
2.3	Actuators . . . . .	30
2.3.1	Reaction Wheel Model . . . . .	31
	Determination of controller gain . . . . .	33
2.3.2	Reaction Wheel Assembly (RWA) . . . . .	34
2.4	Sensors . . . . .	36
2.4.1	Gyroscope . . . . .	36
2.4.2	Star Tracker . . . . .	37
2.4.3	Proximity Sensor . . . . .	38
3	DISTURBANCE MODELS . . . . .	40
3.1	External Disturbances . . . . .	40
3.1.1	Aerodynamic Drag . . . . .	40
3.1.2	Gravity Gradient Torque . . . . .	41
3.1.3	Solar Radiation Pressure . . . . .	42
3.1.4	Magnetic Residual Moment . . . . .	43
3.2	Internal Disturbances . . . . .	44
3.2.1	Propellant Sloshing . . . . .	45
3.2.2	Reaction Wheel Induced Vibration . . . . .	47
3.2.3	Slew Induced Vibration . . . . .	53
4	CONTROL ALGORITHMS . . . . .	54
4.1	Quaternion Feedback (QFB) Controller . . . . .	54
4.2	State Feedback (SFB) Controller . . . . .	55
4.2.1	State Reduction . . . . .	56
4.2.2	Linearizing the System . . . . .	62
4.2.3	Determining the Feedback Gain . . . . .	67
5	POINTING PERFORMANCE . . . . .	70
5.1	Performance Metrics . . . . .	70
5.2	Metric Calculation Algorithm . . . . .	72
6	RESULTS AND DISCUSSION . . . . .	74
6.1	Optimization for QFB Controller . . . . .	74

6.2	Simulation Results . . . . .	80
6.2.1	Results for QFB Controller . . . . .	80
6.2.2	Results for SFB Controller . . . . .	87
6.3	Comparison of Results . . . . .	94
7	CONCLUSION . . . . .	96
7.1	Future Work . . . . .	97
REFERENCES . . . . .		98
APPENDICES		
A	SIMULINK MODELS . . . . .	100
A.1	Simulink Model with Quaternion Feedback Controller . . . . .	100
A.2	Simulink Model with State Feedback Controller . . . . .	101

# LIST OF TABLES

## TABLES

Table 1.1	Properties of selected SAR satellites. . . . .	2
Table 2.1	Coordinate frame associations of dyadics and vectors . . . . .	15
Table 2.2	Parameters used in multi-body model verification . . . . .	25
Table 2.3	Reaction wheel parameters . . . . .	33
Table 2.4	Star tracker performance under different angular velocities . . . . .	38
Table 2.5	TQ 461 proximity sensor properties . . . . .	39
Table 3.1	Parameters of the sun-synchronous orbit <sup>[21]</sup> . . . . .	44
Table 3.2	Properties of pendulums representing sloshing fuel . . . . .	47
Table 3.3	Parameters for reaction wheel disturbance model . . . . .	51
Table 4.1	Maximum values for states and inputs . . . . .	68
Table 5.1	Algorithm for obtaining the pointing metrics from time sampled data . . . . .	72
Table 6.1	Pointing metrics for the QFB controller . . . . .	80
Table 6.2	Pointing metrics for the SFB controller . . . . .	87

# LIST OF FIGURES

## FIGURES

Figure 1.1	Examples of SAR satellites (Left; Radarsat-2, Right; Sentinel-1) . . . . .	2
Figure 2.1	General representation of the multi-body satellite model being considered .	10
Figure 2.2	Part of the multi-body spacecraft model showing only bodies $B_1$ , $B_2$ and $B_5$ together with position, force and torque vectors . . . . .	11
Figure 2.3	Joint $Gm$ connecting the inner body $i$ to the outer body $j$ . . . . .	13
Figure 2.4	Angular acceleration and velocity error of $B_1$ . . . . .	26
Figure 2.5	Angle errors of joints in solar array 1 . . . . .	27
Figure 2.6	Angle errors of joints in solar array 2 . . . . .	28
Figure 2.7	Angular displacement vs. Torque plot for torsional spring . . . . .	29
Figure 2.8	A typical reaction wheel unit . . . . .	31
Figure 2.9	Reaction wheel Simulink model . . . . .	31
Figure 2.10	Reaction wheel output justifying the predicted settling time . . . . .	34
Figure 2.11	A Tetrahedron. Each wheel of the RWA is situated perpendicular to sides in such a configuration . . . . .	35
Figure 2.12	Comparison of actual and measured angular rate . . . . .	38
Figure 2.13	A star tracker (SELEX Galileo of Finmeccanica) . . . . .	39
Figure 2.14	Model TQ 461 proximity sensor . . . . .	39
Figure 3.1	Non-uniform gravitational force leads to gravity gradient torque <sup>[19]</sup> . . . .	42
Figure 3.2	A depiction of Earth's magnetic field <sup>[20]</sup> . . . . .	44
Figure 3.3	Plot of external disturbance torque for 6 hours . . . . .	45
Figure 3.4	Fuel tank sloshing dynamics represented by a simple pendulum in a body rotating around pitch axis (adapted from Ref.[14]) . . . . .	46

Figure 3.5 Slosh disturbance torques in roll, pitch and yaw axes . . . . .	48
Figure 3.6 Reaction wheel together with representative masses for static ( $m_s$ ) and dynamic ( $m_d$ ) imbalances (adapted from Ref.[23]) . . . . .	49
Figure 3.7 Disturbance forces acting on the satellite main body due to reaction wheel imbalances . . . . .	52
Figure 3.8 Disturbance torques acting on the satellite main body due to reaction wheel imbalances . . . . .	52
Figure 4.1 Eigenvalues of the state Jacobian matrix $G_x$ . . . . .	67
Figure 5.1 Representative attitude error plot together with the steps of imaging process exposure time $T_E$ and readout time $T_{RO}$ . . . . .	71
Figure 5.2 Weighting functions for jitter ( $W_j$ ) and stability ( $W_s$ ) . . . . .	73
Figure 6.1 $3\sigma_a$ values (in $^\circ$ ) obtained in roll axis for different $K_p$ and $K_d$ values . . . .	75
Figure 6.2 $3\sigma_a$ values (in $^\circ$ ) obtained in pitch axis for different $K_p$ and $K_d$ values . . .	76
Figure 6.3 $3\sigma_a$ values (in $^\circ$ ) obtained in yaw axis for different $K_p$ and $K_d$ values . . .	76
Figure 6.4 $3\sigma_s$ values (in $^\circ$ ) obtained in roll axis for different $K_p$ and $K_d$ values . . . .	77
Figure 6.5 $3\sigma_s$ values (in $^\circ$ ) obtained in pitch axis for different $K_p$ and $K_d$ values . . .	77
Figure 6.6 $3\sigma_s$ values (in $^\circ$ ) obtained in yaw axis for different $K_p$ and $K_d$ values . . .	78
Figure 6.7 $3\sigma_j$ values (in $^\circ/s$ ) obtained in roll axis for different $K_p$ and $K_d$ values . . .	78
Figure 6.8 $3\sigma_j$ values (in $^\circ/s$ ) obtained in pitch axis for different $K_p$ and $K_d$ values . .	79
Figure 6.9 $3\sigma_j$ values (in $^\circ/s$ ) obtained in yaw axis for different $K_p$ and $K_d$ values . . .	79
Figure 6.10 Attitude history of the satellite main body (QFB controller) . . . . .	81
Figure 6.11 Main body angular rates for the duration of simulation (QFB) . . . . .	81
Figure 6.12 Main body angular accelerations for the duration of simulation (QFB) . . .	82
Figure 6.13 Detail from attitude error for the last 150 s of simulation (QFB) . . . . .	82
Figure 6.14 Joint angular velocities for the solar array 1 (QFB) . . . . .	83
Figure 6.15 Joint angular velocities for the solar array 2 (QFB) . . . . .	83
Figure 6.16 Joint angular positions for the solar array 1 (QFB) . . . . .	84
Figure 6.17 Joint angular positions for the solar array 2 (QFB) . . . . .	84

Figure 6.18 Actuator torque being applied on the satellite (QFB) . . . . .	85
Figure 6.19 Reaction wheel angular velocities (QFB) . . . . .	85
Figure 6.20 Disturbance torques due to reaction wheels acting on the satellite (QFB) . .	86
Figure 6.21 Disturbance torques due to propellant sloshing acting on the satellite (QFB)	86
Figure 6.22 Attitude history of the satellite main body (SFB Controller) . . . . .	87
Figure 6.23 Main body angular rates for the duration of simulation (SFB) . . . . .	88
Figure 6.24 Main body angular accelerations for the duration of simulation (SFB) . . .	88
Figure 6.25 Detail from attitude error from the last half of the simulation (SFB) . . . .	89
Figure 6.26 Joint angular velocities for the first solar array (SFB) . . . . .	89
Figure 6.27 Joint angular velocities for the second solar array (SFB) . . . . .	90
Figure 6.28 Joint angular positions for the solar array 1 (SFB) . . . . .	90
Figure 6.29 Joint angular positions for the solar array 2 (SFB) . . . . .	91
Figure 6.30 Actuator torque being applied on the satellite (SFB) . . . . .	91
Figure 6.31 Reaction wheel angular velocities (SFB) . . . . .	92
Figure 6.32 Disturbance torques due to reaction wheels acting on the satellite (SFB) . .	92
Figure 6.33 Disturbance torques due to propellant sloshing acting on the satellite (SFB)	93
Figure A.1 Simulink model for multi-body satellite with QFB controller . . . . .	100
Figure A.2 Simulink model for multi-body satellite with SFB controller . . . . .	101

## LIST OF SYMBOLS

$m$	Mass for the single rigid body case	$A$	System matrix for the linear algebraic multi-body equation of motion
$J$	Moment of inertia for the single rigid body case	$u$	Input column matrix for the linear algebraic multi-body equation of motion
$\omega$	Angular rate for the single rigid body case	$y$	Output column matrix for the linear algebraic multi-body equation of motion
$T$	External torque for the single rigid body case	$e$	Absolute error obtained during the verification of multi-body model
$\mathbb{F}_i$	Reference frame on body $i$ ( $i = 0$ when inertial)	$x_{MM}$	Variable obtained from the developed mathematical model during verification
$J_i$	Moment of inertia of body $i$	$x_{SM}$	Variable obtained from the SimMechanics model during verification
$m_i$	Mass of body $i$	$h_{w,comm}$	commanded angular momentum for reaction wheel
$\omega_i$	Angular rate of body $i$	$h_{w,comm}$	angular momentum obtained from reaction wheel
$\omega_{j/i}$	Relative angular velocity of body $j$ with respect to body $i$	$K_M$	Motor torque coefficient of reaction wheel
$H_i$	Angular momentum of body $i$	$R_M$	Electrical resistance of reaction wheel motor
$T_i$	External torque being applied on body $i$	$J_W$	Reaction wheel moment of inertia
$F_i$	External force being applied on body $i$	$B$	Reaction wheel viscous damping
$T_{Gi}$	Reaction torque at joint $i$	$K_V$	Reaction wheel back electromotive force constant
$F_{Gi}$	Reaction force at joint $i$	$K_C$	Reaction wheel controller gain
$r_{ij}$	Position vector from body $i$ 's center of mass to the joint connecting body $i$ to body $j$	$V_M$	Voltage applied to reaction wheel motor
$\theta_i$	Angular displacement at joint $i$	$i_M$	Current applied to reaction wheel motor
$n_j^i$	Unit vector along the axis $j$ of reference frame $i$	$K_{p,rw}$	Proportional controller gain for reaction wheel speed controller
$q$	Quaternion column matrix defining the main body attitude	$K_{i,rw}$	Integral controller gain for reaction wheel speed controller
$\theta, \varphi, \psi$	Euler angles defining the main body attitude		
$f_{spring,i}$	Function defining the torque generated by the torsional spring at the joint $i$		
$k_1, k_2$	Torsional spring constants		



$T_M$	Torque applied by the motor on reaction wheel	$\omega_0$	Satellite orbital rate
$T_{RWA}$	Torque generated by reaction wheel assembly	$\mu_E$	Earth's gravitational constant
$h_{RWA}$	Total angular momentum of reaction wheel assembly	$df_{sol}$	Force acting on an area element due to solar radiation pressure
$E$	Reaction wheel assembly steering law	$P_{sol}$	Solar momentum flux
$e_i$	Unit vectors defining reaction wheel $i$	$s_{sol}$	Unit vector directed to Sun
$T_C$	Control torque calculated by the controller	$dA_{sol}$	Area element used in the calculation of solar radiation pressure
$\omega_{1,meas}$	Angular rate of main body (body 1) measured by gyroscope	$n_{sol}$	Normal vector of the area element
$S$	Gyroscope scale factor error matrix	$\theta_{sol}$	Angle between area element normal and unit vector in sun direction
$s_1, s_2, s_3$	Gyroscope scale factor errors	$c_s$	Coefficient of specular reflection
$U$	Gyroscope alignment matrix	$c_d$	Coefficient of diffusive reflection
$\beta$	Gyroscope drift rate	$r_{sol}$	Position of the area element on the spacecraft
$\eta$	Gyroscope white noise	$T_{sol}$	Torque due to solar radiation pressure
$F_{surf,i}$	Aerodynamic drag force acting on satellite surface element $i$	$T_{mag}$	Torque due to magnetic residual
$\rho$	Atmospheric density	$m_{res}$	Residual magnetic dipole moment
$C_D$	Aerodynamic drag coefficient	$B_{mag}$	Local magnetic field
$A_{surf,i}$	Area of satellite surface element $i$	$T_{slosh}$	Propellant sloshing disturbance torque
$V_\infty$	Satellite translational velocity	$m_x, m_y, m_z$	Masses of representative pendulums
$F_{aero}$	Total aerodynamic drag force acting on the satellite	$b_x, b_y, b_z$	Pendulum rotation axis offsets
$r_{surf,i}$	Position vector for the center of pressure for the satellite surface element $i$	$c_x, c_y, c_z$	Damping coefficients of pendulums
$T_{aero}$	Total aerodynamic drag torque acting on the satellite	$l_x, l_y, l_z$	Length of representative pendulums
$\theta_{surf,i}$	Angle between flow direction and normal of the satellite surface element $i$	$\alpha$	Pendulum angle
$T_{gg}$	Gravity gradient torque acting on the satellite	$F_{wi}$	Disturbance force due to imbalance of wheel $i$
$R_{pos}$	Satellite position vector	$T_{wi}$	Disturbance torque due to imbalance of wheel $i$
$r_u$	Unit vector along the satellite position vector	$\omega_{wi}$	Rotational speed of wheel $i$
		$m_s$	Static imbalance mass
		$m_d$	Dynamic imbalance mass
		$r_s$	Distance of static imbalance mass from the rotation axis
		$r_d$	Distance of dynamic imbalance mass from the rotation axis

$r_{wi}$	Position vector of the reaction wheel $i$	<b>Superscripts</b>	
$C_{1wi}$	Transformation matrix from the frame of body 1 to reaction wheel $i$		$(\vec{\cdot})$ Vector
$F_{rwa,dist}$	Disturbance forces due to whole reaction wheel assembly		$(\check{\cdot})$ Dyadic
$T_{rwa,dist}$	Disturbance torques due to whole reaction wheel assembly		$(\hat{\cdot})$ Matrix
$q_R$	Reference quaternion		$(\bar{\cdot})$ Column matrix
$q_E$	Error quaternion		$\left(\frac{d(\vec{\cdot})}{dt}\right)_{\mathbb{F}_i}$ Time derivative of a vector in frame $i$
$K_P$	Quaternion feedback proportional gain matrix		$(\tilde{\cdot})$ Skew symmetric matrix
$K_D$	Quaternion feedback derivative gain matrix		$(\cdot)^T$ Matrix transpose
$K_p$	Proportional gain constant		
$K_d$	Derivative gain constant		
$J_{Tot}$	Total moment of inertia of the multi-body system		
$K$	State feedback gain matrix		
$G_x$	State Jacobian matrix		
$G_u$	Input Jacobian matrix		
$N_{Perf}$	Performance index for linear quadratic regulator		
$Q$	State weighing matrix		
$R$	Input weighing matrix		
$P$	Solution of Riccati equation		
$w_{Qi}$	Weights of state weighing matrix		
$w_{Ri}$	Weights of input weighing matrix		
$T_E$	Payload exposure time		
$T_{RO}$	Payload readout time		
$\sigma_a$	Accuracy metric		
$\mu$	Mean pointing error		
$T_j$	Jitter time window		
$\sigma_j$	Jitter metric		
$T_s$	Stability time window		
$\sigma_s$	Stability metric		
$W_j$	Jitter metric weighing function		
$W_s$	Stability metric weighing function		
$P_{spec}$	Power spectrum of attitude error		

# CHAPTER 1

## INTRODUCTION

### 1.1 Motivation

Attitude control and pointing performance have great influence on Earth and astronomical observation missions. For meaningful scientific returns, satellites have to point within certain accuracy. This accuracy is generally defined as a system level requirement. The pointing performance is adversely effected by disturbances such as environmental torques (torques due to atmospheric drag, solar radiation pressure, magnetic field) and other internal effects (such as disturbances due to reaction wheels and increased satellite flexibility due to appendages). Attitude control algorithms must address the challenge of mitigating the effects of these disturbances.

Meanwhile, spacecraft payloads are becoming more capable with advancing technology. These payloads, such as SAR<sup>1</sup>, demand high amount of power for operation. This demand is satisfied by introducing additional solar panel area resulting in increased system complexity. Structural effects due to these enlarged panels also have to be taken into account when developing attitude control systems (Figure 1.1).

One type of satellite with high pointing accuracy requirements are SAR satellites.  $3\sigma$  pointing accuracy values for various SAR satellites collected from the literature are given in Table 1.1 together with their launch mass, solar panel area, end of life (EOL) power output and aperture size. One common trend that can be inferred from these data is that SAR spacecraft are large in mass and in size with very high pointing accuracy requirements.

---

<sup>1</sup> Synthetic Aperture Radar

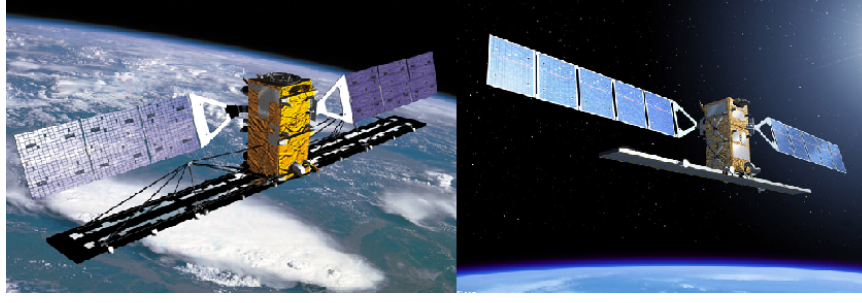


Figure 1.1: Examples of SAR satellites (Left; Radarsat-2, Right; Sentinel-1)

Table 1.1: Properties of selected SAR satellites.

Satellite	Launch Mass (kg)	Solar Panel Area ( $\text{m}^2$ )	EOL Power (Watt)	SAR Antenna Size (m)	Pointing Accuracy ( $^\circ$ )
Radarsat-2 <sup>[1]</sup>	2300	13.42	2400	$15 \times 1.37$	0.05
Sentinel-1 <sup>[2]</sup>	2300	NA	4800	$12.3 \times 0.84$	0.03
COSMO-SkyMed <sup>[3]</sup>	1750	18.30	3600	$5.7 \times 1.4$	NA

SAR satellites are not the only example for missions requiring high pointing performance. More popular are the astronomical missions such as Hubble Space Telescope. These missions tend to have more strict pointing requirements due to the fine nature of their targets and their much complex payloads required to observe them.

Considering the aforementioned facts, it can be deduced that developing an attitude control for observation missions (whether EO<sup>2</sup> or astronomical) is a not an easy task. Not only do strict pointing performance requirements exist, but also an additional solar panel area is being accommodated on the satellite due to the payload's increased power demand. The dynamic models of these large panels have to be included in the development of satellite dynamical model. Furthermore, its effects on pointing performance have to be determined.

However, disturbance due to the solar panels is hardly the only disturbance that will be effecting the spacecraft. The vibration stemming from the reaction wheels would be prominent in degrading the spacecraft stability. Moreover, sensor noise would also downgrade the attitude determination resulting in reduced pointing performance. In addition to these, external disturbances may also effect the spacecraft, although their effects would be considerably at lower

<sup>2</sup> Earth Observation

frequencies than the ones just have been mentioned.

This study addresses the challenge of determining the effect of aforementioned disturbances on the satellite pointing performance. For this purpose, first a satellite model is formed for simulations. Models of different disturbance sources are added to this model. Then, methods for calculating the pointing performance are obtained. Control strategies are proposed to improve pointing performance. Finally inferences are made from all these experience in order to be used in ADCS<sup>3</sup> design.

## 1.2 Literature Survey

The literature relevant to this study is reviewed under this topic. Literature sources that are focusing on a specific topic are reviewed at the beginning of relevant sections.

In determination of ADCS pointing performance, developing pointing error budgets is a crucial step. One such budget was developed by Lee *et al* for the Space Interferometry Mission Spacecraft<sup>[4]</sup>. Contributions from various sources to the error budget was investigated. Methods used in quantitatively obtaining these disturbances were also presented. The error sources covered were attitude determination error, star tracker bias, residual errors after calibrations, thermal distortion between calibrations, slew induced structural vibration, RWA<sup>4</sup> controller error, RWA induced structural vibration, solar array control interaction, thermal flutter and spacecraft-instrument control interaction. The RWA induced vibration turned out to be the primary source of stability error.

Pittelkau undertook the task of defining various metrics for analyzing spacecraft pointing performance<sup>[5]</sup>. Definitions and mathematical expressions for pointing error, accuracy, displacement, jitter and stability metrics were given. Furthermore, algorithms were presented that enable the calculations of these metrics from the output data of a time domain simulator. The metrics were obtained via frequency domain calculations, utilizing weighting functions.

Calculation of pointing metrics are crucial for the determination of attitude controller's effectiveness. These calculations are generally carried out with numerical methods. Bayard proposed a state space method for the evaluation of jitter metric<sup>[6]</sup>. In this particular work,

---

<sup>3</sup> Attitude Determination and Control System

<sup>4</sup> Reaction Wheel Assembly

detailed definitions for the statistical analysis of the pointing performance was given. Also, a rigorous mathematical derivation of the spacecraft pointing process was presented in state space form.

Pointing performance metrics are derived from instrument pointing performance requirements. A similar derivation process was carried out by Kia *et al* for the SIRT<sup>F5</sup> currently known as Spitzer Space Telescope<sup>[7]</sup>. Flow of requirements down to metrics was given. Pointing Control System modes that would realize these metrics were also presented in detail.

Spacecraft jitter reduce the quality of scientific data generated by the payload. Thus, methods for jitter mitigations are sought. Agrawal<sup>[8]</sup> states that, they can be several approaches to this problem. The impact of jitter can be reduced addressing the problem at the source by the isolation of vibration sources (such as reaction wheels); or oppositely the payload can be isolated by using damping elements (such as D-Struts). The overall damping of the structures may as well be reduced by the utilization of passive and active dampers. Another way is to employ fast steering mirrors (assuming that you have an electro-optical imaging device) in your payload to compensate for the poor stability characteristics of the spacecraft bus. A combination of these approaches are generally used to enhance spacecraft jitter mitigation performance.

### 1.3 Contributions

This thesis seeks to achieve the following goals:

- Devising a computer model to simulate pointing scenarios including slew maneuver and subsequent stabilization
- Developing a multi-body spacecraft mathematical model
- Modeling various disturbances of both internal and external nature that may effect this scenario
  - External disturbances
  - Internal disturbances (propellant sloshing, reaction wheel static and dynamic imbalance)

---

<sup>5</sup> Space Infrared Telescope Facility

- Designing controllers that enable meaningful pointing performance under the effect of these disturbances
  - Quaternion feedback controller
  - State feedback controller
- Devising methods to assess the performance of controllers for determination of controller effectiveness

## 1.4 Thesis Overview

This thesis is structured into the following sections:

*Chapter 1* Provides basic introduction on the subject and presents motivation regarding the problem. Also includes the review of pertinent literature.

*Chapter 2* Dynamic and kinematic models of an ideal spacecraft is obtained. Mathematical modeling of multi-body satellite is carried out. Equations of motion for such a spacecraft is obtained through Newton-Euler formulation. This model is then verified via comparison with an identical model developed in SimMechanics of MATLAB. Sensing and actuator models are implemented. Nonlinear models for springs and dampers for the solar arrays are introduced.

*Chapter 3* External disturbance model is included. Internal disturbance models are examined. Among them, disturbing effects of propellant sloshing is modeled together with disturbances stemming from reaction wheel static and dynamic imbalance.

*Chapter 4* Attitude control schemes are investigated. Quaternion feedback controller is used. State feedback controller is also implemented by obtaining the state matrix by linearizing the mathematical model obtained in Chapter 2 around equilibrium point.

*Chapter 5* Pointing performance metrics are investigated and their definitions are presented. Algorithm for obtaining pointing metrics is given.

*Chapter 6* Feedback gain assessment results for the quaternion feedback controllers are presented. A slew maneuver scenario is simulated by the controllers of the both schemes and their results are compared.

*Chapter 7* Conclusions are drawn from the results obtained in Chapter 6. Possible avenues for future work are highlighted.



## CHAPTER 2

### SATELLITE MODEL

The spacecraft model consists of the dynamics, kinematics, actuator and sensor models. Dynamics model is utilized to obtain the resulting accelerations (both linear and angular) due to the forces and torques applied on the system. Kinematics model relate the accelerations obtained from the dynamics model to the velocities and positions. Actuator model involves the detailed modeling of reaction wheels whereas the sensor models involve the mathematical models of the gyroscope, star tracker and proximity sensors.

#### 2.1 Dynamics

Dynamics models relate the forces and torques being applied on the system to the translational and angular accelerations. Since the main focus of this topic is the attitude dynamics, rotational motion will be emphasized. First the single rigid body dynamics will be introduced followed by the model of multiple rigid bodies.

##### 2.1.1 Single Rigid Body Dynamics

The dynamics model of the simple rigid body is obtained by the well-known Euler's rotational equation of motion:

$$\check{J} \cdot \left( \frac{d\vec{\omega}}{dt} \right)_{\mathbb{F}_0} + \vec{\omega} \times \check{J} \cdot \vec{\omega} = \vec{T} \quad (2.1)$$

where  $\check{J}$  is the inertia dyadic,  $\vec{T}$  is the vector defining the applied torques and  $\vec{\omega}$  is the inertial

body angular rate. Note that:

$$\left(\frac{d\vec{\omega}}{dt}\right)_{\mathbb{F}_0} = \underbrace{\vec{\omega} \times \vec{\omega}}_{\vec{0}} + \left(\frac{d\vec{\omega}}{dt}\right)_{\mathbb{F}_1} \quad (2.2)$$

Writing eq.(2.1) in a reference frame which also assumed to be coincident with the principal axes of the rigid body (body frame  $\Gamma_B$ ), the following are obtained<sup>[9]</sup>:

$$\hat{J}\dot{\bar{\omega}} + \bar{\omega}\hat{J}\bar{\omega} = \bar{T} \quad (2.3)$$

Where  $\hat{J}$  is the inertia matrix,  $\bar{\omega}$  is the angular rate column matrix and  $\tilde{\omega}$  is the skew symmetric matrix formed from the elements of  $\bar{\omega}$ :

$$\tilde{\omega} = \begin{bmatrix} 0 & \omega_z & -\omega_y \\ -\omega_z & 0 & \omega_x \\ \omega_y & -\omega_x & 0 \end{bmatrix} \quad (2.4)$$

Solving eq.(2.3) for the angular acceleration:

$$\dot{\bar{\omega}} = \hat{J}^{-1}(\bar{T} - \bar{\omega}\hat{J}\bar{\omega}) \quad (2.5)$$

### 2.1.2 Multiple Rigid Body Dynamics

Modern spacecraft tend to have multiple appendages for different purposes. They may house dish type antenna systems and mechanisms for their orientation; or they may have solar arrays composed of several segments which can be driven by a servo mechanism for keeping them directed towards the sun. Thus, single rigid body assumption does not hold for all cases and further detailed modeling may be required.

Wie<sup>[9]</sup> addressed the problem of modeling multi-body spacecraft by proposing several methods. For preliminary modeling he suggests lumped parameter analysis (in which appendages are assumed as point masses) whereas for detailed models finite element analysis was proposed. He further utilizes elastic beams for modeling of appendage effects in single axis

rotation cases. Similarly, Junkins<sup>[10]</sup> also models the appendages using beam analogy in two dimensions whilst deriving the motion equations using Lagrange's approach. Hughes<sup>[11]</sup> develops motion expressions for two interconnected bodies in three dimensional space via extensive derivation stemming from Newton-Euler approach; however the outcome is hard to implement in a simulation environment due to involvement of terms like "mixed moments of inertia" in the solution.

Stoneking<sup>[12]</sup> treats the problem of two rigid bodies connected with a spherical joint and is able to obtain a linear algebraic representation of the problem. The problem is further extended to N body case and inferences were made how "mass" and "force" matrices were assembled within the system matrix obtained. Even though the method presented by Stoneking paved the way for the derivations being discussed within this section, it had shortcomings regarding the inclusion of reaction torques among the bodies due to the assumption that all joints are spherical.

The satellite model being considered in this study is presented in Figure 2.1. It is composed of seven rigid bodies which are named from  $B_1$  to  $B_7$ .  $B_1$  represents the satellite main body which is assumed to host the imaging device. Therefore, its orientation will be the one that will be monitored and controlled.  $B_2$  and  $B_5$  represent the mechanical links called "yokes" that connect solar arrays to the main body.  $B_3$ ,  $B_4$ ,  $B_6$  and  $B_7$  are the rigid bodies representing the solar arrays. All the bodies are connected with revolute joints with each other that house torsional springs and dampers. The solar array composed of bodies  $B_2$ ,  $B_3$  and  $B_4$  is identified as solar array 1 whereas the solar array composed of bodies  $B_5$ ,  $B_6$  and  $B_7$  is identified as solar array 2.

A detail from the multi-body spacecraft model utilized in this study is presented in the Figure 2.2. In this model, single DOF<sup>1</sup> hinge joints are assumed to be located at points  $G_m$  where  $m$  is the joint number from 1 to 6. Reaction forces ( $\vec{F}_{Gm}$ ) and torques ( $\vec{T}_{Gm}$ ) are applied by these joints to the adjoining bodies. Revolute joint angular positions are represented by  $\theta_m$ . Furthermore, revolute joints also house torsional springs. Orthogonal frames centered at the COMs<sup>2</sup> of these bodies are also shown. COMs are assumed to be located at the geometric centers of the bodies. Additionally, body forces and torques  $\vec{F}_n$  and  $\vec{T}_n$  (where  $n$  is the body

---

<sup>1</sup> Degree of Freedom

<sup>2</sup> Center of Mass

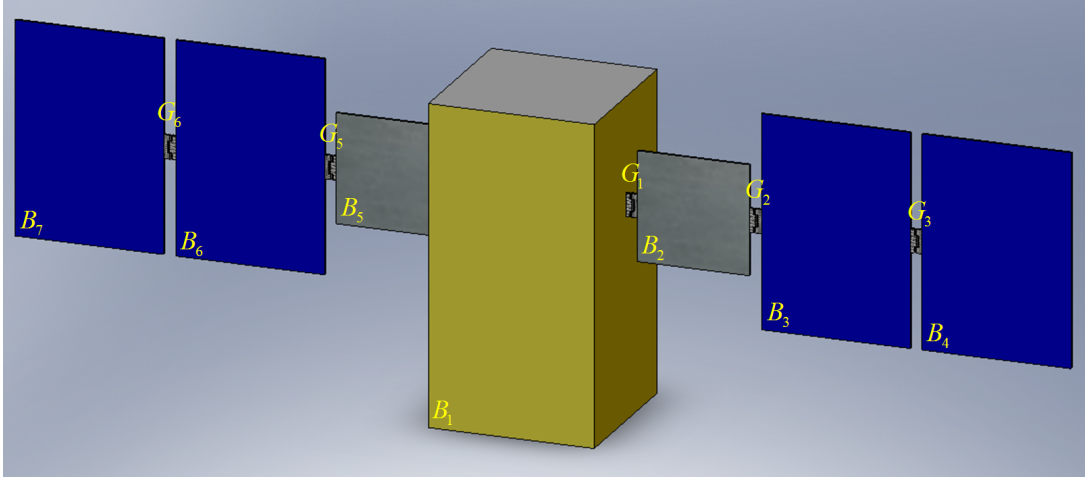


Figure 2.1: General representation of the multi-body satellite model being considered

number) are assumed to be acting on the COMs of the associated bodies. In Figure 2.2, only variables corresponding to bodies  $B_1$ ,  $B_2$ ,  $B_5$  and joints  $G_1$ ,  $G_4$  are shown. Lastly, the position vectors are represented by the vectors  $\vec{r}_{ij}$  where  $i$  is the number of body whose COM the position vector is stemming from and  $j$  is the adjoining body it is directed to. These vectors terminate at the joints connecting body  $i$  to body  $j$  (observe the vectors  $\vec{r}_{12}$  and  $\vec{r}_{21}$  in Figure 2.2).

**Vector derivation of equations of motion** Assuming that the reaction forces and torques are acting on the inner body (body preceding the joint) in positive sense and recalling eq.(2.2), the Euler equation for body  $B_1$  can be written as:

$$\check{J}_1 \cdot \left( \frac{d\vec{\omega}_1}{dt} \right)_{\mathbb{F}_1} = \vec{T}_1 - \vec{\omega}_1 \times \vec{H}_1 + \vec{T}_{G1} + \vec{T}_{G4} + \vec{r}_{12} \times \vec{F}_{G1} + \vec{r}_{15} \times \vec{F}_{G4} \quad (2.6)$$

Where  $\vec{\omega}_1$  is the inertial angular velocity of  $B_1$  and  $\check{J}_1$  is the inertia dyadic,  $\vec{H}_1$  is the angular momentum vector and equals  $\check{J}_1 \cdot \vec{\omega}_1$ . Similarly, for the body  $B_2$ :

$$\check{J}_2 \cdot \left( \frac{d\vec{\omega}_2}{dt} \right)_{\mathbb{F}_2} = \vec{T}_2 - \vec{\omega}_2 \times \vec{H}_2 - \vec{T}_{G1} + \vec{T}_{G2} - \vec{r}_{21} \times \vec{F}_{G1} + \vec{r}_{23} \times \vec{F}_{G2} \quad (2.7)$$

and for body  $B_3$ :

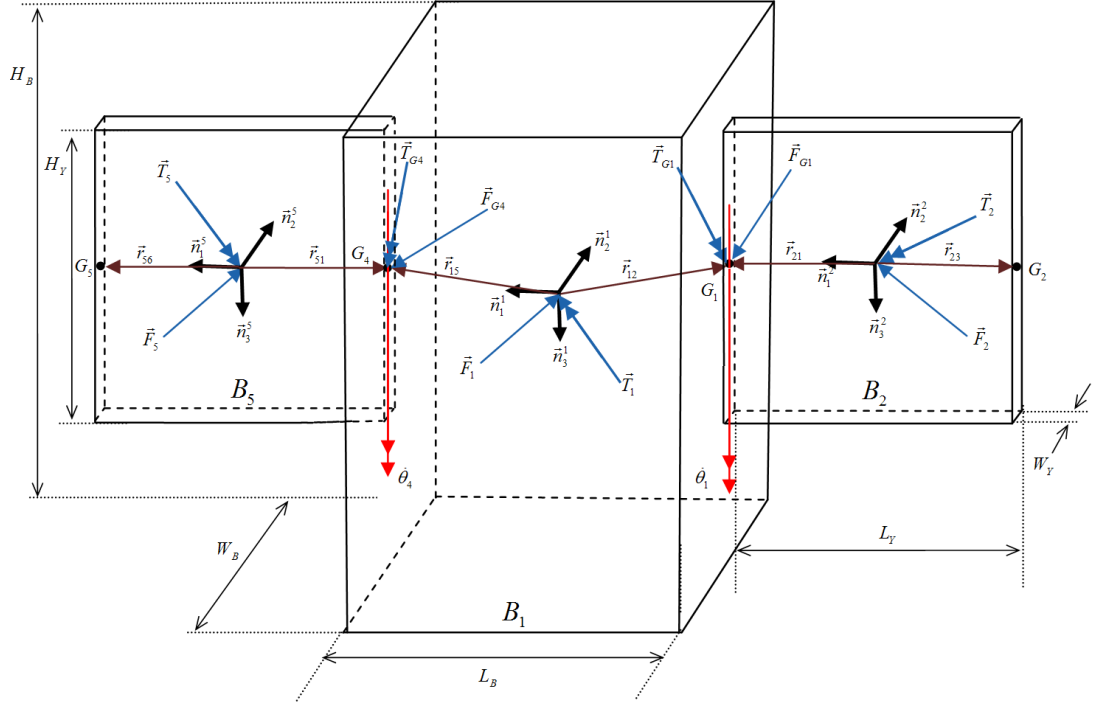


Figure 2.2: Part of the multi-body spacecraft model showing only bodies  $B_1$ ,  $B_2$  and  $B_5$  together with position, force and torque vectors

$$\check{J}_3 \cdot \left( \frac{d\vec{\omega}_3}{dt} \right)_{\mathbb{F}_3} = \vec{T}_3 - \vec{\omega}_3 \times \vec{H}_3 - \vec{T}_{G2} + \vec{T}_{G3} - \vec{r}_{32} \times \vec{F}_{G2} + \vec{r}_{34} \times \vec{F}_{G3} \quad (2.8)$$

for the body  $B_4$  which is also the end member of the array 1:

$$\check{J}_4 \cdot \left( \frac{d\vec{\omega}_4}{dt} \right)_{\mathbb{F}_4} = \vec{T}_4 - \vec{\omega}_4 \times \vec{H}_4 - \vec{T}_{G3} - \vec{r}_{43} \times \vec{F}_{G3} \quad (2.9)$$

continuing the Euler's equations with the first member of the array 2,  $B_5$ :

$$\check{J}_5 \cdot \left( \frac{d\vec{\omega}_5}{dt} \right)_{\mathbb{F}_5} = \vec{T}_5 - \vec{\omega}_5 \times \vec{H}_5 - \vec{T}_{G4} + \vec{T}_{G5} - \vec{r}_{51} \times \vec{F}_{G4} + \vec{r}_{56} \times \vec{F}_{G5} \quad (2.10)$$

and for body  $B_6$ :

$$\check{J}_6 \cdot \left( \frac{d\vec{\omega}_6}{dt} \right)_{\mathbb{F}_6} = \vec{T}_6 - \vec{\omega}_6 \times \vec{H}_6 - \vec{T}_{G5} + \vec{T}_{G6} - \vec{r}_{65} \times \vec{F}_{G5} + \vec{r}_{67} \times \vec{F}_{G6} \quad (2.11)$$

and finally, for body  $B_7$ :

$$\check{J}_7 \cdot \left( \frac{d\vec{\omega}_7}{dt} \right)_{\mathbb{F}_7} = \vec{T}_7 - \vec{\omega}_7 \times \vec{H}_7 - \vec{T}_{G6} - \vec{r}_{76} \times \vec{F}_{G6} \quad (2.12)$$

In a similar fashion, Newton's equation can be written for all the bodies involved. For body  $B_1$ :

$$m_1 \left( \frac{d\vec{v}_1}{dt} \right)_{\mathbb{F}_0} = \vec{F}_1 + \vec{F}_{G1} + \vec{F}_{G5} \quad (2.13)$$

which yields;

$$m_1(\vec{\omega}_1 \times \vec{v}_1) + m_1 \left( \frac{d\vec{v}_1}{dt} \right)_{\mathbb{F}_1} = \vec{F}_1 + \vec{F}_{G1} + \vec{F}_{G5} \quad (2.14)$$

similarly, body  $B_2$ :

$$m_2(\vec{\omega}_2 \times \vec{v}_2) + m_2 \left( \frac{d\vec{v}_2}{dt} \right)_{\mathbb{F}_2} = \vec{F}_2 - \vec{F}_{G1} + \vec{F}_{G2} \quad (2.15)$$

for body  $B_3$ :

$$m_3(\vec{\omega}_3 \times \vec{v}_3) + m_3 \left( \frac{d\vec{v}_3}{dt} \right)_{\mathbb{F}_3} = \vec{F}_3 - \vec{F}_{G2} + \vec{F}_{G3} \quad (2.16)$$

and for body  $B_4$ :

$$m_4(\vec{\omega}_4 \times \vec{v}_4) + m_4 \left( \frac{d\vec{v}_4}{dt} \right)_{\mathbb{F}_4} = \vec{F}_4 - \vec{F}_{G3} \quad (2.17)$$

moving on to the elements of the other solar array, body  $B_5$ :

$$m_5(\vec{\omega}_5 \times \vec{v}_5) + m_5 \left( \frac{d\vec{v}_5}{dt} \right)_{\mathbb{F}_5} = \vec{F}_5 - \vec{F}_{G4} + \vec{F}_{G5} \quad (2.18)$$

also for body  $B_6$ :

$$m_6(\vec{\omega}_6 \times \vec{v}_6) + m_6 \left( \frac{d\vec{v}_6}{dt} \right)_{\mathbb{F}_6} = \vec{F}_6 - \vec{F}_{G5} + \vec{F}_{G6} \quad (2.19)$$

and finally, for body  $B_7$ :

$$m_7(\vec{\omega}_7 \times \vec{v}_7) + m_7 \left( \frac{d\vec{v}_7}{dt} \right)_{\mathbb{F}_7} = \vec{F}_7 - \vec{F}_{G6} \quad (2.20)$$

Having obtained the Newton's and Euler's equations, we currently have 42 equations covering unknowns  $\left( \frac{d\vec{\omega}_n}{dt} \right)_{\mathbb{F}_n}$  and  $\left( \frac{d\vec{v}_n}{dt} \right)_{\mathbb{F}_n}$ ; yet there also exists additional 42 unknowns defining the joint reaction forces  $\vec{F}_{Gm}$  (18) and joint reaction torques  $\vec{T}_{Gm}$  (18) and joint angles  $\theta_m$  (6). Thus, an additional set of 42 equations are needed. 18 of them can be introduced by taking the joint constraints into consideration. As mentioned previously, it was assumed that joint  $Gm$  connects the inner body  $i$  to the outer body  $j$  (Figure 2.3).

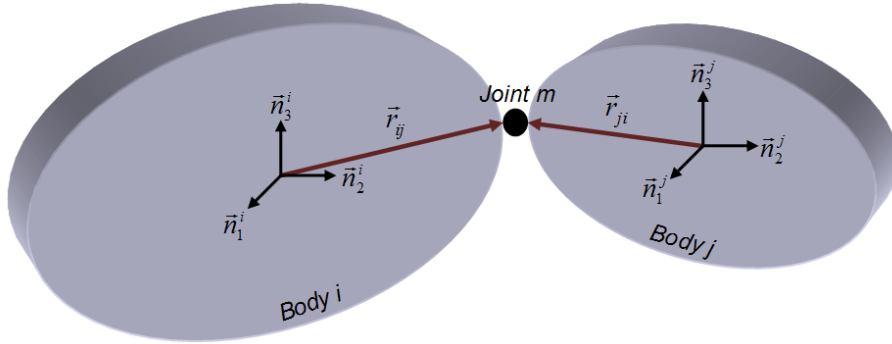


Figure 2.3: Joint  $Gm$  connecting the inner body  $i$  to the outer body  $j$

The velocity of joint  $Gm$  can then be described by both using the variables of inner and outer bodies  $B_i$  and  $B_o$ :

$$\vec{v}_{Gm} = \vec{v}_i + \vec{\omega}_i \times \vec{r}_{ij} = \vec{v}_j + \vec{\omega}_j \times \vec{r}_{ji} \quad (2.21)$$

differentiating eq.(2.21) with respect to time in inertial frame, the joint constraint vector equation is obtained:

$$\vec{\omega}_i \times \vec{v}_i + \left( \frac{d\vec{v}_i}{dt} \right)_{\mathbb{F}_i} + \left( \frac{d\vec{\omega}_i}{dt} \right)_{\mathbb{F}_i} \times \vec{r}_{ij} + \vec{\omega}_i \times (\vec{\omega}_i \times \vec{r}_{io}) = \vec{\omega}_j \times \vec{v}_j + \left( \frac{d\vec{v}_j}{dt} \right)_{\mathbb{F}_j} + \left( \frac{d\vec{\omega}_j}{dt} \right)_{\mathbb{F}_j} \times \vec{r}_{ji} + \vec{\omega}_j \times (\vec{\omega}_j \times \vec{r}_{ji}) \quad (2.22)$$

Another 18 equations can be introduced by considering the identity that defines the relative angular velocities among the inner and outer bodies connected by the revolute joint:

$$\vec{\omega}_j - \vec{\omega}_i = \vec{\omega}_{j/i} \quad (2.23)$$

Where  $\vec{\omega}_{j/i}$  is:

$$\vec{\omega}_{j/i} = 0 \cdot \vec{n}_1^j + 0 \cdot \vec{n}_2^j + \dot{\theta}_m \cdot \vec{n}_3^j \quad (2.24)$$

here,  $\vec{n}_1^j$ ,  $\vec{n}_2^j$  and  $\vec{n}_3^j$  are the unit vectors in the frame of outer body  $j$ . Upon differentiating eq.(2.23) with respect to the time and recalling that  $\vec{\omega}_i$  and  $\vec{\omega}_j$  are inertial angular velocities:

$$\left( \frac{d\vec{\omega}_j}{dt} \right)_{\mathbb{F}_j} - \left( \frac{d\vec{\omega}_i}{dt} \right)_{\mathbb{F}_i} - \vec{\omega}_j \times \vec{\omega}_{j/i} = \left( \frac{d\vec{\omega}_{j/i}}{dt} \right)_{\mathbb{F}_j} \quad (2.25)$$

Writing eq.(2.25) for all joints ( $m = 1, \dots, 6$ ), the total number of equations is raised to 78. The last 6 equations can be obtained by using the mathematical model for the spring housed within the revolute joint:

$$\vec{T}_{Gm} = 0 \cdot \vec{n}_1^j + 0 \cdot \vec{n}_2^j + f_{spring,m}(\theta_m) \cdot \vec{n}_3^j \quad (2.26)$$

where  $f_{spring,m}(\theta_m)$  is the spring functions which we will be dealing with later. Establishing eq.(2.26) again for all joints, the number of equations and unknowns are finally equalized. Next step will be writing these equations in matrix notation.

**Equations of motion in matrix notation** Before writing the equations of motion in matrix form, we have to determine which frames would be used for each equation. It is decided to write each motion equation in the frame of the body whose motion it describes. Moreover,



Table 2.1: Coordinate frame associations of dyadics and vectors

Frame	Dyadics	Vectors
$B_1$	$\check{J}_1$	$\vec{\omega}_1, \vec{T}_1, \vec{H}_1, \vec{r}_{12}, \vec{r}_{15}, \vec{v}_1, \vec{F}_1$
$B_2$	$\check{J}_2$	$\vec{\omega}_2, \vec{T}_2, \vec{H}_2, \vec{r}_{21}, \vec{r}_{23}, \vec{v}_2, \vec{F}_2, \vec{T}_{G1}, \vec{F}_{G1}$
$B_3$	$\check{J}_3$	$\vec{\omega}_3, \vec{T}_3, \vec{H}_3, \vec{r}_{32}, \vec{r}_{34}, \vec{v}_3, \vec{F}_3, \vec{T}_{G2}, \vec{F}_{G2}$
$B_4$	$\check{J}_4$	$\vec{\omega}_4, \vec{T}_4, \vec{H}_4, \vec{r}_{43}, \vec{v}_4, \vec{F}_4, \vec{T}_{G3}, \vec{F}_{G3}$
$B_5$	$\check{J}_5$	$\vec{\omega}_5, \vec{T}_5, \vec{H}_5, \vec{r}_{51}, \vec{r}_{56}, \vec{v}_5, \vec{F}_5, \vec{T}_{G4}, \vec{F}_{G4}$
$B_6$	$\check{J}_6$	$\vec{\omega}_6, \vec{T}_6, \vec{H}_6, \vec{r}_{65}, \vec{r}_{67}, \vec{v}_6, \vec{F}_6, \vec{T}_{G5}, \vec{F}_{G5}$
$B_7$	$\check{J}_7$	$\vec{\omega}_7, \vec{T}_7, \vec{H}_7, \vec{r}_{76}, \vec{v}_7, \vec{F}_7, \vec{T}_{G6}, \vec{F}_{G6}$

joint constraint equations will be represented in the frame of the preceding body of the associated joint. Table 2.1 informs us regarding the coordinate frames which the vectors forming the motion equations are represented in.

During the transformation from vector to matrix equations, an equivalent operation for cross product must be defined. In order to represent cross product in the matrix form, tilde ( $\sim$ ) operator is utilized which can be defined as:

$$\tilde{x} = \begin{bmatrix} 0 & -x_3 & x_2 \\ x_3 & 0 & -x_1 \\ -x_2 & x_1 & 0 \end{bmatrix} \quad (2.27)$$

Also, transformation matrices have to be defined. The matrix that transforms vectors from the coordinate frame of  $B_i$  to the coordinate frame of  $B_j$  is represented as  $\hat{C}_{ji}$  and described by:

$$\hat{C}_{ji} = \begin{bmatrix} \cos \theta_m & \sin \theta_m & 0 \\ -\sin \theta_m & \cos \theta_m & 0 \\ 0 & 0 & 1 \end{bmatrix} \quad (2.28)$$

for solar array 1;  $j = 4, 3, 2$  when  $i = 3, 2, 1$  and  $m = 3, 2, 1$ . For solar array 2;  $j = 7, 6, 5$  when  $i = 6, 5, 1$  and  $m = 6, 5, 4$ . Furthermore;

$$\hat{C}_{ij} = \hat{C}_{ji}^T \quad (2.29)$$

Having defined the transformation matrices, we may write the Euler's equation for body  $B_1$

as:

$$\hat{J}_1 \dot{\omega}_1 = \bar{T}_1 - \tilde{\omega}_1 \bar{H}_1 + \hat{C}_{12} \bar{T}_{G1} + \hat{C}_{15} \bar{T}_{G4} + \tilde{r}_{12} \hat{C}_{12} \bar{F}_{G1} + \tilde{r}_{15} \hat{C}_{15} \bar{F}_{G4} \quad (2.30)$$

similarly, for body  $B_2$ :

$$\hat{J}_2 \dot{\omega}_2 = \bar{T}_2 - \tilde{\omega}_2 \bar{H}_2 - \bar{T}_{G1} + \hat{C}_{23} \bar{T}_{G2} - \tilde{r}_{21} \bar{F}_{G1} + \tilde{r}_{23} \hat{C}_{23} \bar{F}_{G2} \quad (2.31)$$

also for body  $B_3$ :

$$\hat{J}_3 \dot{\omega}_3 = \bar{T}_3 - \tilde{\omega}_3 \bar{H}_3 - \bar{T}_{G2} + \hat{C}_{34} \bar{T}_{G3} - \tilde{r}_{32} \bar{F}_{G2} + \tilde{r}_{34} \hat{C}_{34} \bar{F}_{G3} \quad (2.32)$$

and finally for body  $B_4$ :

$$\hat{J}_4 \dot{\omega}_4 = \bar{T}_4 - \tilde{\omega}_4 \bar{H}_4 - \bar{T}_{G3} - \tilde{r}_{43} \bar{F}_{G3} \quad (2.33)$$

continuing on with the Euler equations for the members of solar array 2, for  $B_5$ :

$$\hat{J}_5 \dot{\omega}_5 = \bar{T}_5 - \tilde{\omega}_5 \bar{H}_5 - \bar{T}_{G4} + \hat{C}_{56} \bar{T}_{G5} - \tilde{r}_{51} \bar{F}_{G4} + \tilde{r}_{56} \hat{C}_{56} \bar{F}_{G5} \quad (2.34)$$

also for  $B_6$ :

$$\hat{J}_6 \dot{\omega}_6 = \bar{T}_6 - \tilde{\omega}_6 \bar{H}_6 - \bar{T}_{G5} + \hat{C}_{67} \bar{T}_{G6} - \tilde{r}_{65} \bar{F}_{G5} + \tilde{r}_{67} \hat{C}_{67} \bar{F}_{G6} \quad (2.35)$$

and ultimately for  $B_7$ :

$$\hat{J}_7 \dot{\omega}_7 = \bar{T}_7 - \tilde{\omega}_7 \bar{H}_7 - \bar{T}_{G6} - \tilde{r}_{76} \bar{F}_{G6} \quad (2.36)$$

Newton's equations for the system members are obtained as follows. For  $B_1$ :

$$m_1 \tilde{\omega}_1 \bar{v}_1 + m_1 \dot{\bar{v}}_1 = \bar{F}_1 + \hat{C}_{12} \bar{F}_{G1} + \hat{C}_{15} \bar{F}_{G4} \quad (2.37)$$

also for  $B_2$ :

$$m_2\tilde{\omega}_2\bar{v}_2 + m_2\dot{\bar{v}}_2 = \bar{F}_2 - \bar{F}_{G1} + \hat{C}_{23}\bar{F}_{G2} \quad (2.38)$$

similarly for  $B_3$ :

$$m_3\tilde{\omega}_3\bar{v}_3 + m_3\dot{\bar{v}}_3 = \bar{F}_3 - \bar{F}_{G2} + \hat{C}_{34}\bar{F}_{G3} \quad (2.39)$$

and for  $B_4$ :

$$m_4\tilde{\omega}_4\bar{v}_4 + m_4\dot{\bar{v}}_4 = \bar{F}_4 - \bar{F}_{G3} \quad (2.40)$$

for  $B_5$ :

$$m_5\tilde{\omega}_5\bar{v}_5 + m_5\dot{\bar{v}}_5 = \bar{F}_5 - \bar{F}_{G4} + \hat{C}_{56}\bar{F}_{G5} \quad (2.41)$$

for  $B_6$ :

$$m_6\tilde{\omega}_6\bar{v}_6 + m_6\dot{\bar{v}}_6 = \bar{F}_6 - \bar{F}_{G5} + \hat{C}_{67}\bar{F}_{G6} \quad (2.42)$$

and lastly for  $B_7$ :

$$m_7\tilde{\omega}_7\bar{v}_7 + m_7\dot{\bar{v}}_7 = \bar{F}_7 - \bar{F}_{G6} \quad (2.43)$$

The joint constraint criterion given in eq.(2.22) can be written in matrix notation as follows:

$$\dot{\bar{v}}_i - \tilde{r}_{ij}\dot{\bar{\omega}}_i - \hat{C}_{ij}\dot{\bar{v}}_j + \hat{C}_{ij}\tilde{r}_{ji}\dot{\bar{\omega}}_j = \hat{C}_{ij}\tilde{\omega}_j\tilde{\omega}_j\tilde{r}_{ji} - \tilde{\omega}_i\tilde{\omega}_i\tilde{r}_{ij} + \hat{C}_{ij}\tilde{\omega}_j\bar{v}_j - \tilde{\omega}_i\bar{v}_i \quad (2.44)$$

Similarly, eq.(2.25) can be written in matrix notation for all joints as:

$$\dot{\bar{\omega}}_j - \hat{C}_{ji}\dot{\bar{\omega}}_i - \dot{\bar{\omega}}_{j/i} = \tilde{\omega}_j\bar{\omega}_{j/i} \quad (2.45)$$

Lastly, eq.(2.26) in matrix rotation is:

$$\begin{bmatrix} 0 & 0 & 1 \end{bmatrix} \bar{T}_{Gm} = f_{spring,m}(\theta_m) \quad (2.46)$$

writing eq.(2.46) for the preceding and succeeding bodies of all joint, a complete set of linear algebraic equations that describe the motion of a multi-body system will be obtained.

**Linear algebraic motion equation** Assuming that:

$$\bar{y} = \begin{bmatrix} \dot{\omega}_1^T \dots \dot{\omega}_n^T & \dot{v}_1^T \dots \dot{v}_n^T & \bar{F}_{G1}^T \dots \bar{F}_{Gm}^T & \bar{T}_{G1}^T \dots \bar{T}_{Gm}^T & \ddot{\theta}_1 \dots \ddot{\theta}_m \end{bmatrix}^T \quad (2.47)$$

The equations from (2.30) to (2.46) can be written in the form:

$$\hat{A}\bar{y} = \bar{u} \quad (2.48)$$

Writing eq.(2.48) in more detail:

$$\begin{bmatrix} \hat{A}_{11} & \hat{A}_{12} & \hat{A}_{13} & \hat{A}_{14} & \hat{A}_{15} \\ \hat{A}_{21} & \hat{A}_{22} & \hat{A}_{23} & \hat{A}_{24} & \hat{A}_{25} \\ \hat{A}_{31} & \hat{A}_{32} & \hat{A}_{33} & \hat{A}_{34} & \hat{A}_{35} \\ \hat{A}_{41} & \hat{A}_{42} & \hat{A}_{43} & \hat{A}_{44} & \hat{A}_{45} \\ \hat{A}_{51} & \hat{A}_{52} & \hat{A}_{53} & \hat{A}_{54} & \hat{A}_{55} \end{bmatrix} \begin{bmatrix} \bar{y}_{11} \\ \bar{y}_{21} \\ \bar{y}_{31} \\ \bar{y}_{41} \\ \bar{y}_{51} \end{bmatrix} = \begin{bmatrix} \bar{u}_{11} \\ \bar{u}_{21} \\ \bar{u}_{31} \\ \bar{u}_{41} \\ \bar{u}_{51} \end{bmatrix} \quad (2.49)$$

note that:

$$\bar{y}_{11} = \begin{bmatrix} \dot{\omega}_1 \\ \vdots \\ \dot{\omega}_n \end{bmatrix} \quad (2.50)$$

together with:

$$\bar{y}_{21} = \begin{bmatrix} \dot{\bar{v}}_1 \\ \vdots \\ \dot{\bar{v}}_n \end{bmatrix} \quad (2.51)$$

and:

$$\bar{y}_{31} = \begin{bmatrix} \bar{F}_{G1} \\ \vdots \\ \bar{F}_{Gm} \end{bmatrix} \quad (2.52)$$

also:

$$\bar{y}_{41} = \begin{bmatrix} \bar{T}_{G1} \\ \vdots \\ \bar{T}_{Gm} \end{bmatrix} \quad (2.53)$$

lastly:

$$\bar{y}_{51} = \begin{bmatrix} \ddot{\theta}_1 \\ \vdots \\ \ddot{\theta}_m \end{bmatrix} \quad (2.54)$$

Now we may fill in the elements of  $\hat{A}_{11}$ ,  $\hat{A}_{12}$ ,  $\hat{A}_{13}$ ,  $\hat{A}_{14}$  and  $\hat{A}_{15}$  and  $\bar{u}_{11}$  with the help of Euler's equations from eq.(2.30) to eq.(2.36).  $\hat{A}_{11}$  becomes:

$$\hat{A}_{11} = \begin{bmatrix} \hat{J}_1 & \hat{0} & \hat{0} & \hat{0} & \hat{0} & \hat{0} & \hat{0} \\ \hat{0} & \hat{J}_2 & \hat{0} & \hat{0} & \hat{0} & \hat{0} & \hat{0} \\ \hat{0} & \hat{0} & \hat{J}_3 & \hat{0} & \hat{0} & \hat{0} & \hat{0} \\ \hat{0} & \hat{0} & \hat{0} & \hat{J}_4 & \hat{0} & \hat{0} & \hat{0} \\ \hat{0} & \hat{0} & \hat{0} & \hat{0} & \hat{J}_5 & \hat{0} & \hat{0} \\ \hat{0} & \hat{0} & \hat{0} & \hat{0} & \hat{0} & \hat{J}_6 & \hat{0} \\ \hat{0} & \hat{0} & \hat{0} & \hat{0} & \hat{0} & \hat{0} & \hat{J}_7 \end{bmatrix} \quad (2.55)$$

where  $\hat{0}$  is a matrix formed entirely of zeros. Similarly,  $\hat{A}_{12}$  is a 21 by 21 matrix composed entirely of zeros since  $\left(\frac{d\vec{v}_n}{dt}\right)_{\mathbb{F}_n}$  is not present in Euler's equations.  $\hat{A}_{13}$  is:

$$\hat{A}_{13} = \begin{bmatrix} -\tilde{r}_{12}\hat{C}_{12} & \hat{0} & \hat{0} & -\tilde{r}_{15}\hat{C}_{15} & \hat{0} & \hat{0} \\ \tilde{r}_{21} & -\tilde{r}_{23}\hat{C}_{23} & \hat{0} & \hat{0} & \hat{0} & \hat{0} \\ \hat{0} & \tilde{r}_{32} & -\tilde{r}_{34}\hat{C}_{34} & \hat{0} & \hat{0} & \hat{0} \\ \hat{0} & \hat{0} & \tilde{r}_{43} & \hat{0} & \hat{0} & \hat{0} \\ \hat{0} & \hat{0} & \hat{0} & \tilde{r}_{51} & -\tilde{r}_{56}\hat{C}_{56} & \hat{0} \\ \hat{0} & \hat{0} & \hat{0} & \hat{0} & \tilde{r}_{65} & -\tilde{r}_{67}\hat{C}_{67} \\ \hat{0} & \hat{0} & \hat{0} & \hat{0} & \hat{0} & \tilde{r}_{76} \end{bmatrix} \quad (2.56)$$

also  $\hat{A}_{14}$  is:

$$\hat{A}_{14} = \begin{bmatrix} -\hat{C}_{12} & \hat{0} & \hat{0} & -\hat{C}_{15} & \hat{0} & \hat{0} \\ \hat{I} & -\hat{C}_{23} & \hat{0} & \hat{0} & \hat{0} & \hat{0} \\ \hat{0} & \hat{I} & -\hat{C}_{34} & \hat{0} & \hat{0} & \hat{0} \\ \hat{0} & \hat{0} & \hat{I} & \hat{0} & \hat{0} & \hat{0} \\ \hat{0} & \hat{0} & \hat{0} & \hat{I} & -\hat{C}_{56} & \hat{0} \\ \hat{0} & \hat{0} & \hat{0} & \hat{0} & \hat{I} & -\hat{C}_{67} \\ \hat{0} & \hat{0} & \hat{0} & \hat{0} & \hat{0} & \hat{I} \end{bmatrix} \quad (2.57)$$

Because  $\ddot{\theta}_m$  is not explicitly stated in Euler's equations,  $\hat{A}_{15}$  is a zero matrix with size 21 by 6. Furthermore,  $\bar{u}_{11}$  becomes:

$$\bar{u}_{11} = \begin{bmatrix} \bar{T}_1 - \tilde{\omega}_1 (\hat{J}_1 \bar{\omega}_1) \\ \bar{T}_2 - \tilde{\omega}_2 (\hat{J}_2 \bar{\omega}_2) \\ \bar{T}_3 - \tilde{\omega}_3 (\hat{J}_3 \bar{\omega}_3) \\ \bar{T}_4 - \tilde{\omega}_4 (\hat{J}_4 \bar{\omega}_4) \\ \bar{T}_5 - \tilde{\omega}_5 (\hat{J}_5 \bar{\omega}_5) \\ \bar{T}_6 - \tilde{\omega}_6 (\hat{J}_6 \bar{\omega}_6) \\ \bar{T}_7 - \tilde{\omega}_7 (\hat{J}_7 \bar{\omega}_7) \end{bmatrix} \quad (2.58)$$

The elements of  $\hat{A}_{21}$ ,  $\hat{A}_{22}$ ,  $\hat{A}_{23}$ ,  $\hat{A}_{24}$ ,  $\hat{A}_{25}$  and  $\bar{u}_{21}$  can be obtained from Newton's equations

from eq.(2.37) to eq.(2.43). Due to the fact that  $\left(\frac{d\vec{\omega}_n}{dt}\right)_{\mathbb{F}_n}$  is not present in Newton's equations  $\hat{A}_{21}$  becomes a 21 by 21 zero matrix as was in the case of  $\hat{A}_{12}$ .  $\hat{A}_{22}$  becomes:

$$\hat{A}_{22} = \begin{bmatrix} m_1 \hat{I} & \hat{0} & \hat{0} & \hat{0} & \hat{0} & \hat{0} & \hat{0} \\ \hat{0} & m_2 \hat{I} & \hat{0} & \hat{0} & \hat{0} & \hat{0} & \hat{0} \\ \hat{0} & \hat{0} & m_3 \hat{I} & \hat{0} & \hat{0} & \hat{0} & \hat{0} \\ \hat{0} & \hat{0} & \hat{0} & m_4 \hat{I} & \hat{0} & \hat{0} & \hat{0} \\ \hat{0} & \hat{0} & \hat{0} & \hat{0} & m_5 \hat{I} & \hat{0} & \hat{0} \\ \hat{0} & \hat{0} & \hat{0} & \hat{0} & \hat{0} & m_6 \hat{I} & \hat{0} \\ \hat{0} & \hat{0} & \hat{0} & \hat{0} & \hat{0} & \hat{0} & m_7 \hat{I} \end{bmatrix} \quad (2.59)$$

where  $\hat{I}$  is the identity matrix.  $\hat{A}_{23}$  is:

$$\hat{A}_{23} = \begin{bmatrix} -\hat{C}_{12} & \hat{0} & \hat{0} & -\hat{C}_{15} & \hat{0} & \hat{0} \\ \hat{I} & -\hat{C}_{23} & \hat{0} & \hat{0} & \hat{0} & \hat{0} \\ \hat{0} & \hat{I} & -\hat{C}_{34} & \hat{0} & \hat{0} & \hat{0} \\ \hat{0} & \hat{0} & \hat{I} & \hat{0} & \hat{0} & \hat{0} \\ \hat{0} & \hat{0} & \hat{0} & \hat{I} & -\hat{C}_{56} & \hat{0} \\ \hat{0} & \hat{0} & \hat{0} & \hat{0} & \hat{I} & -\hat{C}_{67} \\ \hat{0} & \hat{0} & \hat{0} & \hat{0} & \hat{0} & \hat{I} \end{bmatrix} \quad (2.60)$$

Since  $\vec{T}_{Gm}$  is not present in the Newton's equations,  $\hat{A}_{24}$  is a 21 by 18 zero matrix. Similarly, since  $\ddot{\theta}_m$  does not exist explicitly in Newton's equations  $\hat{A}_{25}$  is also a zero matrix (21 by 6). Moreover,  $\bar{u}_{21}$  becomes:

$$\begin{bmatrix} \bar{F}_1 - m_1 \tilde{\omega}_1 \bar{v}_1 \\ \bar{F}_2 - m_2 \tilde{\omega}_2 \bar{v}_2 \\ \bar{F}_3 - m_3 \tilde{\omega}_3 \bar{v}_3 \\ \bar{F}_4 - m_4 \tilde{\omega}_4 \bar{v}_4 \\ \bar{F}_5 - m_5 \tilde{\omega}_5 \bar{v}_5 \\ \bar{F}_6 - m_6 \tilde{\omega}_6 \bar{v}_6 \\ \bar{F}_7 - m_7 \tilde{\omega}_7 \bar{v}_7 \end{bmatrix} \quad (2.61)$$

Joint constraint equations given in general form in eq.(2.44) can be treated in order to obtain the elements for  $\hat{A}_{31}$ ,  $\hat{A}_{32}$ ,  $\hat{A}_{33}$ ,  $\hat{A}_{34}$ ,  $\hat{A}_{35}$  and  $\bar{u}_{31}$ .  $\hat{A}_{31}$  is:

$$\hat{A}_{31} = \begin{bmatrix} -\tilde{r}_{12} & \hat{C}_{12}\tilde{r}_{21} & \hat{0} & \hat{0} & \hat{0} & \hat{0} & \hat{0} \\ \hat{0} & -\tilde{r}_{23} & \hat{C}_{23}\tilde{r}_{32} & \hat{0} & \hat{0} & \hat{0} & \hat{0} \\ \hat{0} & \hat{0} & -\tilde{r}_{34} & \hat{C}_{34}\tilde{r}_{43} & \hat{0} & \hat{0} & \hat{0} \\ -\tilde{r}_{15} & \hat{0} & \hat{0} & \hat{0} & \hat{C}_{15}\tilde{r}_{51} & \hat{0} & \hat{0} \\ \hat{0} & \hat{0} & \hat{0} & \hat{0} & -\tilde{r}_{56} & \hat{C}_{56}\tilde{r}_{65} & \hat{0} \\ \hat{0} & \hat{0} & \hat{0} & \hat{0} & \hat{0} & -\tilde{r}_{67} & \hat{C}_{67}\tilde{r}_{76} \end{bmatrix} \quad (2.62)$$

Moreover,  $\hat{A}_{32}$  is obtained as:

$$\hat{A}_{32} = \begin{bmatrix} \hat{I} & -\hat{C}_{12} & \hat{0} & \hat{0} & \hat{0} & \hat{0} & \hat{0} \\ \hat{0} & \hat{I} & -\hat{C}_{23} & \hat{0} & \hat{0} & \hat{0} & \hat{0} \\ \hat{0} & \hat{0} & \hat{I} & -\hat{C}_{34} & \hat{0} & \hat{0} & \hat{0} \\ \hat{I} & \hat{0} & \hat{0} & \hat{0} & -\hat{C}_{15} & \hat{0} & \hat{0} \\ \hat{0} & \hat{0} & \hat{0} & \hat{0} & \hat{I} & -\hat{C}_{56} & \hat{0} \\ \hat{0} & \hat{0} & \hat{0} & \hat{0} & \hat{0} & \hat{I} & -\hat{C}_{67} \end{bmatrix} \quad (2.63)$$

Since  $\vec{F}_{Gm}$  is not present in joint constraint equations,  $\hat{A}_{33}$  is a 18 by 18 zero matrix. Additionally,  $\hat{A}_{34}$  (18 by 18) and  $\hat{A}_{35}$  (18 by 6) are also zero matrices.  $\bar{u}_{31}$  becomes:

$$\bar{u}_{31} = \begin{bmatrix} \hat{C}_{12}\tilde{\omega}_2\tilde{\omega}_2\tilde{r}_{21} + \hat{C}_{12}\tilde{\omega}_2\tilde{v}_2 - \tilde{\omega}_1\tilde{\omega}_1\tilde{r}_{12} - \tilde{\omega}_1\tilde{v}_1 \\ \hat{C}_{23}\tilde{\omega}_3\tilde{\omega}_3\tilde{r}_{32} + \hat{C}_{23}\tilde{\omega}_3\tilde{v}_3 - \tilde{\omega}_2\tilde{\omega}_2\tilde{r}_{23} - \tilde{\omega}_2\tilde{v}_2 \\ \hat{C}_{34}\tilde{\omega}_4\tilde{\omega}_4\tilde{r}_{43} + \hat{C}_{34}\tilde{\omega}_4\tilde{v}_4 - \tilde{\omega}_3\tilde{\omega}_3\tilde{r}_{34} - \tilde{\omega}_3\tilde{v}_3 \\ \hat{C}_{15}\tilde{\omega}_5\tilde{\omega}_5\tilde{r}_{51} + \hat{C}_{15}\tilde{\omega}_5\tilde{v}_5 - \tilde{\omega}_1\tilde{\omega}_1\tilde{r}_{15} - \tilde{\omega}_1\tilde{v}_1 \\ \hat{C}_{56}\tilde{\omega}_6\tilde{\omega}_6\tilde{r}_{65} + \hat{C}_{56}\tilde{\omega}_6\tilde{v}_6 - \tilde{\omega}_5\tilde{\omega}_5\tilde{r}_{56} - \tilde{\omega}_5\tilde{v}_5 \\ \hat{C}_{67}\tilde{\omega}_7\tilde{\omega}_7\tilde{r}_{76} + \hat{C}_{67}\tilde{\omega}_7\tilde{v}_7 - \tilde{\omega}_6\tilde{\omega}_6\tilde{r}_{67} - \tilde{\omega}_6\tilde{v}_6 \end{bmatrix} \quad (2.64)$$

Writing eq.(2.45) for all the joints, the elements for  $\hat{A}_{41}$ ,  $\hat{A}_{42}$ ,  $\hat{A}_{43}$ ,  $\hat{A}_{44}$ ,  $\hat{A}_{45}$  and  $\bar{u}_{41}$  can be obtained. Consequently,  $\hat{A}_{41}$  takes the following form:



$$\hat{A}_{41} = \begin{bmatrix} -\hat{C}_{12} & \hat{1} & \hat{0} & \hat{0} & \hat{0} & \hat{0} & \hat{0} \\ \hat{0} & -\hat{C}_{23} & \hat{1} & \hat{0} & \hat{0} & \hat{0} & \hat{0} \\ \hat{0} & \hat{0} & -\hat{C}_{34} & \hat{1} & \hat{0} & \hat{0} & \hat{0} \\ -\hat{C}_{15} & \hat{0} & \hat{0} & \hat{0} & \hat{1} & \hat{0} & \hat{0} \\ \hat{0} & \hat{0} & \hat{0} & \hat{0} & -\hat{C}_{56} & \hat{1} & \hat{0} \\ \hat{0} & \hat{0} & \hat{0} & \hat{0} & \hat{0} & -\hat{C}_{67} & \hat{1} \end{bmatrix} \quad (2.65)$$

$\hat{A}_{42}$  (18 by 21),  $\hat{A}_{43}$  (18 by 21) and  $\hat{A}_{44}$  (18 by 18) are zero matrices.  $\hat{A}_{45}$  is:

$$\hat{A}_{45} = \begin{bmatrix} 0 & 0 & 0 & 0 & 0 & 0 \\ 0 & 0 & 0 & 0 & 0 & 0 \\ -1 & 0 & 0 & 0 & 0 & 0 \\ 0 & 0 & 0 & 0 & 0 & 0 \\ 0 & 0 & 0 & 0 & 0 & 0 \\ 0 & -1 & 0 & 0 & 0 & 0 \\ 0 & 0 & 0 & 0 & 0 & 0 \\ 0 & 0 & 0 & 0 & 0 & 0 \\ 0 & 0 & -1 & 0 & 0 & 0 \\ 0 & 0 & 0 & 0 & 0 & 0 \\ 0 & 0 & 0 & 0 & 0 & 0 \\ 0 & 0 & 0 & 0 & 0 & 0 \\ 0 & 0 & 0 & -1 & 0 & 0 \\ 0 & 0 & 0 & 0 & 0 & 0 \\ 0 & 0 & 0 & 0 & 0 & 0 \\ 0 & 0 & 0 & 0 & -1 & 0 \\ 0 & 0 & 0 & 0 & 0 & 0 \\ 0 & 0 & 0 & 0 & 0 & 0 \\ 0 & 0 & 0 & 0 & 0 & -1 \end{bmatrix} \quad (2.66)$$

and the corresponding input  $\bar{u}_{41}$  is:

$$\bar{u}_{41} = \begin{bmatrix} \tilde{\omega}_2 \begin{bmatrix} 0 & 0 & \dot{\theta}_1 \end{bmatrix}^T \\ \tilde{\omega}_3 \begin{bmatrix} 0 & 0 & \dot{\theta}_2 \end{bmatrix}^T \\ \tilde{\omega}_4 \begin{bmatrix} 0 & 0 & \dot{\theta}_3 \end{bmatrix}^T \\ \tilde{\omega}_5 \begin{bmatrix} 0 & 0 & \dot{\theta}_4 \end{bmatrix}^T \\ \tilde{\omega}_6 \begin{bmatrix} 0 & 0 & \dot{\theta}_5 \end{bmatrix}^T \\ \tilde{\omega}_7 \begin{bmatrix} 0 & 0 & \dot{\theta}_6 \end{bmatrix}^T \end{bmatrix} \quad (2.67)$$

Lastly,  $\hat{A}_{51}$  (6 by 21),  $\hat{A}_{52}$  (6 by 21),  $\hat{A}_{53}$  (6 by 18) and  $\hat{A}_{55}$  (6 by 6) are zero matrices.  $\hat{A}_{54}$  becomes:

$$\hat{A}_{54} = \begin{bmatrix} \begin{bmatrix} 0 & 0 & 1 \end{bmatrix} & \bar{0}^T & \bar{0}^T & \bar{0}^T & \bar{0}^T & \bar{0}^T \\ \bar{0}^T & \begin{bmatrix} 0 & 0 & 1 \end{bmatrix} & \bar{0}^T & \bar{0}^T & \bar{0}^T & \bar{0}^T \\ \bar{0}^T & \bar{0}^T & \begin{bmatrix} 0 & 0 & 1 \end{bmatrix} & \bar{0}^T & \bar{0}^T & \bar{0}^T \\ \bar{0}^T & \bar{0}^T & \bar{0}^T & \begin{bmatrix} 0 & 0 & 1 \end{bmatrix} & \bar{0}^T & \bar{0}^T \\ \bar{0}^T & \bar{0}^T & \bar{0}^T & \bar{0}^T & \begin{bmatrix} 0 & 0 & 1 \end{bmatrix} & \bar{0}^T \\ \bar{0}^T & \bar{0}^T & \bar{0}^T & \bar{0}^T & \bar{0}^T & \begin{bmatrix} 0 & 0 & 1 \end{bmatrix} \end{bmatrix} \quad (2.68)$$

Finally, the input  $\bar{u}_{51}$  is:

$$\bar{u}_{51} = \begin{bmatrix} f_{spring,1}(\theta_1) \\ f_{spring,2}(\theta_2) \\ f_{spring,3}(\theta_3) \\ f_{spring,4}(\theta_4) \\ f_{spring,5}(\theta_5) \\ f_{spring,6}(\theta_6) \end{bmatrix} \quad (2.69)$$

Here,  $f_{spring,m}$  is the function embodying the mathematical model of the torsional spring at joint  $m$ . Having obtained all the elements present in eq.(2.49), we may now solve for  $\bar{y}$ :

$$\bar{y} = \hat{A}^{-1} \bar{u} \quad (2.70)$$

Table 2.2: Parameters used in multi-body model verification

Parameter	Value	Unit
$m_{main}$	420	kg
$L_{main}$	1	m
$W_{main}$	1	m
$H_{main}$	1.4	m
$J_{main} (B_1)$	$\begin{bmatrix} 103.6 & 0 & 0 \\ 0 & 103.6 & 0 \\ 0 & 0 & 70 \end{bmatrix}$	kg-m <sup>2</sup>
$m_{yoke}$	5	kg
$L_{yoke}$	0.5	m
$W_{yoke}$	0.04	m
$H_{yoke}$	0.5	m
$J_{yoke} (B_2, B_5)$	$\begin{bmatrix} 0.1048 & 0 & 0 \\ 0 & 0.2083 & 0 \\ 0 & 0 & 0.1048 \end{bmatrix}$	kg-m <sup>2</sup>
$m_{panel}$	10	kg
$L_{panel}$	1.0	m
$W_{panel}$	0.02	m
$H_{panel}$	1.1	m
$J_{panel} (B_3, B_4, B_6, B_7)$	$\begin{bmatrix} 1.0087 & 0 & 0 \\ 0 & 1.8417 & 0 \\ 0 & 0 & 0.8337 \end{bmatrix}$	kg-m <sup>2</sup>
$k_{spring}$	2	Nm/rad

**Verification of the multi-body model** In order to verify the multi-body model obtained, an identical model was built with the Simulink's SimMechanics tool. Parameters given in Table 2.2 were used. Note that there exist no deviations in geometric and mass properties within the categories main body, panel and yoke themselves. Outputs  $\left(\frac{d\vec{\omega}_1}{dt}\right)_{\mathbb{F}_1}$ ,  $\vec{\omega}_1$  and  $\theta_m$  of the recently obtained mathematical model and the SimMechanics model were compared. Both systems were simulated for 100 seconds with a time step of 0.1 s. Moreover, all initial conditions were assumed to equal zero.

Comparisons of  $\left(\frac{d\vec{\omega}_1}{dt}\right)_{\mathbb{F}_1}$ ,  $\vec{\omega}_1$  and  $\theta_m$  were made by the usage of absolute errors. Absolute error is defined as:

$$e = |x_{MM} - x_{SM}| \quad (2.71)$$

where  $e$  is the absolute error,  $x_{SM}$  is the value of the variable calculated by the SimMechanics model and  $X_{MM}$  is the value calculated by using the recently obtained mathematical model.

0.5 Nm was assumed to be applied to the yaw axis of body  $B_1$  for 100 s. Here, one must note that the largest torque that can be supplied by the current actuators in the yaw axis is 0.3919 Nm, by assuming that each reaction wheel can produce at most 0.24 Nm and the steering law given in eq.(2.89) is used. The yaw axis was considered since it is the axis where applied torques can easily excite the panels (due to the fact that all the revolute joints are aligned in that direction). One additional note regarding the torque duration is that even during a 60 ° roll, 60 ° pitch and 0 ° yaw slew maneuver; the longest duration of the maximum torque (i.e. 0.3919 Nm) does not exceed 50 s. Therefore, it can easily be inferred that this test case is rather harsh. The error history between the two simulation models, SimMechanics and the equations derived, are given in Figure 2.4, whereas errors in joint angles  $\theta_m$  are given in Figure 2.5 for solar array 1 and Figure 2.6 for solar array 2.

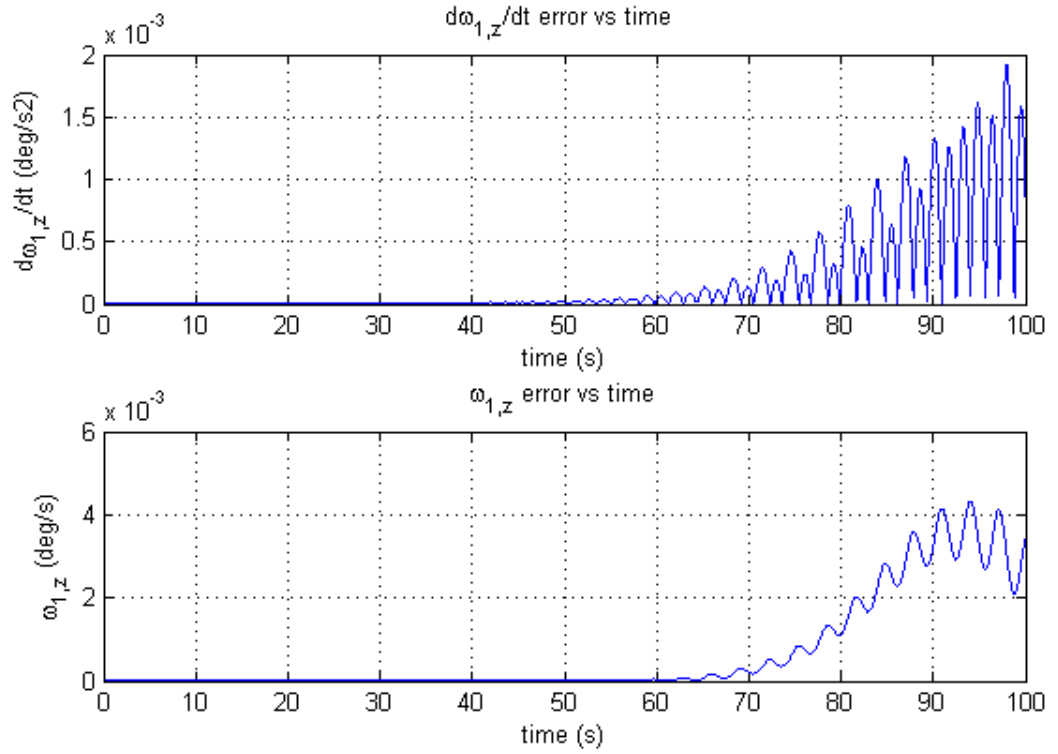


Figure 2.4: Angular acceleration and velocity error of  $B_1$

It can be observed from Figure 2.4 that errors for angular accelerations and velocities are in the order of  $10^{-3} \text{ }^\circ/\text{s}^2$  and  $10^{-3} \text{ }^\circ/\text{s}$  respectively, corresponding to 0.1 % and 0.04 % of the

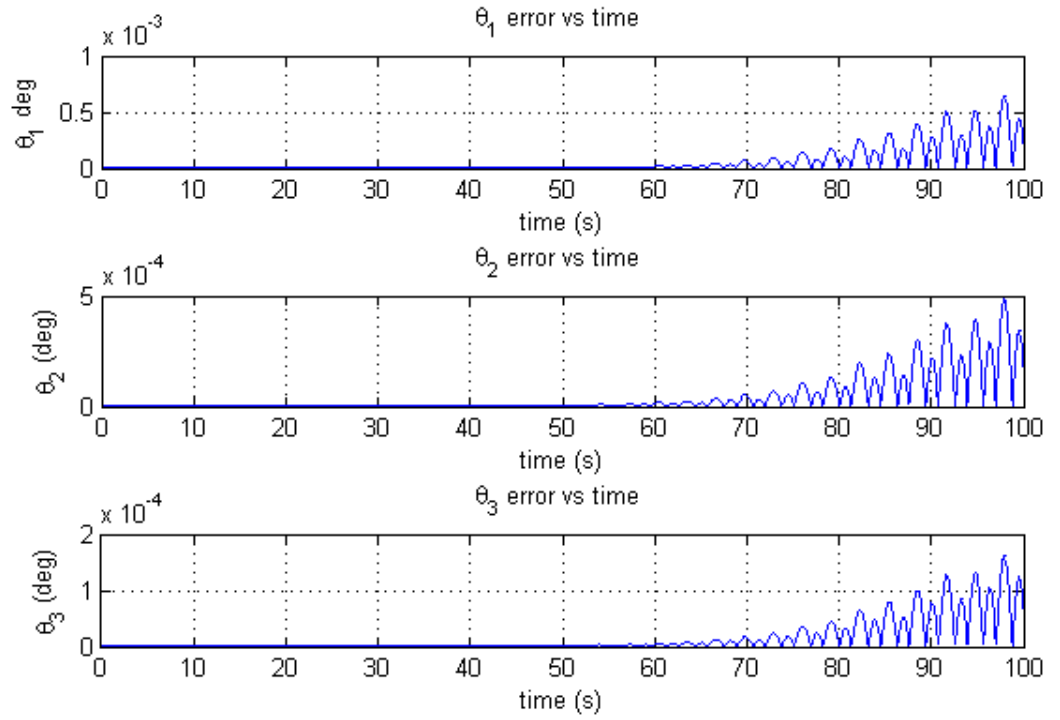


Figure 2.5: Angle errors of joints in solar array 1

maximum values of the variables. Similarly from Figures 2.5 and 2.6 it is seen that the errors for joints angles are as low as  $10^{-4}^\circ$  (0.025 % of the maximum value). Thus, the values obtained by the model developed are in close agreement with that of SimMechanics.

**Nonlinear spring model** It was assumed that after the initial deployment, the panel hinges lock into their configuration shown in Figure 2.1. It is furthermore assumed that even though the hinges are locked, there still exists room for panels to move; although it is small. When a panel rotates beyond this "free play" zone, the hinges hit the "hard stops" and a higher than usual restoring torque is applied in the opposite direction. The mathematical model of such a hinge system is as follows assuming that the free play zone is confined within  $-0.25^\circ$  and  $0.25^\circ$ :

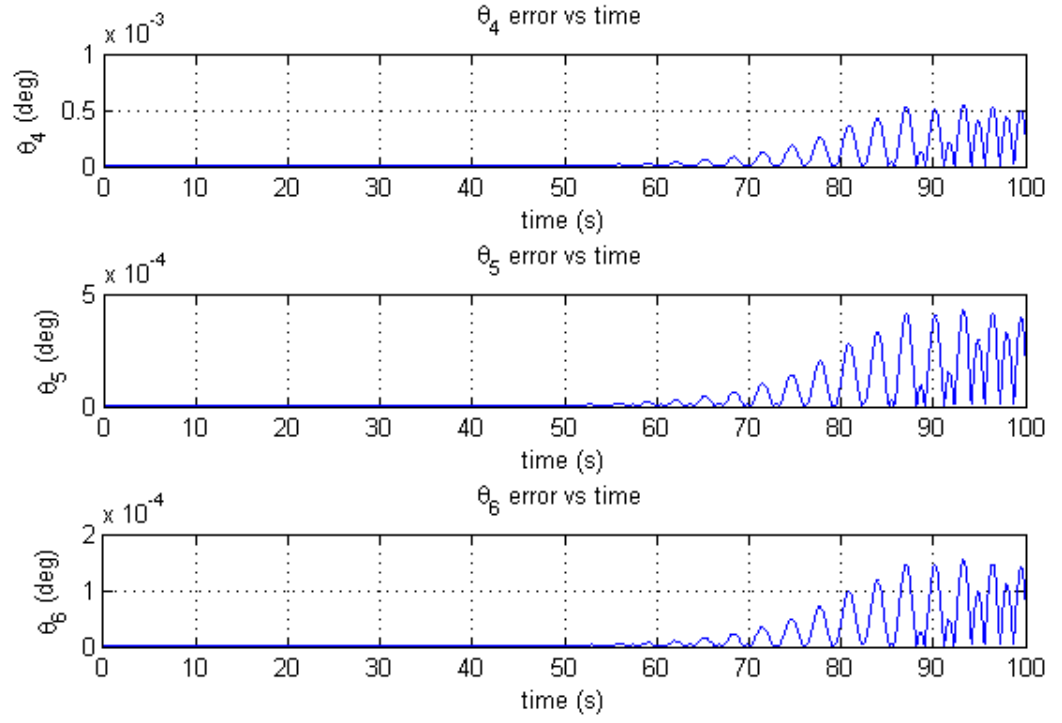


Figure 2.6: Angle errors of joints in solar array 2

$$f_{spring,m}(\theta_m) = \begin{cases} k_1\theta_m, & |\theta_m| \leq 0.25^\circ \\ k_2\theta_m - 0.428, & \theta_m > 0.25^\circ \\ k_2\theta_m + 0.428, & \theta_m < -0.25^\circ \end{cases} \quad (2.72)$$

where  $f_{spring,m}(\theta_m)$  is the function given previously in eq.(2.26).  $k_1$  is the spring constant in the free play zone and is equal to  $2 \text{ Nm/rad}$  whereas  $k_2$  equals to  $100 \text{ Nm/rad}$  and corresponds to the state when the hinge is in contact with the hard stops. Plot of eq.(2.72) is given in Figure 2.7.

## 2.2 Kinematics

Having obtained the expression for the angular acceleration both for the single and multi-body cases, we would next seek methods to represent the spacecraft angular orientation. For this

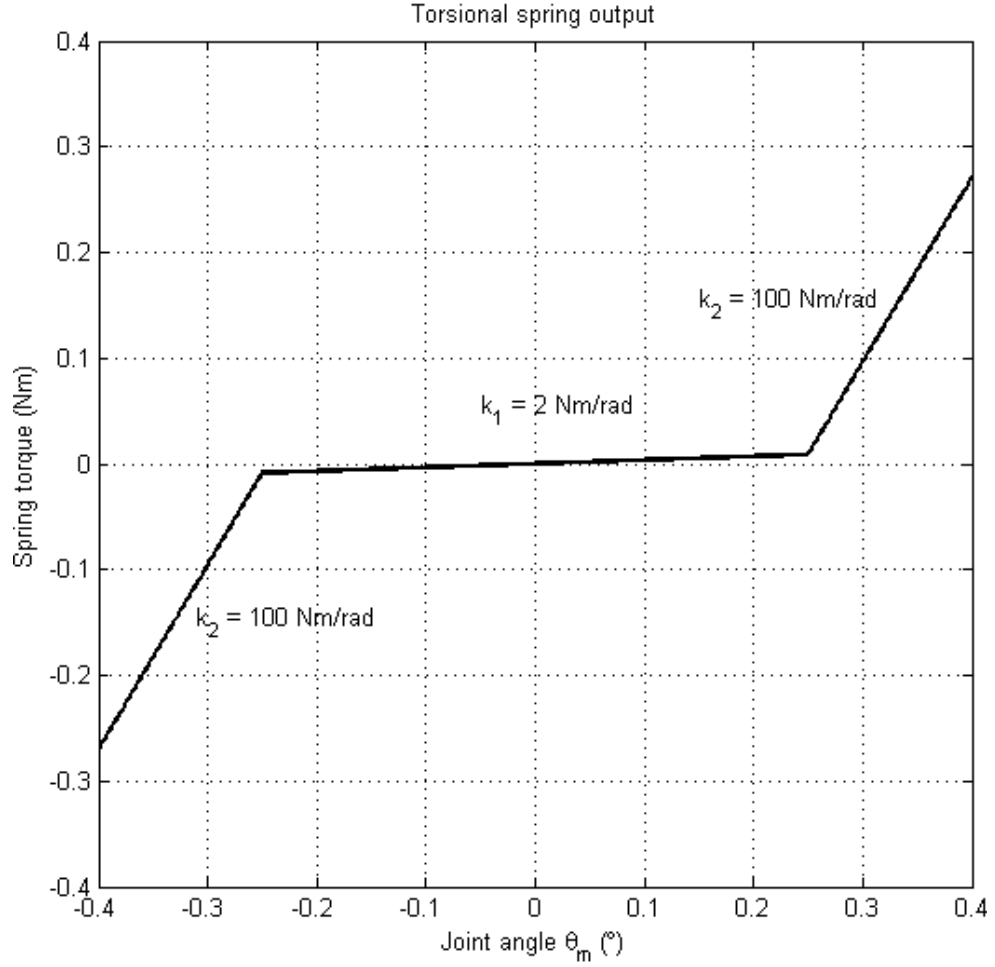


Figure 2.7: Angular displacement vs. Torque plot for torsional spring

purpose, a kinematic model is needed. Several methods exist for modeling rigid body kinematics such as DCM<sup>3</sup>, Euler angle and quaternion representations. In this model, quaternion representation is used since it avoids the singularities that result from various axes transformations that arise when DCM and Euler angle representations are utilized. The kinematic model for quaternion representation is<sup>[13]</sup>:

$$\dot{\bar{q}} = \frac{1}{2} \begin{bmatrix} 0 & \omega_z & -\omega_y & \omega_x \\ -\omega_z & 0 & \omega_x & \omega_y \\ \omega_y & -\omega_x & 0 & \omega_z \\ -\omega_x & -\omega_y & -\omega_z & 0 \end{bmatrix} \bar{q} \quad (2.73)$$

<sup>3</sup> Direction Cosine Matrix

The attitude of the spacecraft can be propagated in quaternions by the integration of eq.(2.73). Appendix A of Ref.[13] provides more detailed explanation of quaternion representation.

Even though quaternions are useful in representing spacecraft attitude, they are not easy to visualize. Thus, it is helpful to observe the corresponding Euler angles for physical interpretation. The transformation from quaternions to Euler angles is carried out by first obtaining the DCM from the quaternions<sup>[14]</sup>:

$$\hat{A} = \begin{bmatrix} q_1^2 - q_2^2 - q_3^2 + q_4^2 & 2(q_1q_2 + q_3q_4) & 2(q_1q_3 - q_2q_4) \\ 2(q_1q_2 - q_3q_4) & -q_1^2 + q_2^2 - q_3^2 + q_4^2 & 2(q_2q_3 + q_1q_4) \\ 2(q_1q_3 + q_2q_4) & 2(q_2q_3 - q_1q_4) & -q_1^2 - q_2^2 + q_3^2 + q_4^2 \end{bmatrix} \quad (2.74)$$

Then, the Euler angles are calculated from the DCM elements via the following identities:

$$\begin{aligned} \theta &= \arccos(A_{33}) \\ \varphi &= -\arctan\left(\frac{A_{31}}{A_{32}}\right) \\ \psi &= \arctan\left(\frac{A_{13}}{A_{23}}\right) \end{aligned} \quad (2.75)$$

Thus, the orientation of the spacecraft is obtained in terms of Euler angles whilst avoiding singularities in calculation. Note that even though dealing with quaternions save us from singularities in attitude propagation, singularities can still be encountered when transforming from quaternions to Euler angles, as evident from eq.(2.75). However, since in this study the maneuver angle is smaller than 90 °, singularities are not observed in simulations.

### 2.3 Actuators

The only actuator model employed in this study is the reaction wheel assembly consisting of four reaction wheels in tetrahedron configuration. The reorientation of the spacecraft is possible by the momentum exchange of these devices (Figure 2.8) with the spacecraft.

First, the model and operating principles of a single reaction wheel will be introduced followed by the reaction wheel cluster.





Figure 2.8: A typical reaction wheel unit

### 2.3.1 Reaction Wheel Model

A detailed reaction wheel model provided by Sidi<sup>[13]</sup> and is given in Figure 2.9. Desired angular momentum change is the input of the model whereas obtained angular momentum and its change is the output. The input is assumed to be quantized with 8 bit representation which provides a  $0.001875 \text{ Nm}$  of command resolution. The model consists of electrical and mechanical parts. Voltage and current being applied within the electrical portion of the model is limited to  $\pm 50 \text{ V}$  and  $\pm 1.8 \text{ A}$ . Similarly, in the mechanical part, the maximum torque output is also limited ( $\pm 0.24 \text{ Nm}$ ) and wheel saturation speed is also included in the model. Wheel is assumed to operate in the range of  $\pm 2500 \text{ rpm}$ .

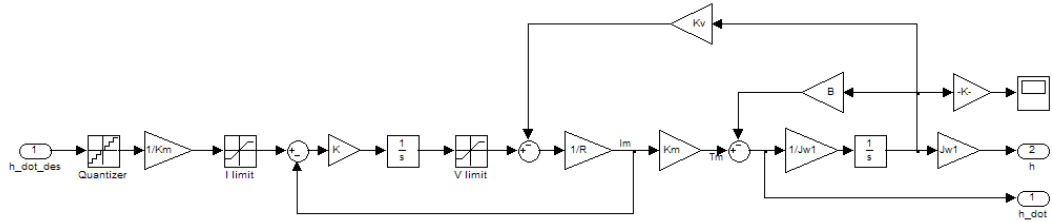


Figure 2.9: Reaction wheel Simulink model

The transfer function of the system is obtained as:

$$\frac{\dot{h}_{W,out}}{\dot{h}_{W,comm}} = \frac{\frac{K_C}{K_M} s}{\frac{R_M}{K_M} s^2 + \left( \frac{K_C}{K_M} + \frac{B R_M}{J_W K_M} + \frac{K_V}{J_W} \right) s + \frac{B K_C}{J_W K_M}} \quad (2.76)$$

where  $K_M$  is the motor torque coefficient,  $R_M$  is the electrical resistance,  $J_W$  is the wheel moment of inertia,  $B$  is the viscous damping,  $K_V$  is the back emf constant of the electric motor and  $K_C$  is the controller gain. Proportional plus integral speed control is utilized even though it is not evident from Figure 2.9. The reaction wheel is driven via applied voltage  $V_M$ . In the electrical part of the model, observe that the control law for defining the applied voltage is:

$$\left( \frac{\dot{h}_{W,comm}}{K_M} - i_M \right) \frac{K_C}{s} = V_M \quad (2.77)$$

Since it is known that,

$$i_M = \frac{T_M}{K_M} \quad (2.78)$$

where  $T_M$  is the torque applied by the motor. From the mechanical part of the model,

$$T_M = \dot{h}_{W,out} - B\omega_W \quad (2.79)$$

furthermore,

$$\begin{aligned} \dot{h}_{W,comm} &= J_W \dot{\omega}_{W,comm} \\ \dot{h}_{W,out} &= J_W \dot{\omega}_{W,out} \end{aligned} \quad (2.80)$$

Using equations (2.79) and (2.80), eq.(2.78) takes the following form:

$$J_W \frac{K_C}{K_M} (\omega_{W,comm} - \omega_{W,out}) - B \frac{K_C}{K_M} \int \omega_{W,out} dt = V_M \quad (2.81)$$

From eq.2.81, the proportional plus integral controller gains  $K_{p,rw}$  and  $K_{i,rw}$  can be deduced as:

$$\begin{aligned} K_{p,rw} &= J_W \frac{K_C}{K_M} \\ K_{i,rw} &= B \frac{K_C}{K_M} \end{aligned} \quad (2.82)$$

Table 2.3: Reaction wheel parameters

Parameter	Value	Unit
$R_M$	4.0	Ohm
$K_M$	0.15	N-m/A
$K_V$	0.04	V-s/rad
$B$	$0.159 \times 10^{-5}$	N-m-s/rad
$t_s$	0.05	s
$K_C$	479.920	V/A-s
$J_{W1}$	0.075000	kg-m <sup>2</sup>
$J_{W2}$	0.075750	kg-m <sup>2</sup>
$J_{W3}$	0.074250	kg-m <sup>2</sup>
$J_{W4}$	0.075375	kg-m <sup>2</sup>

**Determination of controller gain** By inspecting eq.(2.76) which is a second order system with a zero at the origin, the following expression for  $2\zeta\omega_n$  is obtained:

$$2\zeta\omega_n = \frac{K_C}{R_M} + \frac{B}{J_W} + \frac{K_V K_M}{J_W R_M} \quad (2.83)$$

Ogata<sup>[15]</sup> defines the relationship of the settling time  $t_s$  with the damping ratio  $\zeta$  and natural frequency  $\omega_n$  as:

$$t_s = \frac{3}{\zeta\omega_n} \quad (2.84)$$

for the 5 % settling criterion. Using eq.(2.84) and rearranging eq.(2.83), an expression for controller gain  $K_C$  is obtained:

$$K_C = R_M \left( \frac{6}{t_s} - \frac{B}{J_W} - \frac{K_M K_V}{J_W R_M} \right) \quad (2.85)$$

The reaction wheel model parameter values utilized in simulation are presented in Table 2.3.

It was assumed that the reaction wheel moment of inertias were not identical for all the wheels in the cluster. Inertias of each reaction wheel is presented in Table 2.3. However, the controller gain was calculated using the inertia of reaction wheel 1 and was used in all of the wheel models. The output of reaction wheel 1 for a step input of 0.2 Nm is plotted in Figure 2.10. Note that the output reaches the reference input in 0.05 s as predicted.

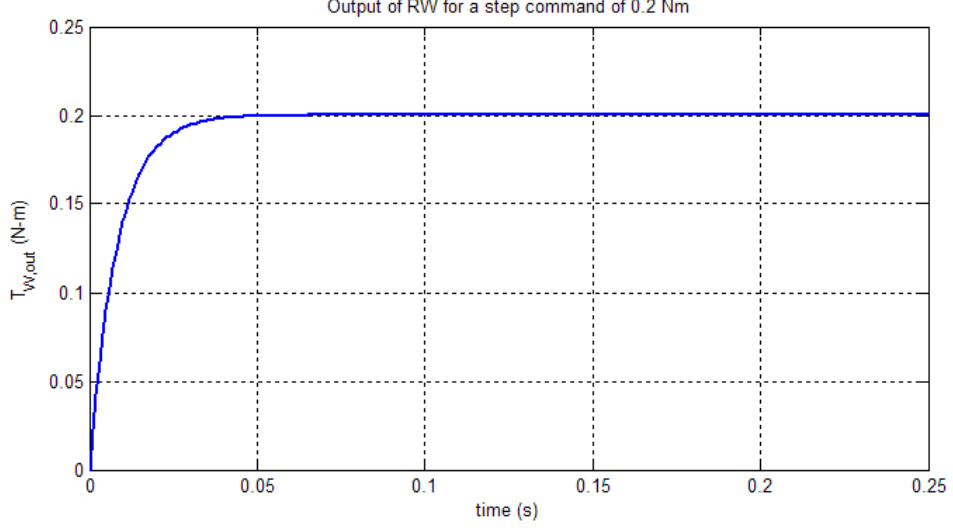


Figure 2.10: Reaction wheel output justifying the predicted settling time

One last remark must be made regarding the operating conditions of the model. The model presented in this section does not cover Coulomb and dry friction, therefore zero crossing (*i.e.* changing the direction of rotation) is not simulated in detail. It is assumed that the reaction wheels operate sufficiently away from slow rotational speeds where these effects are more significant.

### 2.3.2 Reaction Wheel Assembly (RWA)

The actuators introduced in the previous section are oriented in a tetrahedron configuration, *i.e.* each wheel is situated parallel to a face of an imaginary tetrahedron with equal sizes (Figure 2.11). The underlying logic in such an orientation is to provide actuating capability in an event of failure of one of the wheels. Theoretically, it is possible to steer the spacecraft with only three reaction wheels; however in such a design, the risk of losing three axis control capability exists if even a single reaction wheel malfunctions.

The torque generated by the RWA can be formulated as <sup>[16]</sup>:

$$\bar{T}_{RWA} = \dot{\bar{h}}_{RWA} + \tilde{\omega}_1 \bar{h}_{RWA} \quad (2.86)$$

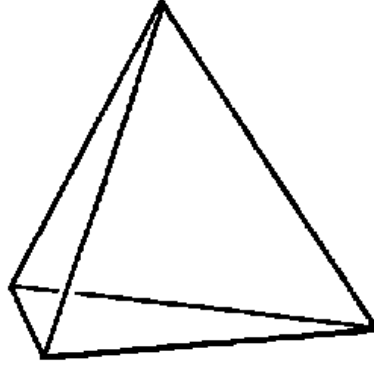


Figure 2.11: A Tetrahedron. Each wheel of the RWA is situated perpendicular to sides in such a configuration

Where,  $\bar{h}_{RWA}$  is the column matrix containing the angular momentum of each wheel. Furthermore,

$$\dot{\bar{h}}_{RWA} = \hat{E} \dot{\bar{h}}_W \quad (2.87)$$

And, similarly;

$$\bar{h}_{RWA} = \hat{E} \bar{h}_W \quad (2.88)$$

Where  $\hat{E}$  is the transformation matrix that transforms the wheel frames to the spacecraft coordinate system. It contains the unit vectors that define the orientations of each reaction wheel<sup>[17]</sup>.  $\hat{E}$  given in Ref. [17] is modified such that the maximum torque can be supplied in the pitch axis, which houses the largest inertia :

$$\hat{E} = \begin{bmatrix} \bar{e}_1 & \bar{e}_2 & \bar{e}_3 & \bar{e}_4 \end{bmatrix} = \begin{bmatrix} \sqrt{\frac{2}{3}} & -\sqrt{\frac{2}{3}} & 0 & 0 \\ -\sqrt{\frac{1}{3}} & -\sqrt{\frac{1}{3}} & \sqrt{\frac{1}{3}} & \sqrt{\frac{1}{3}} \\ 0 & 0 & -\sqrt{\frac{2}{3}} & \sqrt{\frac{2}{3}} \end{bmatrix} \quad (2.89)$$

The RWA functions as follows: firstly, torque command  $\bar{T}_C$  generated by the controller is received. RWA must produce torque such that:

$$\bar{T}_{RWA} = -\bar{T}_C = -\bar{T}_1 \quad (2.90)$$

Consequently, using equations (2.86) and (2.90), the angular momentum change that must be generated by the RWA is obtained:

$$\dot{h}_{RWA} = -\bar{T}_C + \tilde{\omega}_1 \bar{h}_{RWA} \quad (2.91)$$

Then calculated angular momentum change is assigned to each reaction wheel via the identity:

$$\dot{h}_W = \hat{E}^{-1} \dot{h}_{RWA} \quad (2.92)$$

Where  $\hat{E}^{-1}$  is the steering law<sup>[14]</sup>. However, note that the  $\hat{E}$  is not a square matrix, therefore its inverse does not exist in ordinary fashion. Therefore, its Moore-Penrose pseudo inverse is calculated from:

$$\hat{E}^{-1} = \hat{E}^T (\hat{E} \hat{E}^T)^{-1} \quad (2.93)$$

## 2.4 Sensors

Three different sensors are assumed to be operating in the satellite. Gyroscope provides feedback regarding the spacecraft angular rates, star tracker supplies attitude quaternions and proximity sensors informs the controller regarding the joint angles.

### 2.4.1 Gyroscope

The gyroscope is the device used for sensing angular rates. Its mathematical model can be formulated as<sup>[14]</sup>:

$$\bar{\omega}_{1, meas} = \hat{S} \hat{U} \bar{\omega}_1 + \bar{\beta} + \bar{\eta} \quad (2.94)$$

Where  $\bar{\omega}$  is the body rate vector,  $\bar{\beta}$  is the drift rate,  $\bar{\eta}$  is the white noise,  $\hat{U}$  is the alignment matrix (which is assumed to be equal to the identity matrix i.e. gyroscope axes are positioned in body axes) and  $\hat{S}$  is the scale factor error matrix:

$$\hat{S} = \begin{bmatrix} 1 + s_1 & 0 & 0 \\ 0 & 1 + s_2 & 0 \\ 0 & 0 & 1 + s_3 \end{bmatrix} \quad (2.95)$$

where scale factor  $s_1$ ,  $s_2$  and  $s_3$  are assumed to equal  $1 \times 10^{-3}$ . The gyroscope is assumed to be limited to measuring the angular velocities up to  $20^\circ/s$  with a resolution of  $0.001^\circ/s$ . Its measurements are assumed to be updated with a frequency of  $20\text{ Hz}$ . The bias drift was assumed to be  $0^\circ/s$ ; i.e. bias error is not taken into account since the duration of simulation is rather short (in the order of minutes). Additionally, bias error itself is also assumed to be  $0^\circ/s$ . Furthermore, white noise with amplitude varying between  $\pm 0.005^\circ/s$  is also included in the model.

Figure 2.12 presents the measured angular velocity data calculated using eq.(2.94) in comparison with the actual data.

## 2.4.2 Star Tracker

Star tracker provides the attitude information to the controller in quaternion representation. Star tracker, which is essentially a camera (see Figure 2.13), functions by taking images of the stars and comparing them with the onboard star map in order to determine the attitude with respect to the inertial frame (i.e. distant stars).

A star tracker's performance is dependent on the spacecraft angular rates, since rotational motion can degrade the image acquisition process by the smearing of images. A representative star tracker is assumed to function as presented in Table 2.4 under various angular velocities.

After a certain angular velocity ( $2^\circ/s$ ), star tracker performance is degraded and when a certain limit is violated the equipment becomes non-operational ( $6^\circ/s$ ). An update frequency of  $10\text{ Hz}$  was assumed in the model.

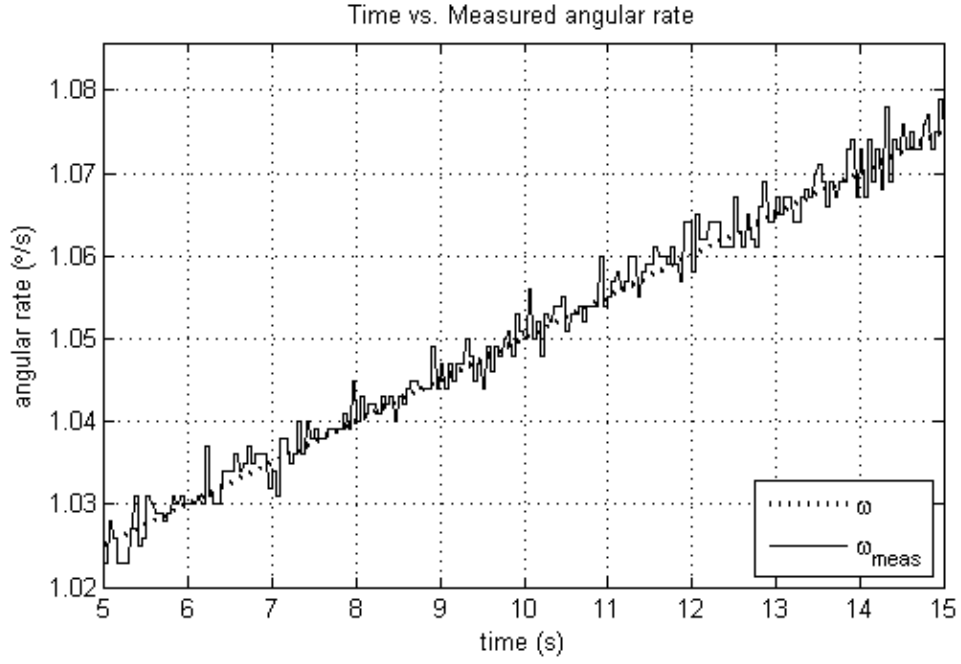


Figure 2.12: Comparison of actual and measured angular rate

Table 2.4: Star tracker performance under different angular velocities

Case	Random Error
$\ \vec{\omega}\  < 2.0^\circ/s$	5 arcsec
$2.0^\circ/s \leq \ \vec{\omega}\  < 6.0^\circ/s$	26 arcsec
$\ \vec{\omega}\  \geq 6.0^\circ/s$	N/A (Not Operational)

### 2.4.3 Proximity Sensor

Proximity sensors are used to obtain feedback regarding joint angles  $\theta_m$ . One suitable sensor for this particular application is HRSPS<sup>4</sup> developed by Vibro-Meter SA of Switzerland. HRSPS is a sensor developed under contract from ESA<sup>5</sup>/ESTEC<sup>6</sup> in order to provide a general purpose displacement system for various mechanisms<sup>[18]</sup>. A representative view of TQ 461 model sensor is given in Figure 2.14 whereas an assortment of its properties is presented in Table 2.5. Thanks to its high frequency update rate and fine resolution in nanometers, It is assumed that HRSPS provides immediate and exact feedback of joint angular position.

<sup>4</sup> High Resolution Standard Proximity Sensor

<sup>5</sup> European Space Agency

<sup>6</sup> European Space Research and Technology Center





Figure 2.13: A star tracker (SELEX Galileo of Finmeccanica)

Table 2.5: TQ 461 proximity sensor properties

Property	Value
Measuring range	$\pm 1.0 \text{ mm}$
Output voltage	$\pm 5 \text{ V}$
Effective resolution	$1.0 \text{ nm}$
Measurement rate	$1000 \text{ Hz}$
Mass	$30 \text{ gr}$
Diameter	$5 \text{ mm}$
Length	$20 \text{ mm}$
Power consumption	$2 \text{ W}$
Power dissipation	$15 \text{ mW}$



Figure 2.14: Model TQ 461 proximity sensor

## CHAPTER 3

### DISTURBANCE MODELS

Disturbances acting on the spacecraft can be categorized according to their sources. External disturbances stem from the environment the spacecraft is immersed in whereas internal disturbances are produced by the equipment within the spacecraft.

#### 3.1 External Disturbances

As mentioned earlier, external disturbances stem from the interaction between the spacecraft and its environment. The sources of these disturbances can be named as aerodynamic drag, gravity gradient torque, solar radiation pressure and magnetic residual moment. Brief information on each of these sources is presented below.

##### 3.1.1 Aerodynamic Drag

Even though the upper atmosphere is rarefied, aerodynamic drag still exists. Assuming that all the collisions with the atmospheric particles are elastic, one can formulate the force exerted on a satellite surface with area  $A_{surf,i}$  as<sup>[14]</sup>:

$$\vec{F}_{surf,i} = -\frac{1}{2}\rho C_D A_{surf,i} (\vec{n}_{surf,i} \cdot \vec{V}_\infty) \cdot \vec{V}_\infty \quad (3.1)$$

Where  $\rho$  is the atmospheric density,  $C_D$  is the drag coefficient,  $\vec{n}_{surf,i}$  is the unit vector normal to the area and  $\vec{V}_\infty$  is the translational velocity of the satellite in the medium. The total aerodynamic drag acting on the spacecraft can be obtained by writing the eq.(3.1) for all the

surfaces of the spacecraft and summing:

$$\vec{F}_{aero} = \sum_i \vec{F}_{surf,i} \quad (3.2)$$

Similarly, the total aerodynamic torque acting on the spacecraft can be obtained as:

$$\vec{T}_{aero} = \sum_i \vec{r}_{surf,i} \times \vec{F}_{surf,i} \quad (3.3)$$

In which,  $\vec{r}_{surf,i}$  is the position vector for the  $i^{\text{th}}$  surface's COP<sup>1</sup> with respect to the spacecraft COM . However, one must also check whether the  $i^{\text{th}}$  surface is subjected to flow before utilizing eq.(3.1). This can be done by calculating:

$$\theta_{surf,i} = \cos^{-1} \left( \frac{\vec{n}_{surf,i} \cdot \vec{V}_{\infty}}{|\vec{n}_{surf,i}| |\vec{V}_{\infty}|} \right) \quad (3.4)$$

And checking whether flow is impinging on the surface (*i.e.*  $90 < \theta_{surf,i} \leq 180$ ). If not, there will not be any collision with the atmospheric particles, thus:

$$\vec{F}_{surf,i} = \vec{0} \quad (3.5)$$

### 3.1.2 Gravity Gradient Torque

Gravity gradient torque stems from the fact that gravitational force exerted by the main body on the satellite is not uniformly distributed as shown in Figure 3.1.

Under these circumstances, the body tries to align itself with the gravitational potential. The gravity gradient torque  $\vec{T}_{gg}$  is then can be formulated as<sup>[14]</sup>:

$$\vec{T}_{gg} = 3(\omega_0)^2 \vec{r}_u \times (\check{J} \cdot \vec{r}_u) \quad (3.6)$$

Where  $\check{J}$  is the inertia dyadic and  $\vec{r}_u$  is the unit vector defined as:

---

<sup>1</sup> Center of Pressure

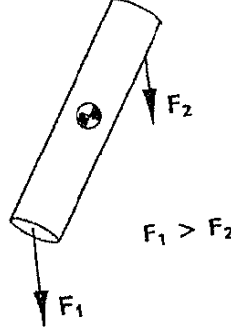


Figure 3.1: Non-uniform gravitational force leads to gravity gradient torque<sup>[19]</sup>

$$\vec{r}_u = -\frac{\vec{R}_{pos}}{|\vec{R}_{pos}|} \quad (3.7)$$

Here  $\vec{R}_{pos}$  is the vector defining the position of the spacecraft in ECI<sup>2</sup> coordinates. Moreover, the orbital rate  $\omega_0$  may be found from<sup>[14]</sup>:

$$\omega_0 = \sqrt{\frac{\mu_E}{|\vec{R}_{pos}|^3}} \quad (3.8)$$

Where  $\mu_E$  is the gravitational constant.

### 3.1.3 Solar Radiation Pressure

Solar radiation pressure is the aggregate of the force exerted by photons colliding with the spacecraft surface. It depends on the area illuminated by the source, surface characteristics and the intensity of the source. The surface characteristics determine whether the photon is absorbed or reflected. Reflection can be specular (photon is deflected at a certain angle) or as diffusion (photon is deflected from the surface randomly)<sup>[19]</sup>. Source of the radiation may as well be due to solar radiation reflected from Earth's surface (*i.e.* Earth's albedo) as well as the sun itself; although the later is more prevalent<sup>[14]</sup>. Depending on whether the photon is absorbed or reflected, the mathematical model takes the form:

---

<sup>2</sup> Earth Centered Inertial

$$d\vec{f}_{sol} = -P_{sol} \int \left[ (1 - c_s) \vec{s}_{sol} + 2 \left( c_s \cos \theta_{sol} + \frac{1}{3} c_d \right) \vec{n}_{sol} \right] \cos \theta_{sol} dA_{sol} \quad (3.9)$$

where  $P_{sol}$  is the momentum flux,  $\vec{s}_{sol}$  is the unit vector from the spacecraft to sun and  $\vec{n}_{sol}$  is the normal vector of the unit area  $dA_{sol}$ .  $c_s$  and  $c_d$  are the coefficients of specular and diffusive reflections respectively<sup>[14]</sup>. Using eq.(3.9), the total solar radiation disturbance torque can be obtained by:

$$\vec{T}_{sol} = \int \vec{r}_{sol} \times d\vec{f}_{sol} \quad (3.10)$$

### 3.1.4 Magnetic Residual Moment

Most spacecraft are not electrically inert; electrical currents flow within circuits in the spacecraft for power distribution, communication etc.; creating a dipole moment. In the presence of a magnetic field, the interaction among the dipole moment and magnetic field yields torque<sup>[14]</sup>:

$$\vec{T}_{mag} = \vec{m}_{res} \times \vec{B}_{mag} \quad (3.11)$$

where  $m_{res}$  is the magnetic dipole moment and  $\vec{B}_{mag}$  the local magnetic field vector. This phenomenon can also be exploited by using actuators that generate "intentional" dipole moments to interact with the Earth's magnetic field (Figure 3.2) and produce control torques. This is the main working principal of magnetic torque rods.

As it can be inferred from equations (3.1), (3.7), (3.9) and (3.11), parameters such as spacecraft position and velocity, sun normal vector, local magnetic field vector are all have to be obtained in order to utilize the above mathematical models. These parameters can only be obtained by an orbit propagator. Moreover, as mentioned earlier, external disturbances have relatively low amplitudes and frequencies. Therefore; more emphasis is given to the internal disturbances which have higher frequencies and amplitudes that are likely to effect pointing performance (note that the imaging duration is much less than the orbit duration itself). Thus, the arduous labor of creating an orbit propagator and detailed modeling was not undertaken

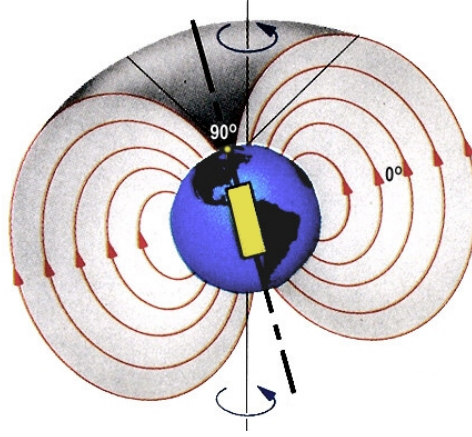


Figure 3.2: A depiction of Earth's magnetic field<sup>[20]</sup>

Table 3.1: Parameters of the sun-synchronous orbit<sup>[21]</sup>

Parameter	Value	Unit
$a(\text{semi} - \text{majoraxis})$	7028	Km
$e(\text{eccentricity})$	0	NA
$i(\text{inclination})$	97.8	°

as much as the external disturbances are considered. Instead, the results obtained in the work of Kutlu<sup>[21]</sup> was observed and sinusoidal functions that approximate the total external disturbances torque were obtained for a satellite with orbital parameters given in Table 3.1. The output of the approximating functions are given in Figure 3.3.

## 3.2 Internal Disturbances

As mentioned earlier, internal disturbance torques are generated by the equipment operating on the spacecraft. Their amplitudes and frequencies are much higher than that of the external disturbances; therefore they pose a much critical threat to spacecraft pointing performance. They could be named as propellant sloshing, reaction wheel induced vibration and slew induced vibration.

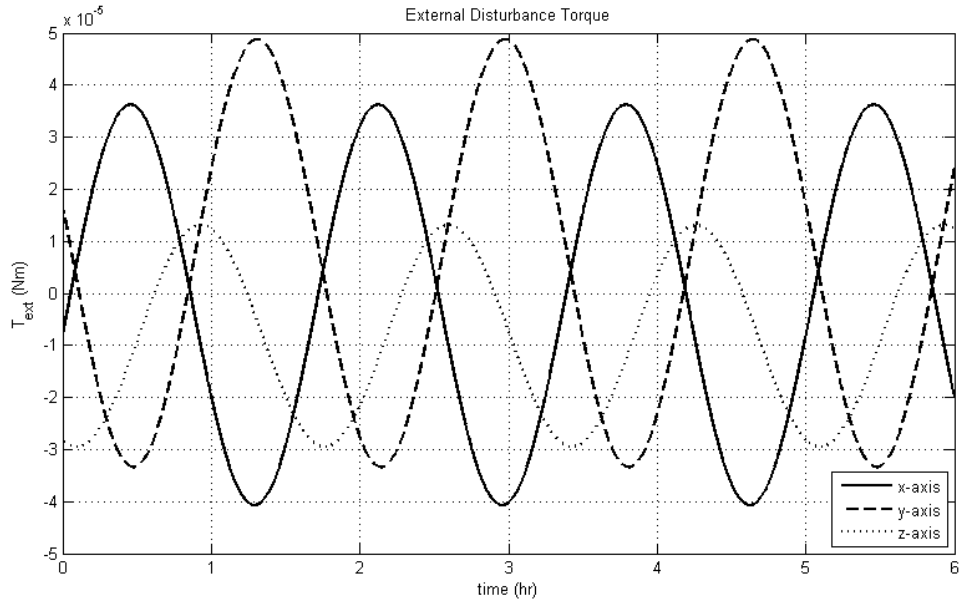


Figure 3.3: Plot of external disturbance torque for 6 hours

### 3.2.1 Propellant Sloshing

Spacecraft occasionally carry a substantial amount of fuel in order to carry out various maneuvers such as orbital station keeping. Attitude maneuvers may induce sloshing of this fuel which could lead to the destabilization of the spacecraft. Thus, it is a common practice to model the onboard propellant in order to fully appreciate its effects on attitude stability. Modeling liquid dynamics coupled with spacecraft would be an demanding task, but fortunately Wertz<sup>[14]</sup> suggests that equivalent mechanical systems can be utilized. One such equivalent system is a simple pendulum (Figure 3.4).

Wie<sup>[9]</sup> further includes the derivation of equations of motion for one such case, which is presented below as adjusted for our use. The disturbance torque due to propellant sloshing in a single axis rotation maneuver can be described by:

$$T_{slosh} = -mb \left[ b\dot{\omega} + l(\dot{\omega} + \ddot{\alpha}) \cos(\alpha) - l(\omega + \dot{\alpha})^2 \sin(\alpha) \right] \quad (3.12)$$

Where  $m$  is the representative mass for the pendulum,  $b$  is the offset of the pendulum rotation axis from the main body rotation axis,  $l$  is the length of the simple pendulum whereas  $\omega$  is the

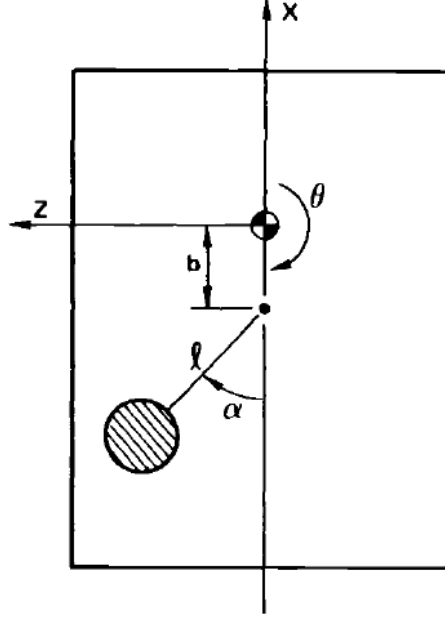


Figure 3.4: Fuel tank sloshing dynamics represented by a simple pendulum in a body rotating around pitch axis (adapted from Ref.[14])

angular rate of the body at the axis of interest. Furthermore,  $\alpha$  is the angle of pendulum with the normal whose acceleration expression is<sup>[9]</sup>:

$$\ddot{\alpha} = -\frac{b}{l}\dot{\omega} \cos(\alpha) - \dot{\omega} - \frac{b}{l}\omega^2 \sin(\alpha) - \frac{c}{m}\dot{\alpha} \quad (3.13)$$

where  $c$  is the associated damping coefficient. Using eq.(3.12), disturbance torque for each body axis is calculated and included in the model. In other words, it is assumed that at each axis resides a simple pendulum, whose properties are given in Table 3.2, representing the disturbance torque generated by the sloshing fluid.

The disturbance torques generated by the sloshing tanks during a 60 ° roll, 60 ° pitch and 0 ° yaw maneuver are given in Figure 3.5.

Note that the fuel sloshing in the yaw axis was not taken into account (*i.e.* swirling of the fuel is not covered and the tank is assumed to be positioned without any offset with respect to the yaw axis). The disturbance torque reaches approximately as much as 0.03 Nm in the pitch axis, nearly three orders of magnitude greater than the sum of external disturbances. Also, the



Table 3.2: Properties of pendulums representing sloshing fuel

Parameter	Value	Unit
Roll axis pendulum		
$m_x$	20	kg
$b_x$	0.4	m
$l_x$	0.3	m
$c_x$	0.001	Nm-s
Pitch axis pendulum		
$m_y$	20	kg
$b_y$	0.4	m
$l_y$	0.3	m
$c_y$	0.001	Nm-s
Yaw axis pendulum		
$m_z$	20	kg
$b_z$	0	m
$l_z$	0	m
$c_z$	0.001	Nm-s

high frequency motion in the sloshing dynamics worth noting.

### 3.2.2 Reaction Wheel Induced Vibration

Taniwaki<sup>[22]</sup>, via experimentation, concludes that the imbalances in a reaction wheels are significant sources of disturbances. Masterson<sup>[23]</sup> further incorporates these imbalances in a reaction wheel analytical model in order to compensate for the deficiencies in a previously developed empirical reaction wheel model. Consequently, this analytical model was later compared and validated with the experimental results obtained from Ithaco E type wheel. Thus, it is inevitable to model the imbalances if the aim is obtaining an accurate reaction wheel disturbance model.

Imbalances in a rotating wheel can be categorized into static and dynamic imbalances. Static imbalance is caused by radial asymmetries in mass distribution of a rotating body; whereas dynamic imbalance is caused by the misalignment of the principal axis of the rotating body and its spin axis. These imbalances can be represented by masses strategically placed on an ideal wheel (Figure 3.6).

Static imbalance leads to a force vector existing in the plane perpendicular to the axis of symmetry which has a constant magnitude but varying direction. Dynamic imbalance results in

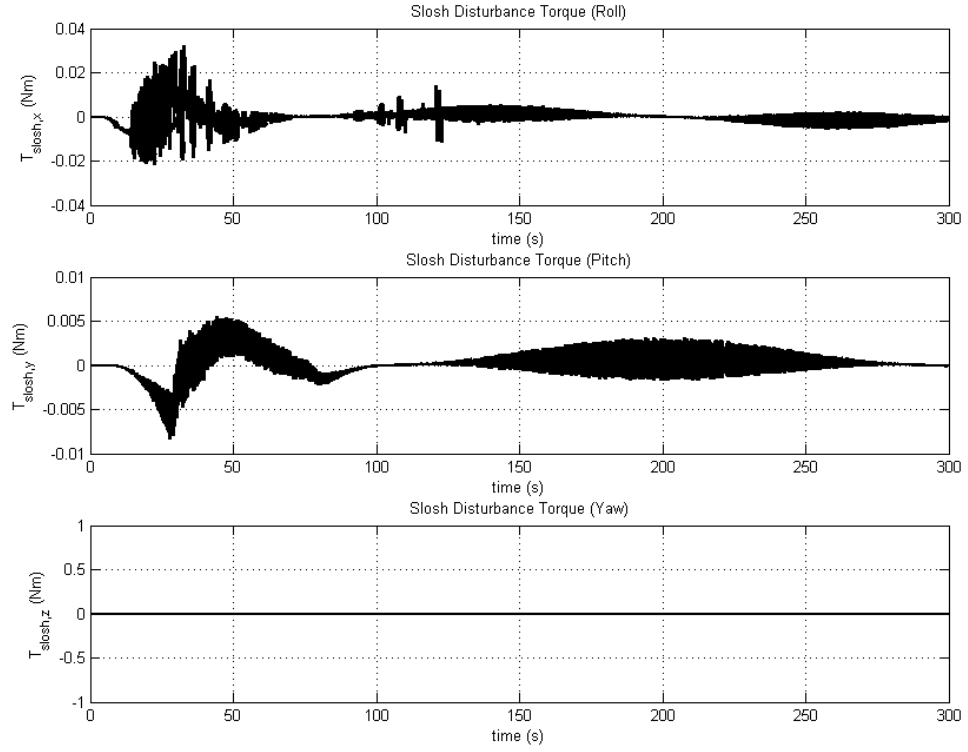


Figure 3.5: Slosh disturbance torques in roll, pitch and yaw axes

a torque vector in the same plane that tries to counteract the misalignment mentioned previously. Its magnitude is also constant whereas its direction is continuously changing. In order to represent these forces and torques, let's define the unit vectors of a local frame for wheel  $i$  as  $\vec{n}_1^{wi}$ ,  $\vec{n}_2^{wi}$  and  $\vec{n}_3^{wi}$ . Assume that this frame is attached to the spacecraft body and the reaction wheel rotates around  $\vec{n}_3^{wi}$ . Under these circumstances, the force due to static imbalance acting on the reaction wheel is<sup>[23]</sup>:

$$\vec{F}_{wi} = \left(-m_s r_s \omega_{wi}^2 \sin(\omega_{wi} t)\right) \vec{n}_1^{wi} + \left(m_s r_s \omega_{wi}^2 \cos(\omega_{wi} t)\right) \vec{n}_2^{wi} \quad (3.14)$$

where  $\omega_{wi}$  is the rotational velocity of the  $i$ th reaction hwheel,  $m_s$  is the representative static imbalance mass and  $r_s$  is its distance from the rotation axis. Similarly, the torque acting on the wheel due to dynamic imbalance is<sup>[23]</sup>:

$$\vec{T}_{wi} = \left(2m_d r_d h \omega_{wi}^2 \cos(\omega_{wi} t)\right) \vec{n}_1^{wi} + \left(2m_d r_d h \omega_{wi}^2 \sin(\omega_{wi} t)\right) \vec{n}_2^{wi} \quad (3.15)$$

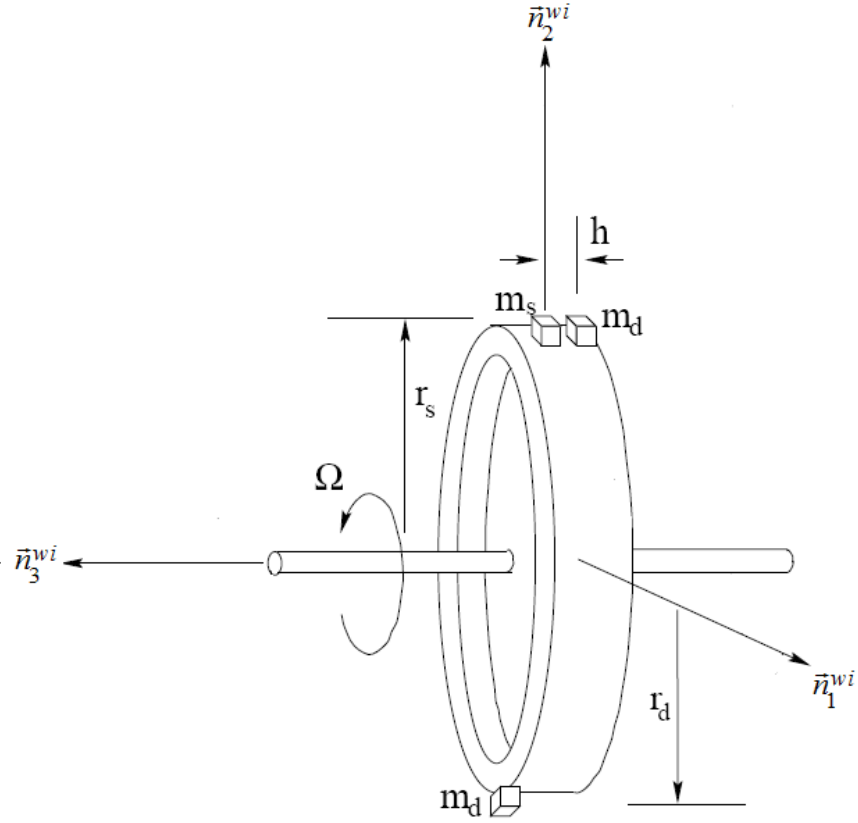


Figure 3.6: Reaction wheel together with representative masses for static ( $m_s$ ) and dynamic ( $m_d$ ) imbalances (adapted from Ref.[23])

where  $m_d$  are the representative dynamic imbalance masses and  $r_d$  is their distance from the rotation axis. Assuming that the reaction wheel is rigidly attached to the spacecraft body, the equal and opposite disturbance forces and torques will be applied on the spacecraft body. Thus, the disturbance forces being applied by the whole reaction wheel assembly on the spacecraft can be given as:

$$\vec{F}_{rwa,dist} = - \sum_{i=1}^4 \vec{F}_{wi} \quad (3.16)$$

whereas the disturbance torques can be obtained as:

$$\vec{T}_{rwa,dist} = - \sum_{i=1}^4 \vec{T}_{wi} + \vec{r}_{wi} \times \vec{F}_{wi} \quad (3.17)$$

where  $\vec{r}_{wi}$  is position vector for the  $i$ th reaction wheel. Eq.(3.16) can be written in matrix

notation as:

$$\bar{F}_{rwa,dist} = - \sum_{i=1}^4 \hat{C}_{1wi} \bar{F}_{wi} \quad (3.18)$$

where  $\hat{C}_{1wi}$  is the transformation matrix from the  $i$ th wheel's frame to the coordinate frame of the main body. Similarly for eq.(3.17):

$$\bar{T}_{rwa,dist} = - \sum_{i=1}^4 \hat{C}_{1wi} \bar{T}_{wi} + \tilde{r}_{wi} \hat{C}_{1wi} \bar{F}_{wi} \quad (3.19)$$

By using equations (3.18) and (3.19), the disturbances generated by the reaction wheel models are included in the overall model. One note must be made regarding the assumption of rigidly attached reaction wheels; wheel supports and mounts may have inherent flexibility and damping. After all, structurally isolating disturbance sources with dampers from spacecraft main body is one of the common approaches taken to mitigate jitter<sup>[8]</sup>. Therefore, reaction wheels can also be modeled with flexible mountings<sup>[23]</sup>. If included, flexibility would reduce amplitude of the disturbances. Thus, the assumption we previously made provides us with a worst case condition.

The numerical values of the parameters used in the simulation are give in Table 3.3; whereas the reaction wheel disturbance forces and torques acting on the spacecraft for a slew maneuver scenario of 60 ° of roll, 60 ° of pitch and 0 ° of yaw are given in Figures 3.7 and 3.8, respectively. The reaction wheel is assumed to be balanced up to grade  $G$  2.5 in accordance with ISO<sup>3</sup> 1940/1 standard<sup>[24]</sup>.

As it can be observed from Figures 3.7 and 3.8, the reaction wheel imbalances are the dominating disturbance source. Disturbance torques due to reaction wheels are at least an order of magnitude larger than the disturbance torques due to propellant sloshing.

---

<sup>3</sup> International Organization for Standardization

Table 3.3: Parameters for reaction wheel disturbance model

Parameter	Value	Unit
$\mu_s (= m_s r_s)$	$7.2 \times 10^{-6}$	kg-m
$\mu_d (= 2m_d r_d h)$	$1.84 \times 10^{-6}$	kg-m <sup>2</sup>
Reaction Wheel 1		
$\bar{r}_{w1}$	$\begin{bmatrix} -0.3 & 0.3 & -0.2 \end{bmatrix}^T$	m
$\hat{C}_{1w1}$	$\begin{bmatrix} 0.2000 & 0.2828 & 0.9381 \\ 0.5416 & 0.7659 & -0.3464 \\ 0.8165 & -0.5774 & 0.0000 \end{bmatrix}$	N/A
Reaction Wheel 2		
$\bar{r}_{w2}$	$\begin{bmatrix} 0.3 & 0.3 & -0.2 \end{bmatrix}^T$	m
$\hat{C}_{1w2}$	$\begin{bmatrix} 0.2000 & -0.2828 & 0.9381 \\ -0.5416 & 0.7659 & 0.3464 \\ -0.8165 & -0.5774 & 0.0000 \end{bmatrix}$	N/A
Reaction Wheel 3		
$\bar{r}_{w3}$	$\begin{bmatrix} 0.3 & -0.3 & -0.2 \end{bmatrix}^T$	m
$\hat{C}_{1w3}$	$\begin{bmatrix} 0.2000 & 0.8000 & 0.5657 \\ -0.9798 & 0.1633 & 0.1155 \\ 0.0000 & 0.5774 & -0.8165 \end{bmatrix}$	N/A
Reaction Wheel 4		
$\bar{r}_{w4}$	$\begin{bmatrix} -0.3 & -0.3 & -0.2 \end{bmatrix}^T$	m
$\hat{C}_{1w4}$	$\begin{bmatrix} 0.2000 & -0.8000 & 0.5657 \\ 0.9798 & 0.1633 & -0.1155 \\ 0.0000 & 0.5774 & 0.8165 \end{bmatrix}$	N/A

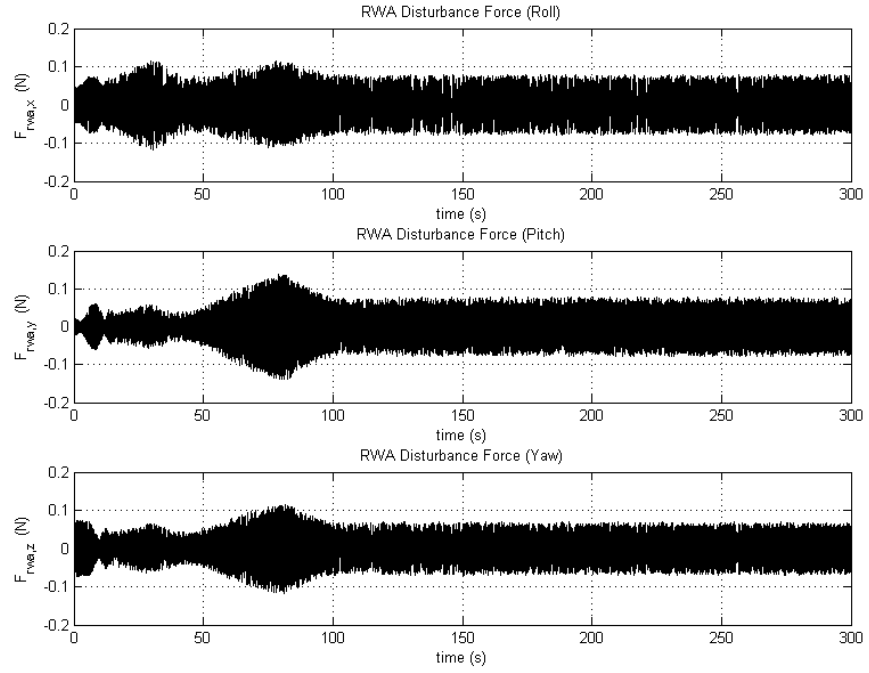


Figure 3.7: Disturbance forces acting on the satellite main body due to reaction wheel imbalances

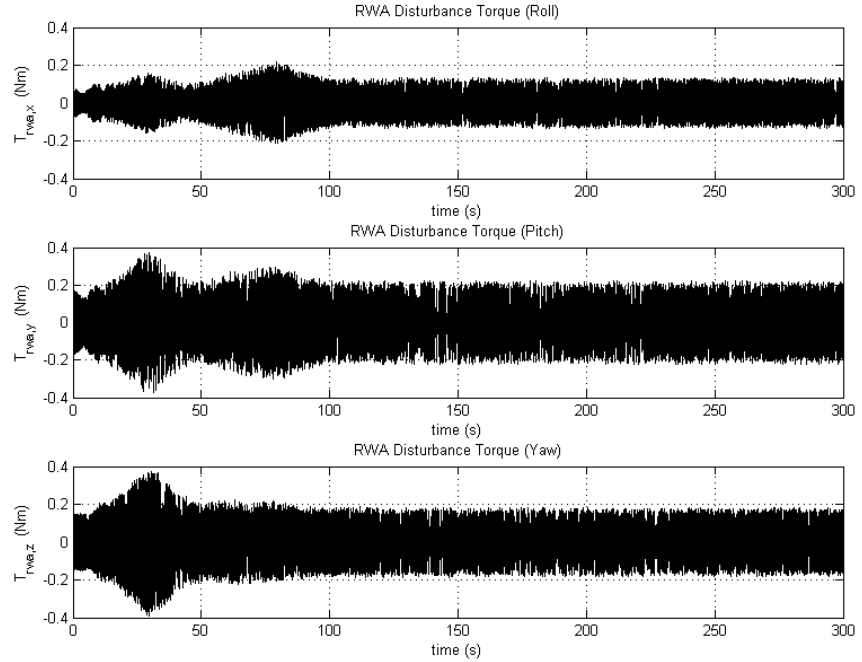


Figure 3.8: Disturbance torques acting on the satellite main body due to reaction wheel imbalances

### **3.2.3 Slew Induced Vibration**

Slew maneuver itself does not pose any danger to the pointing accuracy. However, large angle slew maneuvers induce other disturbance sources such as the propellant sloshing disturbance just covered within this section. Since these are agile reorientation maneuvers, they subject the spacecraft to rapid acceleration followed by rapid deceleration. Such maneuvers excite the fuel in the tank thus it begins sloshing. Similarly, they may also cause the appendages to vibrate. For the dynamics of all these disturbance sources are already covered (tank sloshing in Chapter 3 and solar panels in Chapter 2 as part of the multi-body model), no additional mathematical models have to be defined under this topic, yet the main source of some major disturbances had to be identified.

## CHAPTER 4

### CONTROL ALGORITHMS

Two different control algorithms were studied to realize the satellite reorientation maneuver. The first is the Quaternion Feedback Controller that uses a scheme similar to the proportional and derivative (PD) control law. The other proposed controller is the State Feedback Controller scheme that utilizes LQR<sup>1</sup> approach to determine state feedback gains.

#### 4.1 Quaternion Feedback (QFB) Controller

One method to realize the slew maneuver is the QFB controller. This controller utilizes the quaternion error and body angular rate feedback to determine the required control torque<sup>[9]</sup>. Thus, it can be categorized as a PD controller. Wie<sup>[25]</sup> also asserts through Liapunov's direct method that the QFB control law is asymptotically stable in the large. The required control torque can be obtained by:

$$\bar{T}_C = -\hat{K}_P \bar{q}_E - \hat{K}_D \bar{\omega} \quad (4.1)$$

where  $\hat{K}$  proportional control gain matrix defined as:

$$\hat{K}_P = K_p \hat{J}_{Tot} \quad (4.2)$$

with  $K_p$  as the scalar gain. Similarly,  $\hat{K}_D$  derivative control gain matrix defined as:

---

<sup>1</sup> Linear Quadratic Regulator



$$\hat{K}_D = K_d \hat{J}_{Tot} \quad (4.3)$$

with  $K_d$  as the scalar gain.  $\hat{J}_{Tot}$  is the total moment of inertia of the satellite including the yokes and solar panels. It is calculated once by assuming no deflection at the joints ( $\theta_m = 0^\circ$ ) and utilizing parallel axis theorem. The small deflection assumption was later found to be valid as proved by the results given in Figures 6.16 and 6.17 in Chapter 6. Quaternion error  $q_E$  is obtained from the relationship<sup>[9]</sup>:

$$\bar{q}_E = \begin{bmatrix} q_{R,4} & q_{R,3} & -q_{R,2} & -q_{R,1} \\ -q_{R,3} & q_{R,4} & q_{R,1} & -q_{R,2} \\ q_{R,2} & -q_{R,1} & q_{R,4} & -q_{R,3} \\ q_{R,1} & q_{R,2} & q_{R,3} & q_{R,4} \end{bmatrix} \bar{q} \quad (4.4)$$

Here  $\bar{q}$  is the quaternion representing the current attitude of the spacecraft main body. It is provided by the star tracker. Also,  $q_{R,1}$ ,  $q_{R,2}$ ,  $q_{R,3}$  and  $q_{R,4}$  are the elements of the reference quaternion  $\bar{q}_R$ , which is obtained from the reference Euler angles (see the Appendix of Ref.[13] for transformation between quaternions and Euler angles).

## 4.2 State Feedback (SFB) Controller

Another controller that enables the slewing of the spacecraft is the state feedback controller. This controller utilizes minimum amount of states that completely define the plant configuration in order to calculate the required control torque  $\bar{T}_C$ . The state feedback control law may be given as<sup>[26]</sup>:

$$\bar{u} = -\hat{K}\bar{x} \quad (4.5)$$

where  $\bar{u}$  is defined as:

$$\bar{u} = \bar{T}_C = \begin{bmatrix} T_{1x} & T_{1y} & T_{1z} \end{bmatrix}^T \quad (4.6)$$

$T_{1x}$ ,  $T_{1y}$  and  $T_{1z}$  are the control torques respectively in roll, pitch and yaw axes which will be demanded from the actuators.  $\bar{x}$  is defined as:

$$\bar{x} = \begin{bmatrix} \omega_{1x} & \omega_{1y} & \omega_{1z} & \theta_1 & \dot{\theta}_1 & \theta_2 & \dot{\theta}_2 & \theta_3 & \dot{\theta}_3 & \theta_4 & \dot{\theta}_4 & \theta_5 & \dot{\theta}_5 & \theta_6 & \dot{\theta}_6 & q_1 & q_2 & q_3 & \theta_1 & \theta_2 & \theta_3 & \theta_4 & \theta_5 & \theta_6 \end{bmatrix}^T \quad (4.7)$$

where  $\omega_{1x}$ ,  $\omega_{1y}$  and  $\omega_{1z}$  are the angular rates of the main body;  $\theta_m$  and  $\dot{\theta}_m$  are the angular position and velocity of joint  $m$  whereas  $q_1$ ,  $q_2$  and  $q_3$  are the first three elements of the quaternion column matrix  $\bar{q}$  defining spacecraft attitude. Due to their interdependence, it is not required to include all the elements of the quaternions ( $q_1^2 + q_2^2 + q_3^2 + q_4^2 = 1$ ), only three elements will suffice.

The rest of this section deals with the problem of determining the SFB gain matrix  $\hat{K}$ . For this, first the states obtained in Chapter 2 are reduced to the one given in eq.(4.7). Then, the system is linearized by obtaining its state and input Jacobian matrices ( $\hat{G}_x$  and  $\hat{G}_u$ ) around the equilibrium state  $\bar{x}_e$ . Finally, gain matrix  $\hat{K}$  is obtained via LQR method using  $\hat{G}_x$  and  $\hat{G}_u$ .

#### 4.2.1 State Reduction

It is evident that the number of states obtained in Chapter 2 is much more than that of the number of states given in eq.(4.7). Also, some of the states such as joint reaction forces and torques are not needed in the simulation; their existence will only bring additional computational load. Thus, from this standpoint, it is advisable to eliminate these states from the equation given in eq.(2.48). The states in this equation are already defined in eq.(2.47) and repeated here for the sake of completeness.

$$\bar{y} = \begin{bmatrix} \dot{\omega}_1^T \dots \dot{\omega}_n^T & \dot{v}_1^T \dots \dot{v}_n^T & \bar{F}_{G1}^T \dots \bar{F}_{Gm}^T & \bar{T}_{G1}^T \dots \bar{T}_{Gm}^T & \ddot{\theta}_1 \dots \ddot{\theta}_m \end{bmatrix}^T \quad (4.8)$$

In the first step of reduction from eq.(4.8) to eq.(4.7); the variables given in eq.(4.8) will be reduced to:

$$\dot{\bar{x}} = \begin{bmatrix} \dot{\omega}_1^T & \dot{v}_1^T & \ddot{\theta}_1 \dots \ddot{\theta}_m \end{bmatrix}^T \quad (4.9)$$

and the matrix  $\hat{A}$  will be updated accordingly. For this, the eq.(2.49) is rewritten as:

$$\begin{bmatrix} \hat{A}_{11a} & \hat{A}_{11b} & \hat{A}_{12ma} & \hat{A}_{12na} & \hat{A}_{13a} & \hat{A}_{14a} & \hat{A}_{15a} \\ \hat{A}_{11c} & \hat{A}_{11d} & \hat{A}_{12mb} & \hat{A}_{12nb} & \hat{A}_{13b} & \hat{A}_{14b} & \hat{A}_{15b} \\ \hat{A}_{21am} & \hat{A}_{21bm} & \hat{A}_{22m} & \hat{A}_{22n} & \hat{A}_{23m} & \hat{A}_{24m} & \hat{A}_{25m} \\ \hat{A}_{21an} & \hat{A}_{21bn} & \hat{A}_{22o} & \hat{A}_{22p} & \hat{A}_{23n} & \hat{A}_{24n} & \hat{A}_{25n} \\ \hat{A}_{31a} & \hat{A}_{31b} & \hat{A}_{32m} & \hat{A}_{32n} & \hat{A}_{33} & \hat{A}_{34} & \hat{A}_{35} \\ \hat{A}_{41a} & \hat{A}_{41b} & \hat{A}_{42m} & \hat{A}_{42n} & \hat{A}_{43} & \hat{A}_{44} & \hat{A}_{45} \\ \hat{A}_{51a} & \hat{A}_{51b} & \hat{A}_{52m} & \hat{A}_{52n} & \hat{A}_{53} & \hat{A}_{54} & \hat{A}_{55} \end{bmatrix} \begin{bmatrix} \bar{y}_{11a} \\ \bar{y}_{11b} \\ \bar{y}_{21m} \\ \bar{y}_{21n} \\ \bar{y}_{31} \\ \bar{y}_{41} \\ \bar{y}_{51} \end{bmatrix} = \begin{bmatrix} \bar{u}_{11a} \\ \bar{u}_{11b} \\ \bar{u}_{21m} \\ \bar{u}_{21n} \\ \bar{u}_{31} \\ \bar{u}_{41} \\ \bar{u}_{51} \end{bmatrix} \quad (4.10)$$

where  $\bar{y}_{11a}$  and  $\bar{y}_{11b}$  are:

$$\begin{aligned} \bar{y}_{11a} &= \dot{\omega}_1 \\ \bar{y}_{11b} &= \left[ \dot{\omega}_2^T \dots \dot{\omega}_n^T \right]^T \end{aligned} \quad (4.11)$$

similarly,  $\bar{y}_{21m}$  and  $\bar{y}_{21n}$  are:

$$\begin{aligned} \bar{y}_{21m} &= \dot{v}_1 \\ \bar{y}_{21n} &= \left[ \dot{v}_2^T \dots \dot{v}_n^T \right]^T \end{aligned} \quad (4.12)$$

As it can be observed from eq.(4.10), the matrix  $\hat{A}$  and column matrix  $\bar{u}$  are partitioned accordingly to equations (4.11 and (4.12). Variables given in eq.(4.10) can be related to the variables given in eq.(2.49) via:

$$\begin{bmatrix} \hat{A}_{11a} & \hat{A}_{11b} \\ \hat{A}_{11c} & \hat{A}_{11d} \end{bmatrix} = \hat{A}_{11} \quad (4.13)$$

and,

$$\begin{bmatrix} \hat{A}_{22m} & \hat{A}_{22n} \\ \hat{A}_{22o} & \hat{A}_{22p} \end{bmatrix} = \hat{A}_{22} \quad (4.14)$$

also,

$$\begin{bmatrix} \hat{A}_{12ma} & \hat{A}_{12na} \\ \hat{A}_{12mb} & \hat{A}_{12nb} \end{bmatrix} = \hat{A}_{12} \quad (4.15)$$

additionally,

$$\begin{bmatrix} \hat{A}_{21am} & \hat{A}_{21bm} \\ \hat{A}_{21an} & \hat{A}_{21bn} \end{bmatrix} = \hat{A}_{21} \quad (4.16)$$

also for  $i = 3, 4, 5$ ;

$$\begin{aligned} \begin{bmatrix} \hat{A}_{1ia} \\ \hat{A}_{1ib} \end{bmatrix} &= \hat{A}_{1i} \\ \begin{bmatrix} \hat{A}_{i1a} & \hat{A}_{i1b} \end{bmatrix} &= \hat{A}_{i1} \\ \begin{bmatrix} \hat{A}_{2im} \\ \hat{A}_{2in} \end{bmatrix} &= \hat{A}_{2i} \\ \begin{bmatrix} \hat{A}_{i2m} & \hat{A}_{i2n} \end{bmatrix} &= \hat{A}_{i1} \end{aligned} \quad (4.17)$$

finally,

$$\begin{bmatrix} \bar{u}_{11a} \\ \bar{u}_{11b} \end{bmatrix} = \bar{u}_{11} \quad (4.18)$$

and

$$\begin{bmatrix} \bar{u}_{21m} \\ \bar{u}_{21n} \end{bmatrix} = \bar{u}_{21} \quad (4.19)$$

Including the zero matrices, eq.(4.10) takes the form:

$$\begin{bmatrix} \hat{A}_{11a} & \hat{0} & \hat{0} & \hat{0} & \hat{A}_{13a} & \hat{A}_{14a} & \hat{0} \\ \hat{0} & \hat{A}_{11d} & \hat{0} & \hat{0} & \hat{A}_{13b} & \hat{A}_{14b} & \hat{0} \\ \hat{0} & \hat{0} & \hat{A}_{22m} & \hat{0} & \hat{A}_{23m} & \hat{0} & \hat{0} \\ \hat{0} & \hat{0} & \hat{0} & \hat{A}_{22p} & \hat{A}_{23n} & \hat{0} & \hat{0} \\ \hat{A}_{31a} & \hat{A}_{31b} & \hat{A}_{32m} & \hat{A}_{32n} & \hat{0} & \hat{0} & \hat{0} \\ \hat{A}_{41a} & \hat{A}_{41b} & \hat{0} & \hat{0} & \hat{0} & \hat{0} & \hat{A}_{45} \\ \hat{0} & \hat{0} & \hat{0} & \hat{0} & \hat{0} & \hat{A}_{54} & \hat{0} \end{bmatrix} \begin{bmatrix} \bar{y}_{11a} \\ \bar{y}_{11b} \\ \bar{y}_{21m} \\ \bar{y}_{21n} \\ \bar{y}_{31} \\ \bar{y}_{41} \\ \bar{y}_{51} \end{bmatrix} = \begin{bmatrix} \bar{u}_{11a} \\ \bar{u}_{11b} \\ \bar{u}_{21m} \\ \bar{u}_{21n} \\ \bar{u}_{31} \\ \bar{u}_{41} \\ \bar{u}_{51} \end{bmatrix} \quad (4.20)$$

Performing row operations so that  $\bar{y}_{11a}$ ,  $\bar{y}_{21m}$  and  $\bar{y}_{51}$  are grouped together:

$$\begin{bmatrix} \hat{A}_{11a} & \hat{0} & \hat{0} & \hat{0} & \hat{0} & \hat{A}_{13a} & \hat{A}_{14a} \\ \hat{0} & \hat{A}_{22m} & \hat{0} & \hat{0} & \hat{0} & \hat{A}_{23m} & \hat{0} \\ \hat{0} & \hat{0} & \hat{0} & \hat{0} & \hat{0} & \hat{0} & \hat{A}_{54} \\ \hat{0} & \hat{0} & \hat{0} & \hat{A}_{11d} & \hat{0} & \hat{A}_{13b} & \hat{A}_{14b} \\ \hat{0} & \hat{0} & \hat{0} & \hat{0} & \hat{A}_{22p} & \hat{A}_{23n} & \hat{0} \\ \hat{A}_{31a} & \hat{A}_{32m} & \hat{0} & \hat{A}_{31b} & \hat{A}_{32n} & \hat{0} & \hat{0} \\ \hat{A}_{41a} & \hat{0} & \hat{A}_{45} & \hat{A}_{41b} & \hat{0} & \hat{0} & \hat{0} \end{bmatrix} \begin{bmatrix} \bar{y}_{11a} \\ \bar{y}_{21m} \\ \bar{y}_{51} \\ \bar{y}_{11b} \\ \bar{y}_{21n} \\ \bar{y}_{31} \\ \bar{y}_{41} \end{bmatrix} = \begin{bmatrix} \bar{u}_{11a} \\ \bar{u}_{21m} \\ \bar{u}_{51} \\ \bar{u}_{11b} \\ \bar{u}_{21n} \\ \bar{u}_{31} \\ \bar{u}_{41} \end{bmatrix} \quad (4.21)$$

Defining  $\bar{y}_n$  and  $\bar{u}_n$  as:

$$\bar{y}_n = \begin{bmatrix} \bar{y}_{11a}^T & \bar{y}_{21m}^T & \bar{y}_{51}^T \end{bmatrix}^T \quad (4.22)$$

and

$$\bar{u}_n = \begin{bmatrix} \bar{u}_{11a} & \bar{u}_{21m} & \bar{u}_{51} \end{bmatrix}^T \quad (4.23)$$

Eq.(4.21) takes the following form:

$$\begin{bmatrix} \hat{A}_{nn} & \hat{0} & \hat{0} & \hat{A}_{n3} & \hat{A}_{n4} \\ \hat{0} & \hat{A}_{11d} & \hat{0} & \hat{A}_{13b} & \hat{A}_{14b} \\ \hat{0} & \hat{0} & \hat{A}_{22p} & \hat{A}_{23n} & \hat{0} \\ \hat{A}_{3n} & \hat{A}_{31b} & \hat{A}_{32n} & \hat{0} & \hat{0} \\ \hat{A}_{4n} & \hat{A}_{41b} & \hat{0} & \hat{0} & \hat{0} \end{bmatrix} \begin{bmatrix} \bar{y}_n \\ \bar{y}_{11b} \\ \bar{y}_{21n} \\ \bar{y}_{31} \\ \bar{y}_{41} \end{bmatrix} = \begin{bmatrix} \bar{u}_n \\ \bar{u}_{11b} \\ \bar{u}_{21n} \\ \bar{u}_{31} \\ \bar{u}_{41} \end{bmatrix} \quad (4.24)$$

where  $\hat{A}_{nn}$  is:

$$\hat{A}_{nn} = \begin{bmatrix} \hat{A}_{11a} & \hat{0} & \hat{0} \\ \hat{0} & \hat{A}_{22m} & \hat{0} \\ \hat{0} & \hat{0} & \hat{0} \end{bmatrix} \quad (4.25)$$

also  $\hat{A}_{n3}$  becomes:

$$\hat{A}_{n3} = \begin{bmatrix} \hat{A}_{13a} & \hat{A}_{23m} & \hat{0} \end{bmatrix}^T \quad (4.26)$$

additionally,  $\hat{A}_{n4}$  is:

$$\hat{A}_{n4} = \begin{bmatrix} \hat{A}_{14a} & \hat{0} & \hat{A}_{54} \end{bmatrix}^T \quad (4.27)$$

furthermore,  $\hat{A}_{3n}$  is:

$$\hat{A}_{3n} = \begin{bmatrix} \hat{A}_{31a} & \hat{A}_{32m} & \hat{0} \end{bmatrix} \quad (4.28)$$

finally,  $\hat{A}_{4n}$  can be defined as:

$$\hat{A}_{4n} = \begin{bmatrix} \hat{A}_{41a} & \hat{0} & \hat{A}_{45} \end{bmatrix} \quad (4.29)$$

The state reduction is done on eq.(4.24) via the method employed in Stoneking<sup>[12]</sup>. Firstly, each row except the first one is multiplied by coefficients  $\hat{\alpha}$ ,  $\hat{\beta}$ ,  $\hat{\gamma}$  and  $\hat{\epsilon}$ .

$$\begin{array}{l}
\hat{\alpha}/ \\
\hat{\beta}/ \\
\hat{\gamma}/ \\
\hat{\varepsilon}/
\end{array}
\begin{bmatrix}
\hat{A}_{nn} & \hat{0} & \hat{0} & \hat{A}_{n3} & \hat{A}_{n4} \\
\hat{0} & \hat{A}_{11d} & \hat{0} & \hat{A}_{13b} & \hat{A}_{14b} \\
\hat{0} & \hat{0} & \hat{A}_{22p} & \hat{A}_{23n} & \hat{0} \\
\hat{A}_{3n} & \hat{A}_{31b} & \hat{A}_{32n} & \hat{0} & \hat{0} \\
\hat{A}_{4n} & \hat{A}_{41b} & \hat{0} & \hat{0} & \hat{0}
\end{bmatrix}
\begin{bmatrix}
\bar{y}_n \\
\bar{y}_{11b} \\
\bar{y}_{21n} \\
\bar{y}_{31} \\
\bar{y}_{41}
\end{bmatrix}
=
\begin{bmatrix}
\bar{u}_n \\
\bar{u}_{11b} \\
\bar{u}_{21n} \\
\bar{u}_{31} \\
\bar{u}_{41}
\end{bmatrix}
\begin{array}{l}
/\hat{\alpha} \\
/\hat{\beta} \\
/\hat{\gamma} \\
/\hat{\varepsilon}
\end{array}
\quad (4.30)$$

Secondly, the summation of all the rows of eq.(4.30) is written such that:

$$\begin{bmatrix}
\hat{B}_{11} & \hat{B}_{12} & \hat{B}_{13} & \hat{B}_{14} & \hat{B}_{15}
\end{bmatrix}
\begin{bmatrix}
\bar{y}_n \\
\bar{y}_{11b} \\
\bar{y}_{21n} \\
\bar{y}_{31} \\
\bar{y}_{41}
\end{bmatrix}
= \bar{u}_n + \hat{\alpha}\bar{u}_{11b} + \hat{\beta}\bar{u}_{21n} + \hat{\gamma}\bar{u}_{31} + \hat{\varepsilon}\bar{u}_{41} \quad (4.31)$$

where the expression for the elements of  $\hat{B}$  are:

$$\begin{aligned}
\hat{B}_{11} &= \hat{A}_{nn} + \hat{\gamma}\hat{A}_{3n} + \hat{\varepsilon}\hat{A}_{4n} \\
\hat{B}_{12} &= \hat{\alpha}\hat{A}_{11d} + \hat{\gamma}\hat{A}_{31b} + \hat{\varepsilon}\hat{A}_{41b} \\
\hat{B}_{13} &= \hat{\beta}\hat{A}_{22p} + \hat{\gamma}\hat{A}_{32n} \\
\hat{B}_{14} &= \hat{A}_{n3} + \hat{\alpha}\hat{A}_{13b} + \hat{\beta}\hat{A}_{23n} \\
\hat{B}_{15} &= \hat{A}_{n4} + \hat{\alpha}\hat{A}_{14b}
\end{aligned} \quad (4.32)$$

When the all the elements of  $\hat{B}$  are set to  $\hat{0}$  except  $\hat{B}_{11}$ , a reduced expression that only includes states given in eq.(4.9) are obtained. Therefore the reduction problem is redefined as determining  $\hat{\alpha}$ ,  $\hat{\beta}$ ,  $\hat{\gamma}$  and  $\hat{\varepsilon}$  such that only  $\bar{y}_n$  is available in eq.(4.32). Setting  $\hat{B}_{12}$ ,  $\hat{B}_{13}$ ,  $\hat{B}_{14}$  and  $\hat{B}_{15}$  to  $\hat{0}$ , the coefficients matrices are obtained as:

$$\begin{aligned}
\hat{\alpha} &= -\hat{A}_{n4}\hat{A}_{14b}^{-1} \\
\hat{\beta} &= -(\hat{A}_{n3} + \hat{\alpha}\hat{A}_{13b})\hat{A}_{23n}^{-1} \\
\hat{\gamma} &= -\hat{\beta}\hat{A}_{22p}\hat{A}_{32n}^{-1} \\
\hat{\varepsilon} &= -(\hat{\alpha}\hat{A}_{11d} + \hat{\gamma}\hat{A}_{31b})\hat{A}_{41b}^{-1}
\end{aligned} \quad (4.33)$$

Upon obtaining these matrices eq.(2.48) can be rewritten in reduced form as;

$$\hat{A}^* \bar{y} = \bar{u}^* \quad (4.34)$$

where  $\hat{A}^*$  is:

$$\hat{A}^* = \hat{B}_{11} = \hat{A}_{nn} + \hat{\gamma} \hat{A}_{3n} + \hat{\varepsilon} \hat{A}_{4n} \quad (4.35)$$

and  $\bar{u}^*$  is:

$$\bar{u}^* = \bar{u}_n + \hat{\alpha} \bar{u}_{11b} + \hat{\beta} \bar{u}_{21n} + \hat{\gamma} \bar{u}_{31} + \hat{\varepsilon} \bar{u}_{41} \quad (4.36)$$

#### 4.2.2 Linearizing the System

Assume that a system is described by the relation:

$$\dot{\bar{x}} = \bar{f}(\bar{x}, \bar{u}) \quad (4.37)$$

where  $\bar{f}$  is the column matrix including non-linear functions that relate the states  $\bar{x}$  given eq.(4.7) and inputs  $\bar{u}$  given in eq.(4.6) to the time derivatives of the states  $\dot{\bar{x}}$ . Around an equilibrium point described by equilibrium states  $\bar{x}_e$  and inputs  $\bar{u}_e$ , these functions can be linearized. This linearization process is realized by obtaining the Jacobian matrix of the system. For our case, the state Jacobian matrix  $\hat{G}_x$  takes the form:

$$\hat{G}_x = \left[ \begin{array}{ccc} \frac{\partial f_1}{\partial x_1} & \cdots & \frac{\partial f_1}{\partial x_{18}} \\ \vdots & \ddots & \vdots \\ \frac{\partial f_{18}}{\partial x_1} & \cdots & \frac{\partial f_{18}}{\partial x_{18}} \end{array} \right]_{\substack{\bar{x}=\bar{x}_e \\ \bar{u}=\bar{u}_e}} \quad (4.38)$$

similarly,  $\hat{G}_u$  is obtained from the identity:



$$\hat{G}_u = \left[ \begin{array}{ccc} \frac{\partial f_1}{\partial u_1} & \dots & \frac{\partial f_1}{\partial u_3} \\ \vdots & \ddots & \vdots \\ \frac{\partial f_{18}}{\partial u_1} & \dots & \frac{\partial f_{18}}{\partial u_3} \end{array} \right]_{\substack{\bar{x}=\bar{x}_e \\ \bar{u}=\bar{u}_e}} \quad (4.39)$$

The equilibrium state  $\bar{x}_e$  is defined as:

$$\bar{x}_e = \left[ 0 \ 0 \ 0 \ 0 \ 0 \ 0 \ 0 \ 0 \ 0 \ 0 \ 0 \ 0 \ 0 \ 0 \ 0 \ 0 \ 0 \ 0 \right]^T \quad (4.40)$$

whereas, equilibrium inputs  $\bar{u}_e$  are determined as:

$$\bar{u}_e = \left[ 0 \ 0 \ 0 \right]^T \quad (4.41)$$

However, currently, all the 18 functions needed to define  $\hat{G}_x$  and  $\hat{G}_u$  are not available. Some of these equations can be obtained by solving for the  $\bar{y}_n$  given in eq.(4.34):

$$\bar{y}_n = (\hat{A}^*)^{-1} \bar{u}^* \quad (4.42)$$

But, recalling the elements of  $\bar{y}_n$ ,

$$\bar{y}_n = \left[ \dot{\omega}_1 \quad \dot{v}_1 \quad \ddot{\theta}_1 \dots \ddot{\theta}_m \right]^T \quad (4.43)$$

it is evident that we obtain only 9 functions from the expression obtained from eq.(4.42). Only 9 equations are obtained because  $\dot{v}_1$  does not exist among the system states given in eq.(4.7) due to the fact that we are only concerned with the rotational motion of the satellite. Therefore, the functions defining the linear accelerations of the main body  $\dot{v}_1$  are not taken into consideration.

MATLAB's Symbolics Toolbox was used for derivation of the expression in the right hand side of eq.(4.42). During this derivation it was assumed that  $\theta_m$  were small. This proved to be valid assumption since during the simulations it was observed that the deflection at the joints rarely exceeded  $0.4^\circ$ . This also implies that the hinge springs can be modeled as simple ones

since  $\theta_m$  were mainly in the region dominated by spring constant  $k_1$  (see Figure 2.7). Refer to Chapter 6 for the simulation results.

The 3 of the remaining 9 equations were obtained from kinematic expression of the quaternion vector previously given in eq.(2.73). The scalar portion of the quaternion vector ( $q_4$ ) was not considered due to the existing identities, the fourth quaternion can be calculated when the other three is available.

The last 6 functions were derived from the relations already presented in equations (2.23) and (2.24). Eq.(2.23) can be written in matrix notation as:

$$\bar{\omega}_{j/i} = \bar{\omega}_j - \hat{C}_{ji}\bar{\omega}_i \quad (4.44)$$

from which an expression for the  $\dot{\theta}_m$  can be obtained as:

$$\dot{\theta}_m = \begin{bmatrix} 0 & 0 & 1 \end{bmatrix} (\bar{\omega}_j - \hat{C}_{ji}\bar{\omega}_i) \quad (4.45)$$

Writing eq.(4.45) for all the joints, all expressions for the functions given in eq.(4.37) are obtained. The next step is to determine  $\hat{G}_x$  and  $\hat{G}_u$ . Again, MATLAB's Symbolics Toolbox was utilized to calculate derivatives existing in equations (4.38) and (4.39). Using the system parameters presented in Chapter 6, these matrices are obtained as:

$$\hat{G}_x = \begin{bmatrix} 0 & 0 & 0 & 0 & 0 & 0 & 0 & 0 & 0 & 0 & 0 & 0 & -0.0066 & 0.0072 & -0.0009 & 0.0194 & -0.0214 & 0.0026 \\ 0 & 0 & 0 & 0 & 0 & 0 & 0 & 0 & 0 & 0 & 0 & 0 & 0 & 0 & 0 & 0 & 0 & 0 \\ 0 & 0 & 0 & 0 & 0 & 0 & 0 & 0 & 0 & 0 & 0 & 0 & 0.0617 & -0.0368 & 0.0044 & 0.0616 & -0.0367 & 0.0044 \\ 0 & 0 & 0 & 0 & 0 & 0 & 0 & 0 & 0 & 0 & 0 & 0 & -1.9290 & 3.0121 & -1.5259 & -0.1013 & 0.0435 & -0.0052 \\ 0 & 0 & 0 & 0 & 0 & 0 & 0 & 0 & 0 & 0 & 0 & 0 & 3.0121 & -5.1896 & 3.3514 & 0.0436 & -0.0075 & 0.0009 \\ 0 & 0 & 0 & 0 & 0 & 0 & 0 & 0 & 0 & 0 & 0 & 0 & -1.5259 & 3.3514 & -4.0391 & -0.0052 & 0.0009 & -0.0001 \\ 0 & 0 & 0 & 0 & 0 & 0 & 0 & 0 & 0 & 0 & 0 & 0 & -0.1013 & 0.0436 & -0.0052 & -1.9471 & 3.0320 & -1.5283 \\ 0 & 0 & 0 & 0 & 0 & 0 & 0 & 0 & 0 & 0 & 0 & 0 & 0.0435 & -0.0075 & 0.0009 & 3.0320 & -5.2116 & 3.3541 \\ 0 & 0 & 0 & 0 & 0 & 0 & 0 & 0 & 0 & 0 & 0 & 0 & -0.0052 & 0.0009 & -0.0001 & -1.5283 & 3.3541 & -4.0394 \\ 0.5000 & 0 & 0 & 0 & 0 & 0 & 0 & 0 & 0 & 0 & 0 & 0 & 0 & 0 & 0 & 0 & 0 & 0 \\ 0 & 0.5000 & 0 & 0 & 0 & 0 & 0 & 0 & 0 & 0 & 0 & 0 & 0 & 0 & 0 & 0 & 0 & 0 \\ 0 & 0 & 0.5000 & 0 & 0 & 0 & 0 & 0 & 0 & 0 & 0 & 0 & 0 & 0 & 0 & 0 & 0 & 0 \\ 0 & 0 & 0 & 1.000 & 0 & 0 & 0 & 0 & 0 & 0 & 0 & 0 & 0 & 0 & 0 & 0 & 0 & 0 \\ 0 & 0 & 0 & 0 & 1.000 & 0 & 0 & 0 & 0 & 0 & 0 & 0 & 0 & 0 & 0 & 0 & 0 & 0 \\ 0 & 0 & 0 & 0 & 0 & 1.000 & 0 & 0 & 0 & 0 & 0 & 0 & 0 & 0 & 0 & 0 & 0 & 0 \\ 0 & 0 & 0 & 0 & 0 & 0 & 1.000 & 0 & 0 & 0 & 0 & 0 & 0 & 0 & 0 & 0 & 0 & 0 \\ 0 & 0 & 0 & 0 & 0 & 0 & 0 & 1.000 & 0 & 0 & 0 & 0 & 0 & 0 & 0 & 0 & 0 & 0 \\ 0 & 0 & 0 & 0 & 0 & 0 & 0 & 0 & 1.000 & 0 & 0 & 0 & 0 & 0 & 0 & 0 & 0 & 0 \end{bmatrix}$$

(4.46)

$$\hat{G}_u = \begin{bmatrix} 0.0092 & 0 & 0 \\ 0 & 0.0034 & 0 \\ 0 & 0 & 0.0141 \\ 0.0033 & 0 & -0.0309 \\ -0.0036 & 0 & 0.0184 \\ 0.0004 & 0 & -0.0022 \\ -0.0097 & 0 & -0.0308 \\ 0.0107 & 0 & 0.0183 \\ -0.0013 & 0 & -0.0022 \\ 0 & 0 & 0 \\ 0 & 0 & 0 \\ 0 & 0 & 0 \\ 0 & 0 & 0 \\ 0 & 0 & 0 \\ 0 & 0 & 0 \\ 0 & 0 & 0 \\ 0 & 0 & 0 \\ 0 & 0 & 0 \end{bmatrix} \quad (4.47)$$

Thus, the multi-body system can now be represented in the vicinity of the equilibrium point  $\bar{x}_e$  by:

$$\dot{\bar{x}} = \hat{G}_x \bar{x} + \hat{G}_u \bar{u} \quad (4.48)$$

The eigenvalues of this system is obtained and plotted in Figure 4.1.

Note that the uncontrolled system is marginally stable with inherent oscillations due to nonzero imaginary values. This is actually what had been expected from a mechanical system including springs with no damping. There also exists multiple (six) zeros at the origin corresponding to the six rigid body modes (three angular rates and three quaternions) in the uncontrolled system, which is also expected. Thus, the system obtained so far is coincident with what had been anticipated.

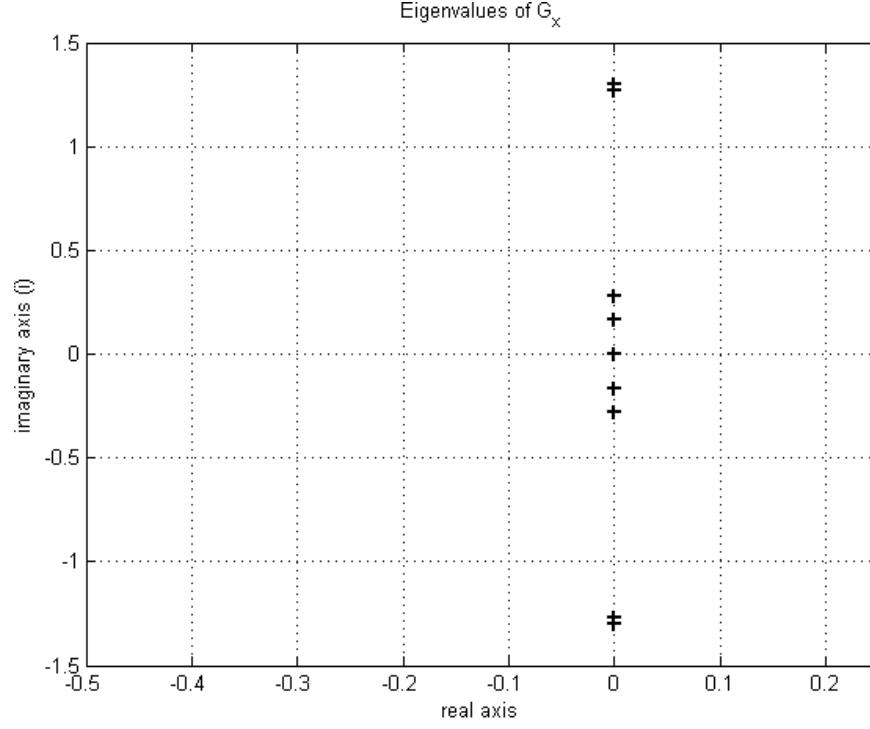


Figure 4.1: Eigenvalues of the state Jacobian matrix  $G_x$

Controllability of the system given in eq.(4.48) is also checked. The controllability matrix  $\hat{M}$  is built by using the expression<sup>[26]</sup>:

$$\hat{M} = \begin{bmatrix} \hat{G}_u & \hat{G}_x \hat{G}_u & \cdots & \hat{G}_x^{17} \hat{G}_u \end{bmatrix} \quad (4.49)$$

Resorting to MATLAB's built in "ctrb" function due to the computational load of eq.(4.49), the controllability matrix was obtained. Its rank was determined as 18, which also happens to be the order of the system. Therefore, the system presented in eq.(4.48) was controllable.

#### 4.2.3 Determining the Feedback Gain

For the SFB controller, the gain matrix  $\hat{K}$  given in eq.(4.5) is obtained by LQR approach. In this method  $\hat{K}$  is determined such that the performance index<sup>[15]</sup>:

Table 4.1: Maximum values for states and inputs

States/Inputs	Maximum Value	Unit
$\omega_1, \omega_2, \omega_3$	0.044	rad/s
$\dot{\theta}_1, \dot{\theta}_2, \dot{\theta}_3, \dot{\theta}_4, \dot{\theta}_5, \dot{\theta}_6$	0.035	rad/s
$q_1, q_2, q_3$	1	N/A
$\theta_1, \theta_2, \theta_3, \theta_4, \theta_5, \theta_6$	0.007	rad
$T_{1x}, T_{1y}, T_{1z}$	0.5	Nm

$$N_{Perf} = \int_0^{\infty} (\bar{x}^T \hat{Q} \bar{x} + \bar{u}^T \hat{R} \bar{u}) dt \quad (4.50)$$

is minimized. Symmetric matrices  $\hat{Q}$  and  $\hat{R}$  provide the weighting for the elements of the performance index. Using these matrices together with the system matrices  $\hat{G}_x$  and  $\hat{G}_u$ , the reduced matrix Riccati equation can be obtained as:

$$\hat{G}_x^T \hat{P} + \hat{P} \hat{G}_x - \hat{P} \hat{G}_u \hat{R}^{-1} \hat{G}_u^T \hat{P} + \hat{Q} = \hat{0} \quad (4.51)$$

To determine  $\hat{K}$ , eq.(4.51) is solved for  $\hat{P}$ . Then the gain matrix is determined from:

$$\hat{K} = \hat{R}^{-1} \hat{G}_u^T \hat{P} \quad (4.52)$$

Again, the computational complexity involved due to the large matrices prompts us to utilize built-in MATLAB commands. The command "lqr" is used to determine the  $\hat{K}$  from available  $\hat{G}_x$ ,  $\hat{G}_u$ ,  $\hat{Q}$  and  $\hat{R}$ . The tuning process of LQR method is mainly compromised of determining  $\hat{Q}$  and  $\hat{R}$  (hence the relative importances) that will yield the desired solution for the particular application.

While determining the relative importances among the states and inputs, normalization have to be carried out. States and inputs may span several order of magnitudes, resulting in difficulties whilst determining relative importances. In this study, normalization is carried out by dividing the states and inputs with their maximum values. These values are collected from the simulations and presented in Table 4.1.

With the help of these values,  $\hat{Q}$  can be determined as:

$$\begin{aligned}
\hat{Q} = & \text{diag}(22.73w_{Q1}, 22.73w_{Q2}, 22.73w_{Q3}, \\
& 22.57w_{Q4}, 22.57w_{Q5}, 22.57w_{Q6}, 22.57w_{Q7}, 22.57w_{Q8}, 22.57w_{Q9}, \\
& w_{Q10}, w_{Q11}, w_{Q12}, \\
& 142.86w_{Q13}, 142.86w_{Q14}, 142.86w_{Q15}, 142.86w_{Q16}, 142.86w_{Q17}, 142.86w_{Q18})
\end{aligned} \tag{4.53}$$

where  $w_{Qi}$  are the weights and  $\text{diag}()$  is a diagonal matrix formed from the listed elements. Similarly, for  $\hat{R}$ ;

$$\hat{R} = \text{diag}(2w_{R1}, 2w_{R2}, 2w_{R3}) \tag{4.54}$$

Using equations (4.53) and (4.54), relative importances can now be allocated to the states and inputs.

## CHAPTER 5

### POINTING PERFORMANCE

In this study, the main aim is to assess the satellite pointing performance; therefore some metrics for evaluation of different controller schemes have to be obtained. Pointing metrics address this particular problem. In this chapter, the definition of pointing performance metrics will be presented first. Later, an algorithm for obtaining these metrics from a time domain simulation will be introduced.

#### 5.1 Performance Metrics

Several pointing metrics exist for assessing the spacecraft pointing performance. These can be named as accuracy, displacement, jitter, stability and windowed stability<sup>[5]</sup>. In this study, only accuracy, jitter and stability metrics are considered. These will be briefly described shortly. However, before introducing them, it is advisable to elaborate more on the imaging process given in Figure 5.1:

The imaging process is as follows; when the satellite settles in a certain prescribed attitude, the payload is operated. The payload is commanded to take images, which it does during the exposure time  $T_E$ . Having finished collecting the image, the payload proceeds to registering the image in its memory and preparing for the next imaging sequence during the readout time  $T_{RO}$ .

Basic definitions of accuracy, jitter and stability metrics can be presented as<sup>[5]</sup>:

*Accuracy Metric.* It can be described as the root mean square of the pointing error. In this study, the accuracy in three body axes is taken into account; therefore accuracy metric was



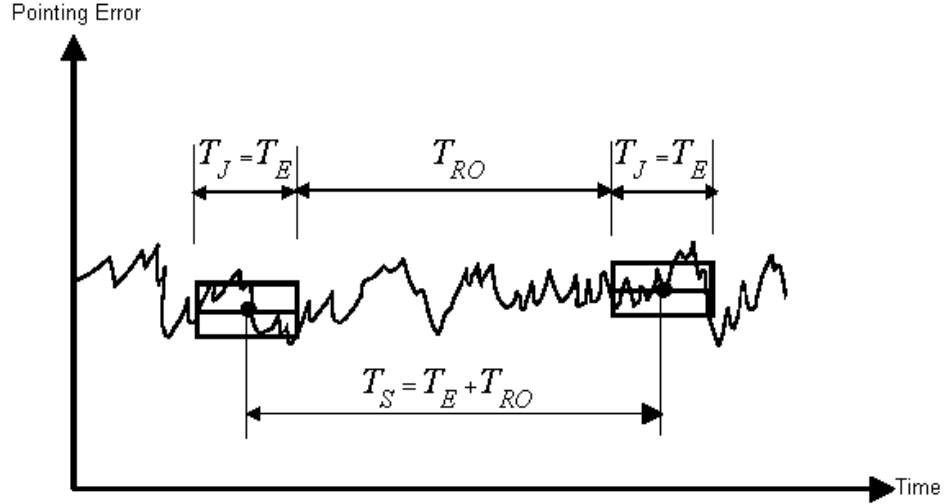


Figure 5.1: Representative attitude error plot together with the steps of imaging process exposure time  $T_E$  and readout time  $T_{RO}$

obtained for all three axes. Its unit is in ( $^\circ$ ) and formulated using:

$$\sqrt{\sigma_a^2 + \mu^2} \quad (5.1)$$

where,  $\sigma_a$  is the variance and  $\mu$  is the mean of pointing error.

*Jitter Metric.* It is defined as the root mean square motion within the jitter time window  $T_j$ . In this study, it is assumed that jitter time window equals the exposure time ( $T_j = T_E$ ). Its unit is in  $^\circ/s$ . High frequency motions of the satellite contribute to this metric. It is also considered in each body axes directions; thus obtained in all three of them. It is denoted by  $\sigma_j$ .

*Stability Metric.* It can be described as the root mean square of the change in pointing from the beginning to the end of stability time interval  $T_s$ . This interval corresponds to the duration between the operations of imaging instrument. For this case, it is assumed that the stability time equals to the summation of exposure and readout times ( $T_s = T_E + T_{RO}$ ). The unit of the stability metric is  $^\circ$ . This metric is also considered in all three body axes directions. It is denoted by  $\sigma_s$ .

Table 5.1: Algorithm for obtaining the pointing metrics from time sampled data

Step	Instruction
1	sample attitude error data with constant $\Delta t$
2	transform sampled data to frequency domain (FFT)
3	obtain the power spectrum of the transformed data
4	shift the power spectrum (center the $f = 0 \text{ Hz}$ point)
5	multiply by the weighting functions $W_j$ and $W_s$
6	sum across the frequency range

## 5.2 Metric Calculation Algorithm

The calculation of the pointing metrics is carried out in frequency domain. The algorithm consists of following steps. First, uniformly sampled attitude error data is transformed to the frequency domain using Fast Fourier Transform (FFT) algorithm. Then the power spectrum of transformed data is obtained by dividing the transformed data with the number of samples and taking the square of the magnitude of the result. Later, the obtained data is shifted so that zero frequency is at the center in the plot. After this process, the obtained data is multiplied by the weighting functions (Figure 5.2) and summed across the frequency range so that the variances of the desired pointing metrics can be obtained<sup>[5]</sup>. This process is summarized in Table 5.1.

The weighting function used for the jitter metric is:

$$W_j(\omega T_j) = 1 - 2 \frac{1 - \cos(\omega T_j)}{(\omega T_j)^2} \quad (5.2)$$

The weighting function for the stability is:

$$W_s(\omega T_s) = 2(1 - \cos(\omega T_s)) \quad (5.3)$$

The functions given in equations (5.2) and (5.3) are plotted in Figure 5.2. Note that, the jitter function mainly takes the high frequency disturbances into account as expected.

As mentioned above, the accuracy metric is calculated by summation:

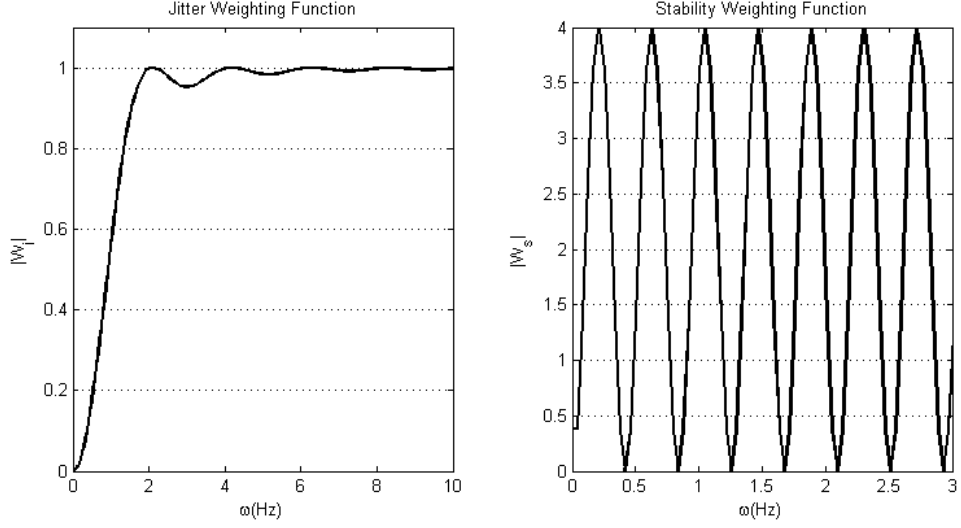


Figure 5.2: Weighting functions for jitter ( $W_j$ ) and stability ( $W_s$ )

$$\sqrt{\sigma_a^2 + \mu^2} = \sqrt{\sum_{i=1}^M P_{spec}(\omega_i)} \quad (5.4)$$

where  $P_{spec}(\omega)$  is the power spectrum of the attitude error data consisting of  $M$  entries, which corresponds to 15000 entries in our simulations (last 150 s of simulation with a time step of 0.01 s was taken into consideration in order to account for settling in new orientation). With the help of eq.(5.2), a similar expression for the jitter metric is also obtained:

$$\sigma_j = \sqrt{\sum_{i=1}^M P_{spec}(\omega_i) W_j(\omega_i T_j)} \quad (5.5)$$

In similar fashion the stability metric becomes:

$$\sigma_s = \sqrt{\sum_{i=1}^M P_{spec}(\omega_i) W_s(\omega_i T_s)} \quad (5.6)$$

As it easily be inferred from equations (5.5) and (5.6), jitter and stability time windows  $T_j$  and  $T_s$  have to be defined in order to calculate the metrics as well. For the calculations, it was assumed that the exposure time  $T_E$  of the imaging instrument onboard the spacecraft is 3 s; whereas the readout time  $T_{RO}$  was chosen as 12 s.

## CHAPTER 6

### RESULTS AND DISCUSSION

With the parameters already presented in Tables 2.2, 2.3, 2.4, 2.5 (only applicable to SFB controller), 3.2 and 3.3; simulations were run for QFB and SFB controllers. First, the QFB controller was optimized with direct methods using pointing metrics as performance indexes and optimal  $K_p$  and  $K_d$  values were obtained. Consequently, this optimal QFB controller was simulated in detail and system variables were recorded. Similarly, tuned SFB controller with a controller gain matrix  $\hat{K}$  (obtained by LQR approach) was also simulated and its system variables were recorded. Comparisons were made between these two simulations utilizing different controllers.

#### 6.1 Optimization for QFB Controller

Since theoretical methods for determining the controller gains of the QFB controller were unavailable, an optimization process was carried out. During this optimization process proportional gain constant  $K_p$  was varied from 0 to 11 whereas derivative gain constant  $K_d$  was varied from 0 to 55 in order to observe the performance of QFB controller for different gain selections. The limits of this "gain grid" were chosen arbitrarily. Pointing metrics were calculated at each point on this grid. Figures 6.1, 6.2 and 6.3 present the accuracy metric  $3\sigma_a$  obtained for roll, pitch and yaw axes for every point in the gain grid. Similarly, Figures 6.4, 6.5 and 6.6 present the stability metric  $3\sigma_s$  obtained for each axis, whereas jitter metric  $3\sigma_j$  for each axis is given in Figures 6.7, 6.8 and 6.9. In the figures, only values smaller than  $0.1^\circ$  for the accuracy and stability metrics and the values smaller than  $0.02^\circ/s$  for the jitter metric were taken into consideration.

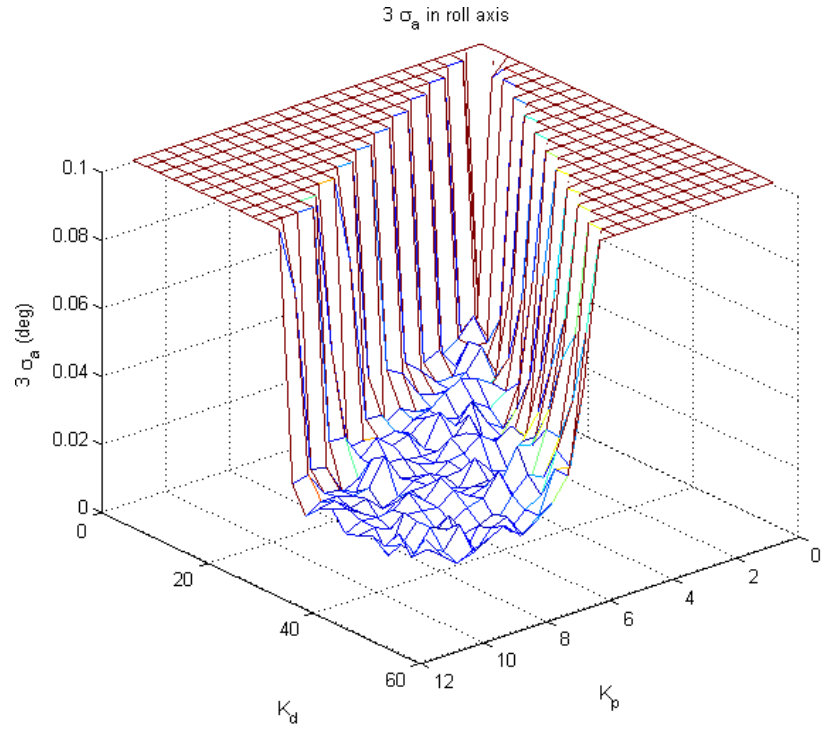


Figure 6.1:  $3\sigma_a$  values (in  $^\circ$ ) obtained in roll axis for different  $K_p$  and  $K_d$  values

At the end of the optimization, the optimum gains were obtained as  $K_p = 10$  and  $K_d = 55$ . One key observation that can be made from Figures 6.1 to 6.9 is that; between certain ratios of  $K_p/K_d$ , satisfactory results are obtained and a "boundary" in which satisfactory results are prevalent is evident. This boundary is seemed to be limited by the ratios  $K_p/K_d = 8$  and  $K_p/K_d = 2.5$ .

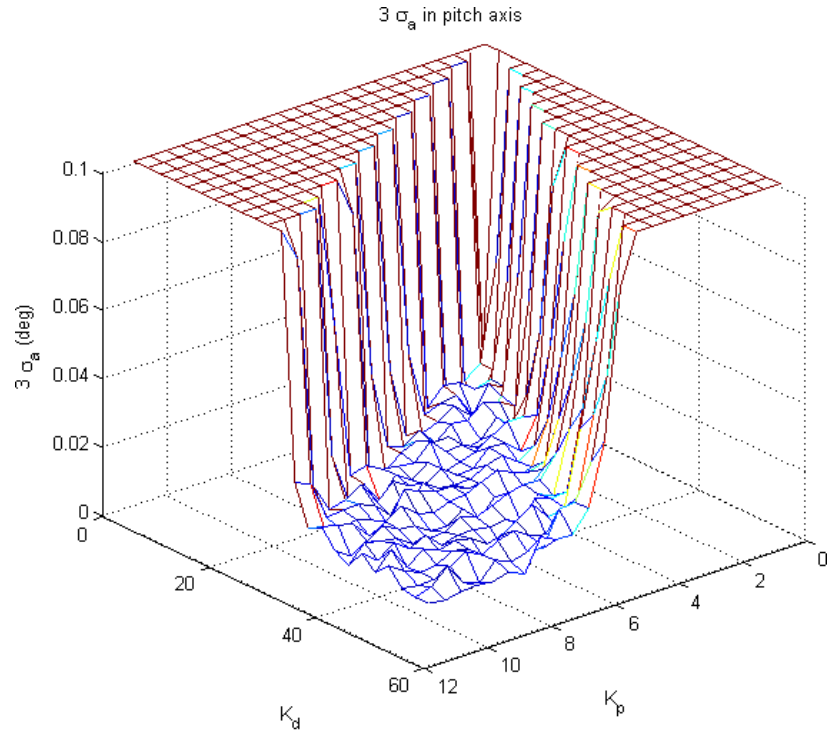


Figure 6.2:  $3\sigma_a$  values (in  $^\circ$ ) obtained in pitch axis for different  $K_p$  and  $K_d$  values

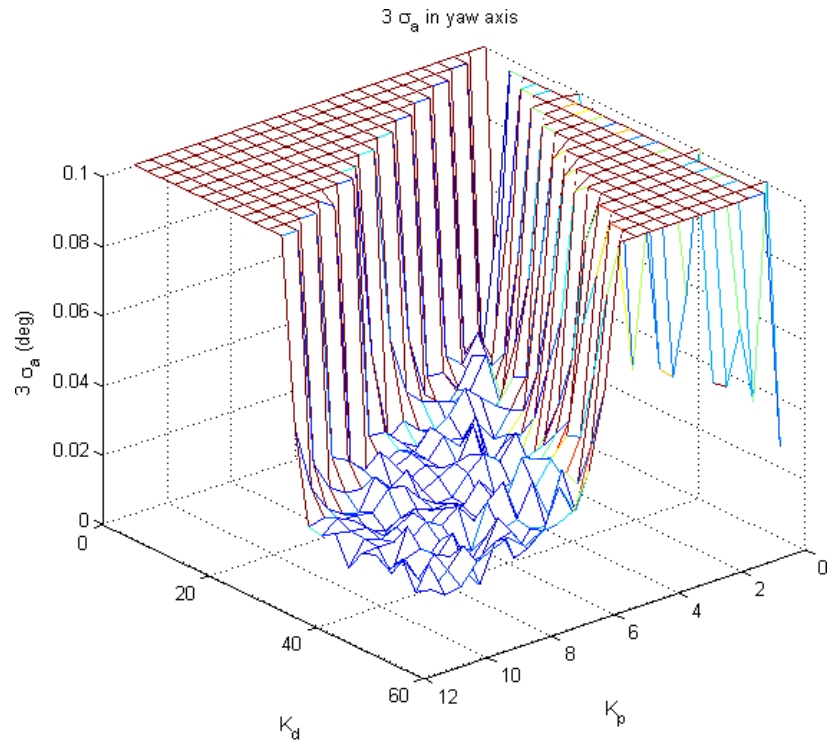


Figure 6.3:  $3\sigma_a$  values (in  $^\circ$ ) obtained in yaw axis for different  $K_p$  and  $K_d$  values

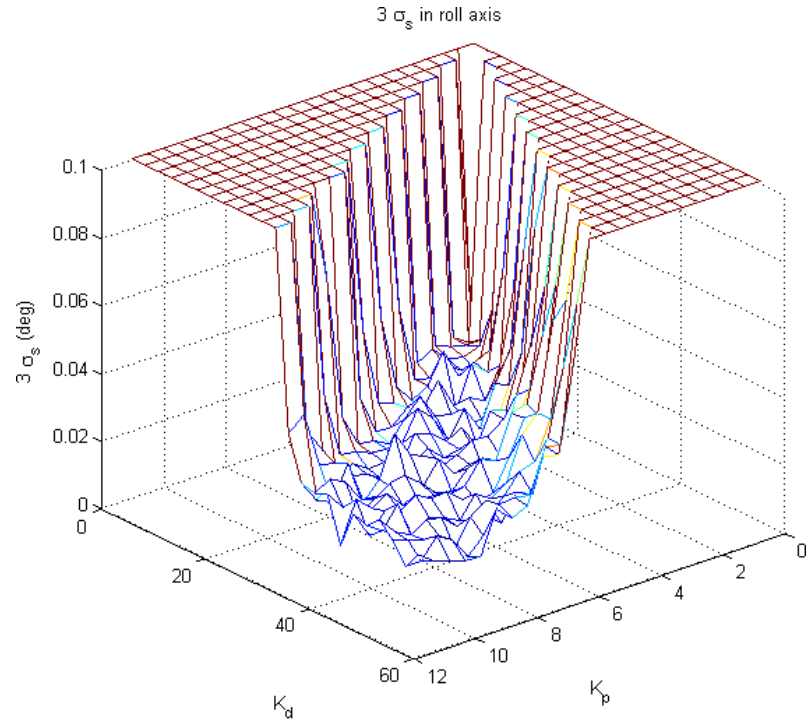


Figure 6.4:  $3\sigma_s$  values (in  $^\circ$ ) obtained in roll axis for different  $K_p$  and  $K_d$  values

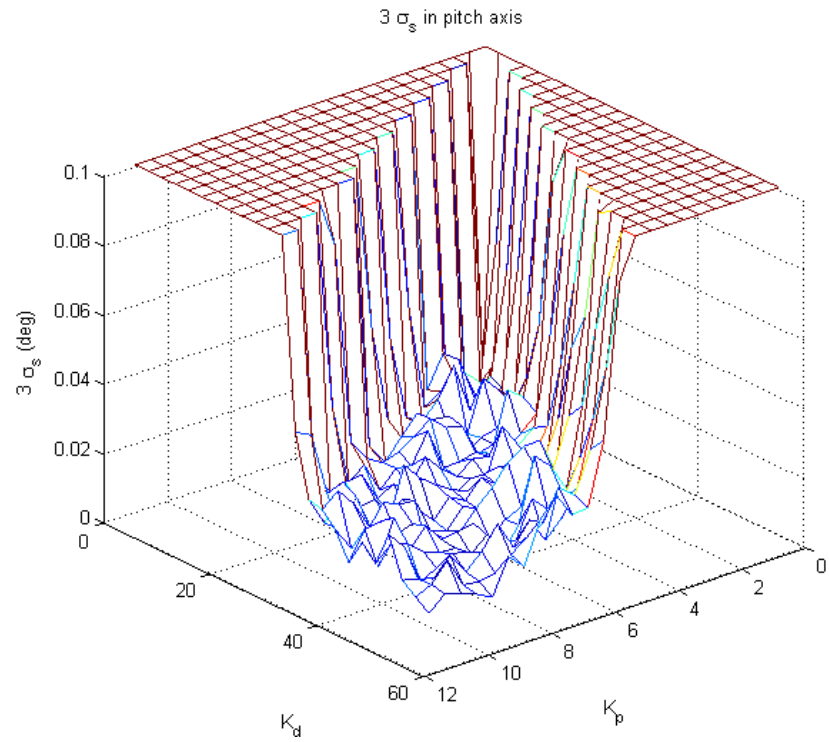


Figure 6.5:  $3\sigma_s$  values (in  $^\circ$ ) obtained in pitch axis for different  $K_p$  and  $K_d$  values

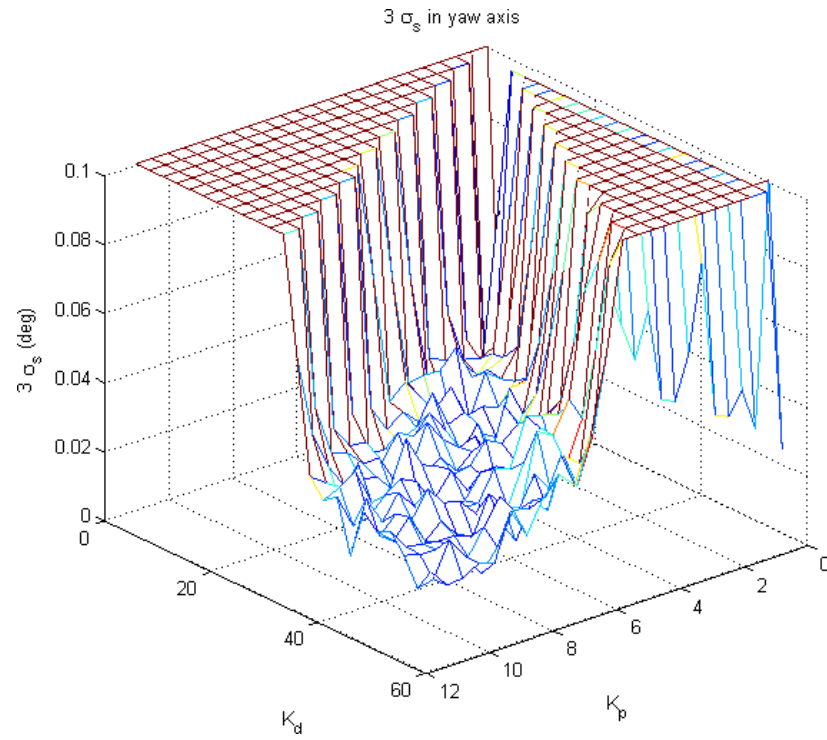


Figure 6.6:  $3\sigma_s$  values (in  $^\circ$ ) obtained in yaw axis for different  $K_p$  and  $K_d$  values

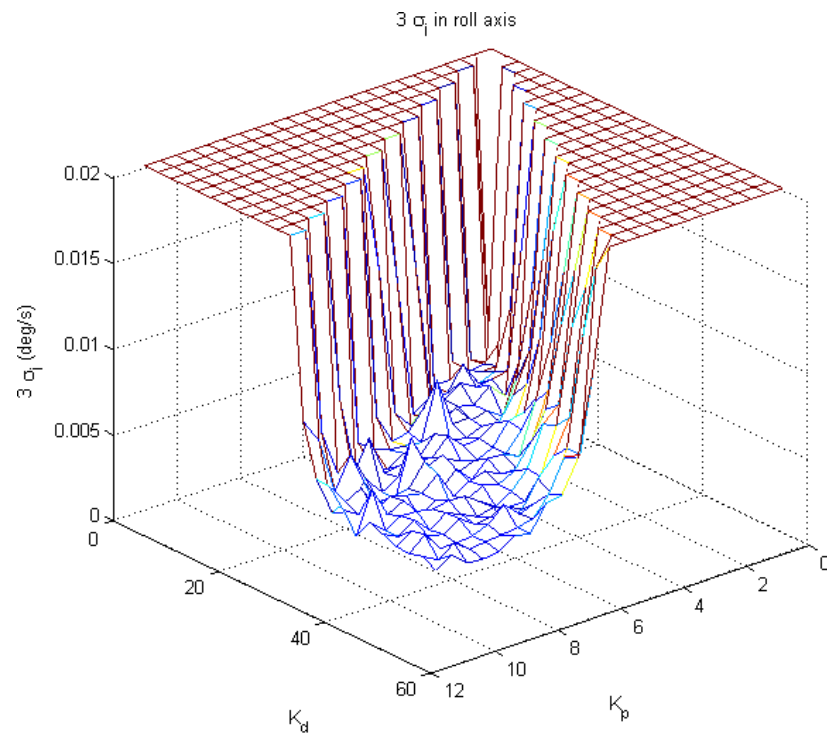


Figure 6.7:  $3\sigma_j$  values (in  $^\circ/\text{s}$ ) obtained in roll axis for different  $K_p$  and  $K_d$  values



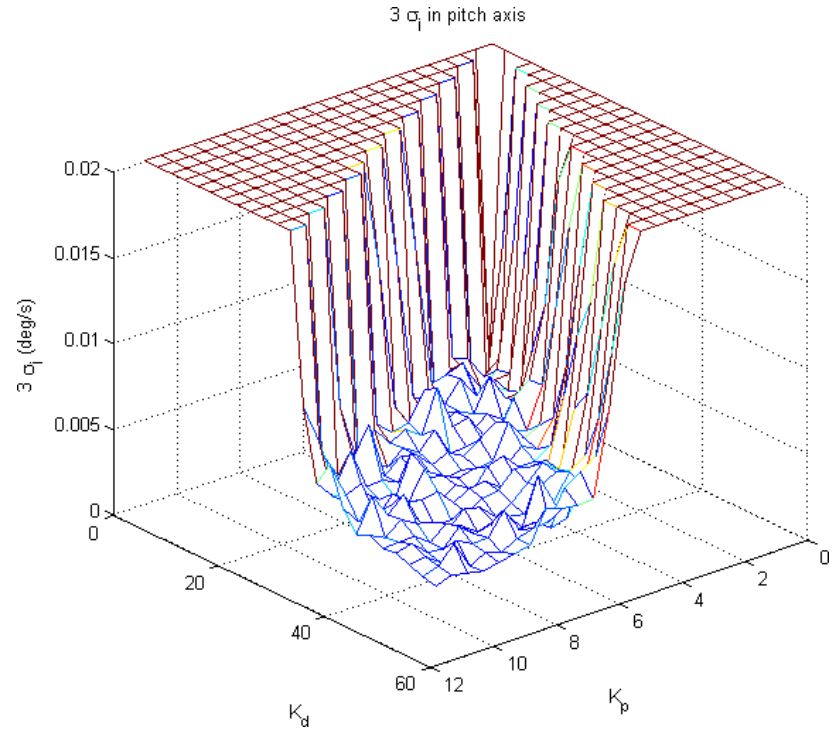


Figure 6.8:  $3\sigma_j$  values (in  $^{\circ}/s$ ) obtained in pitch axis for different  $K_p$  and  $K_d$  values

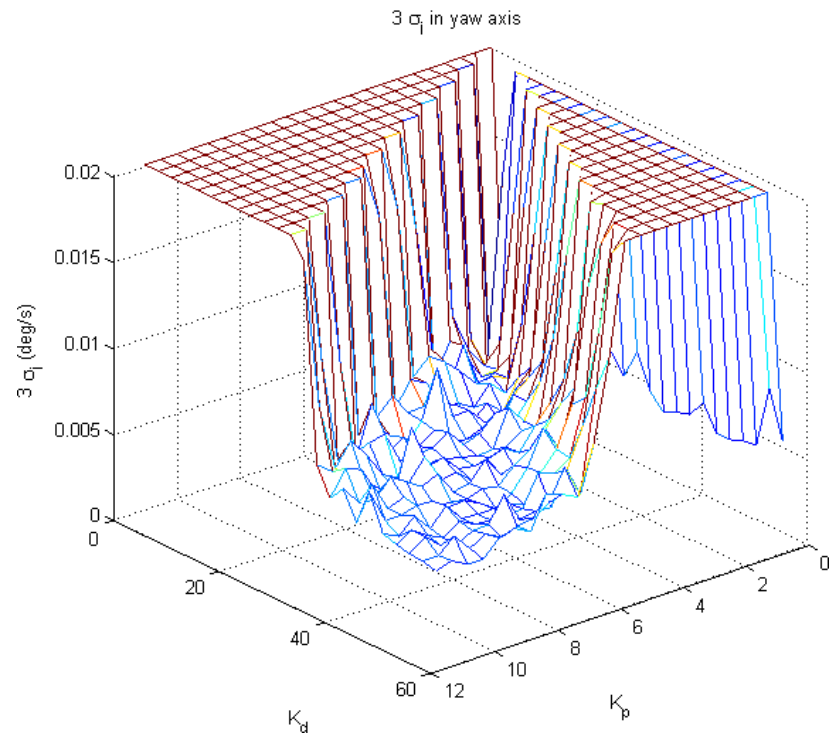


Figure 6.9:  $3\sigma_j$  values (in  $^{\circ}/s$ ) obtained in yaw axis for different  $K_p$  and  $K_d$  values

Table 6.1: Pointing metrics for the QFB controller

Axis	$3\sigma_a$ (°)	$3\sigma_s$ (°)	$3\sigma_j$ (°/s)
Roll	0.0140	0.0200	0.0046
Pitch	0.0131	0.0149	0.0034
Yaw	0.0163	0.0229	0.0048

## 6.2 Simulation Results

A slew maneuver of 60 ° roll, 60 ° pitch and 0 ° yaw is simulated for 299.99 s with a time step of 0.01 s. It is assumed that all initial Euler angles are set to 0 °. Similarly, all the body rates are also assumed to be 0 °/s. Same initial condition assumptions are also valid for the joint angular position ( $\theta_m$ ) and rates ( $\dot{\theta}_m$ ).

### 6.2.1 Results for QFB Controller

QFB controller was able to successfully reorient the spacecraft. Pointing metrics obtained from the simulation are presented in Table 6.1. Relevant data is presented in the following figures.

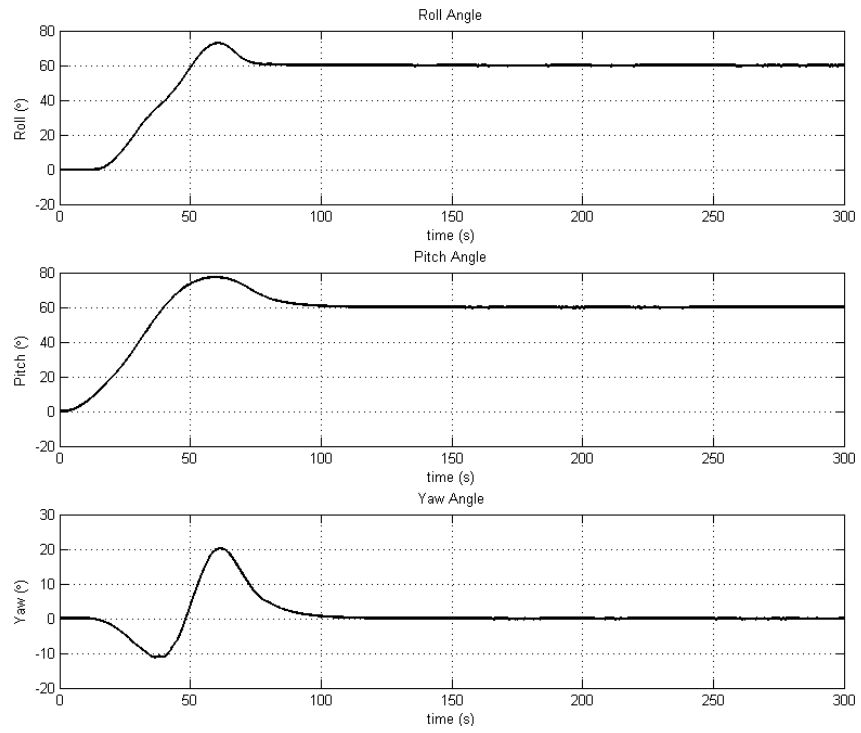


Figure 6.10: Attitude history of the satellite main body (QFB controller)

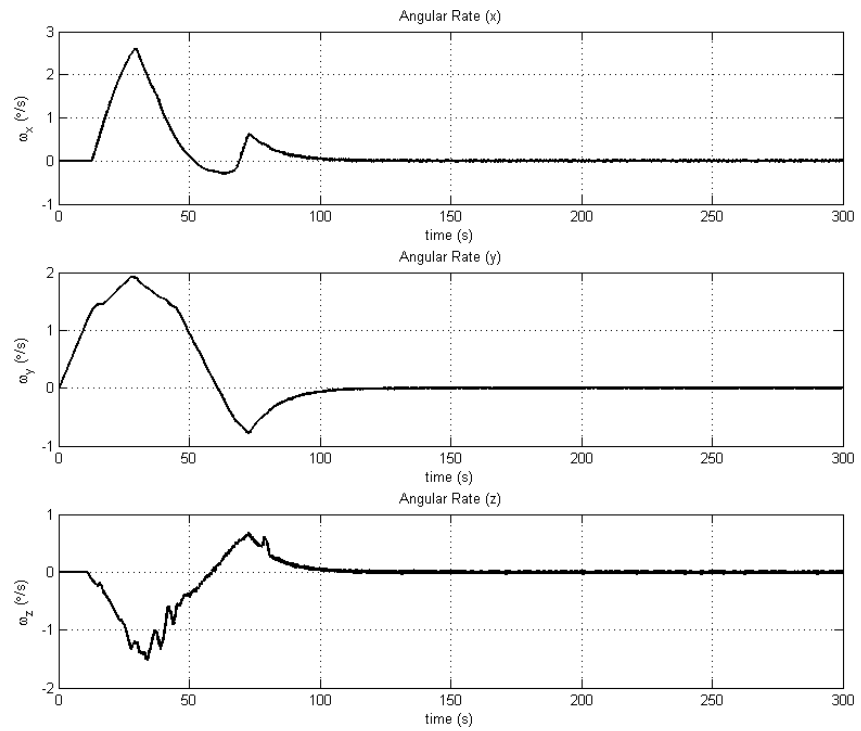


Figure 6.11: Main body angular rates for the duration of simulation (QFB)

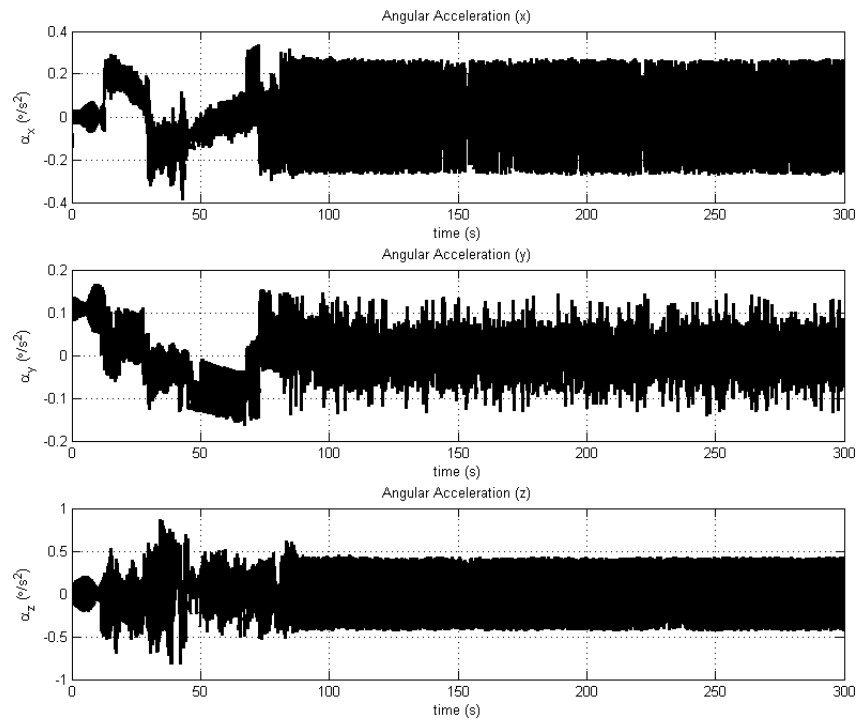


Figure 6.12: Main body angular accelerations for the duration of simulation (QFB)

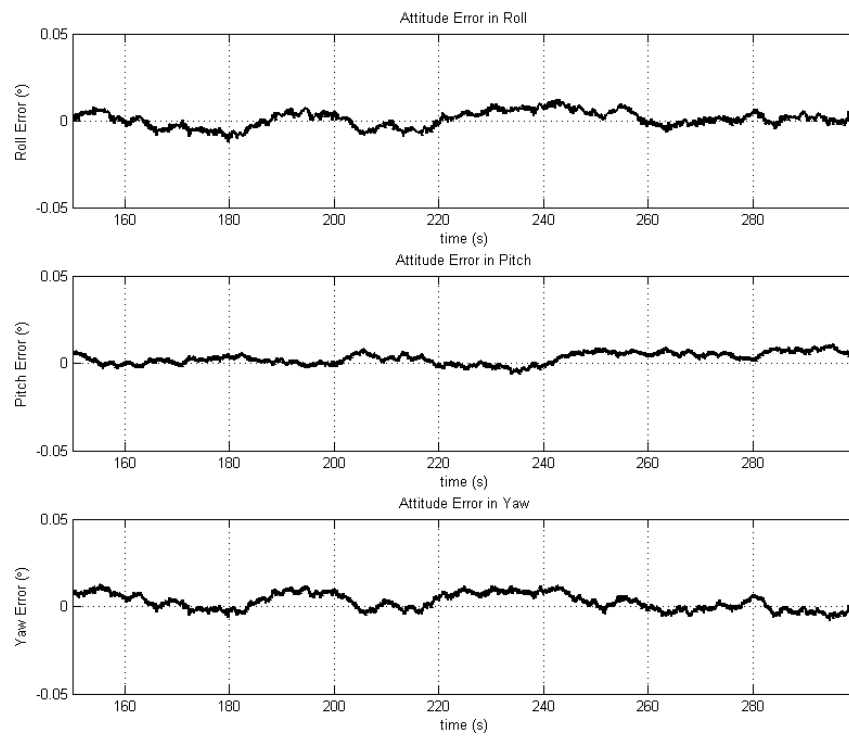


Figure 6.13: Detail from attitude error for the last 150 s of simulation (QFB)

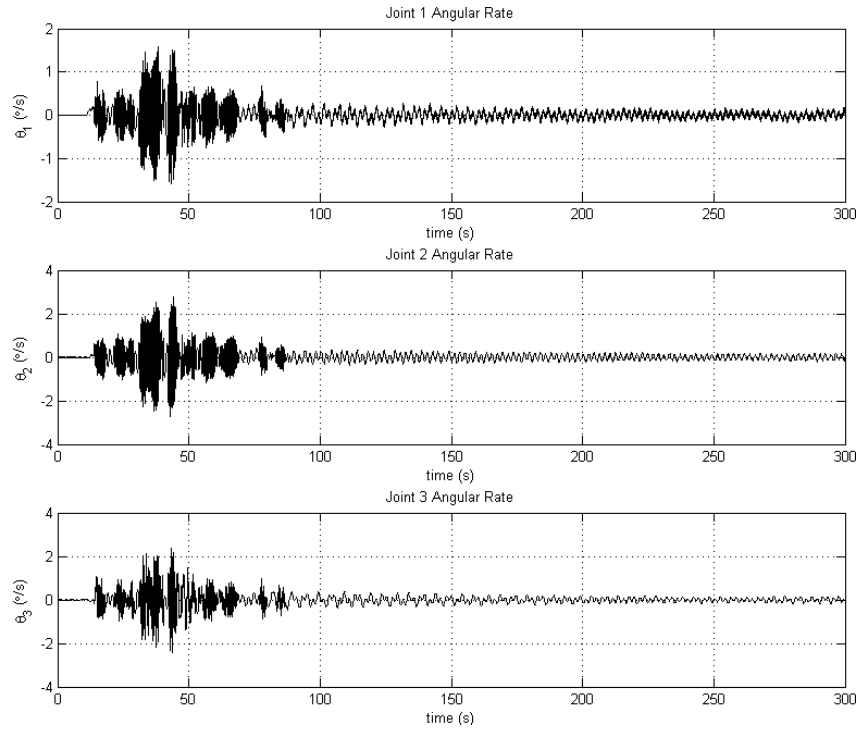


Figure 6.14: Joint angular velocities for the solar array 1 (QFB)

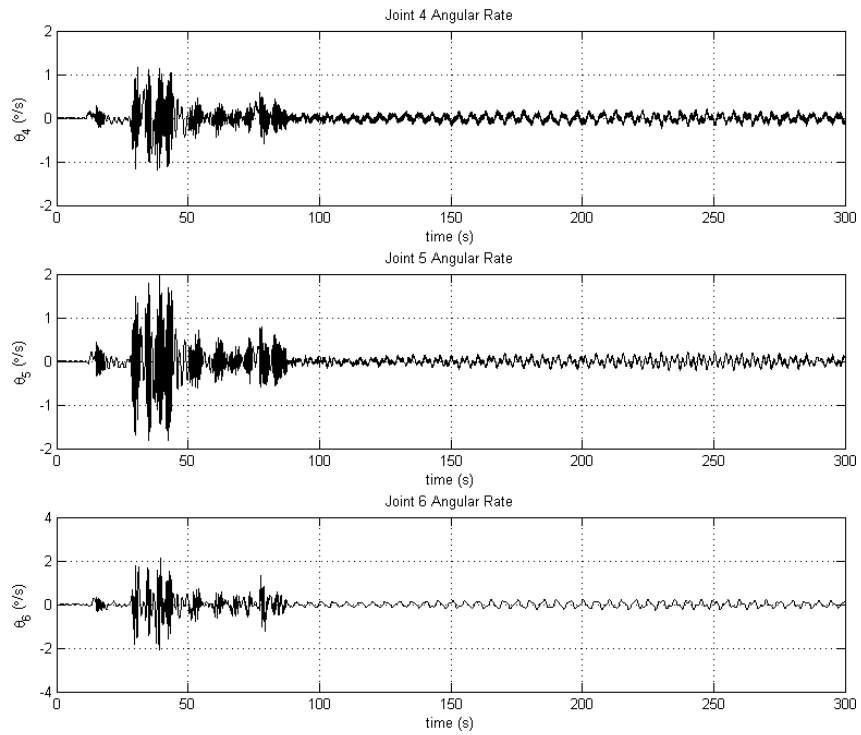


Figure 6.15: Joint angular velocities for the solar array 2 (QFB)

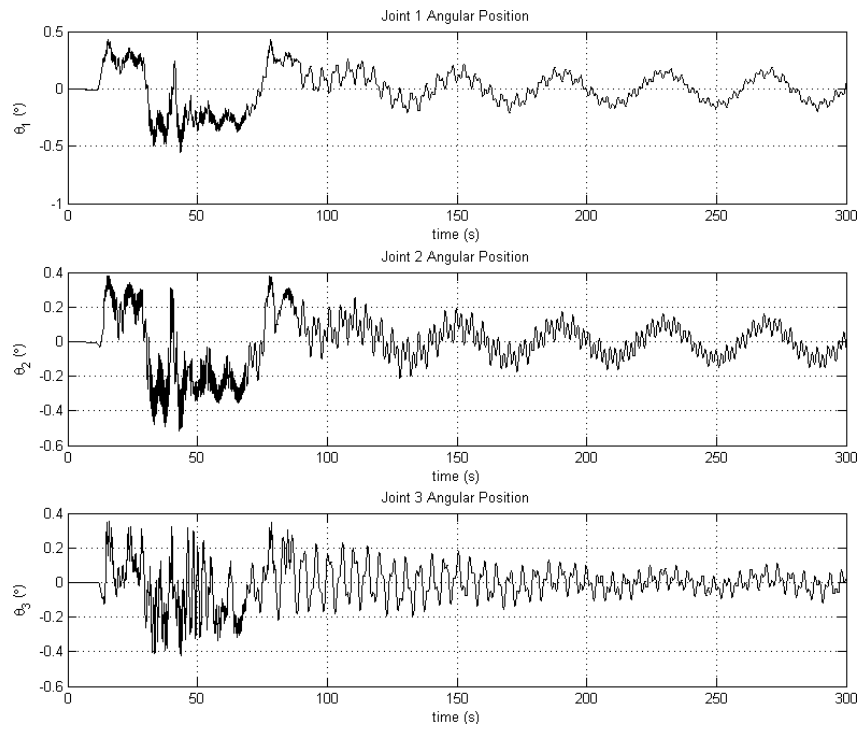


Figure 6.16: Joint angular positions for the solar array 1 (QFB)

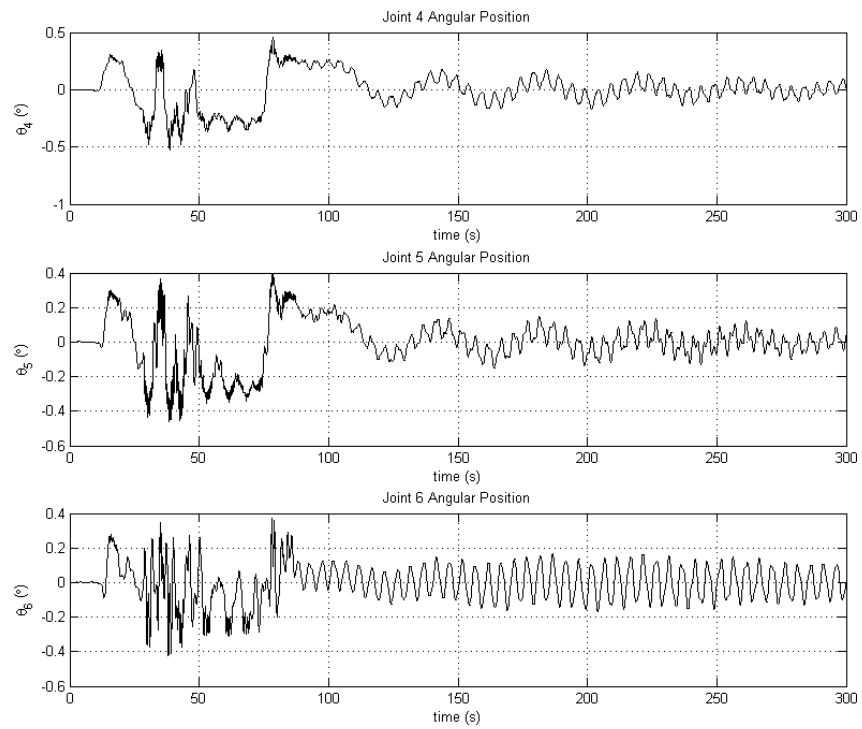


Figure 6.17: Joint angular positions for the solar array 2 (QFB)

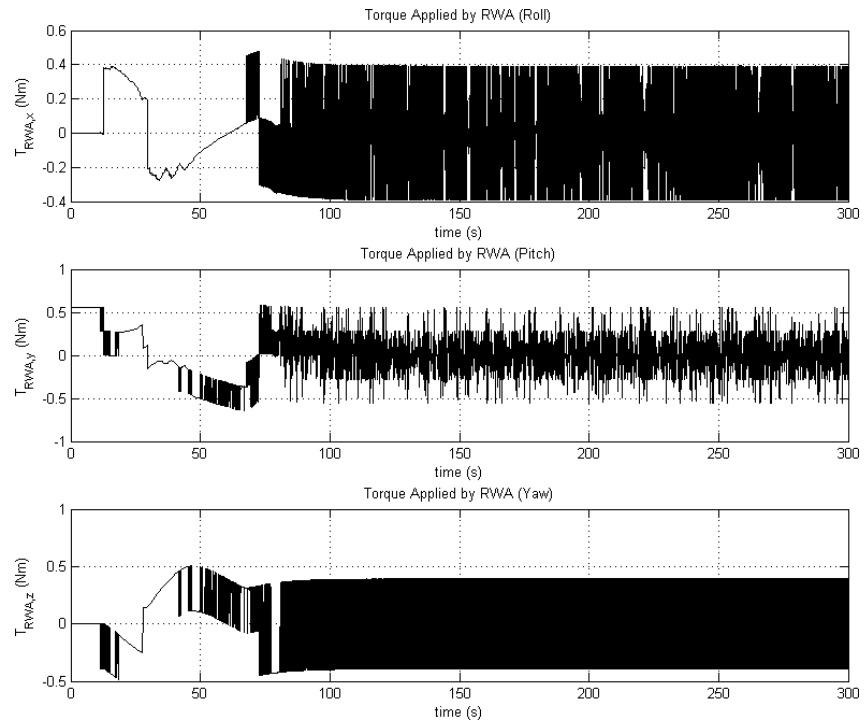


Figure 6.18: Actuator torque being applied on the satellite (QFB)

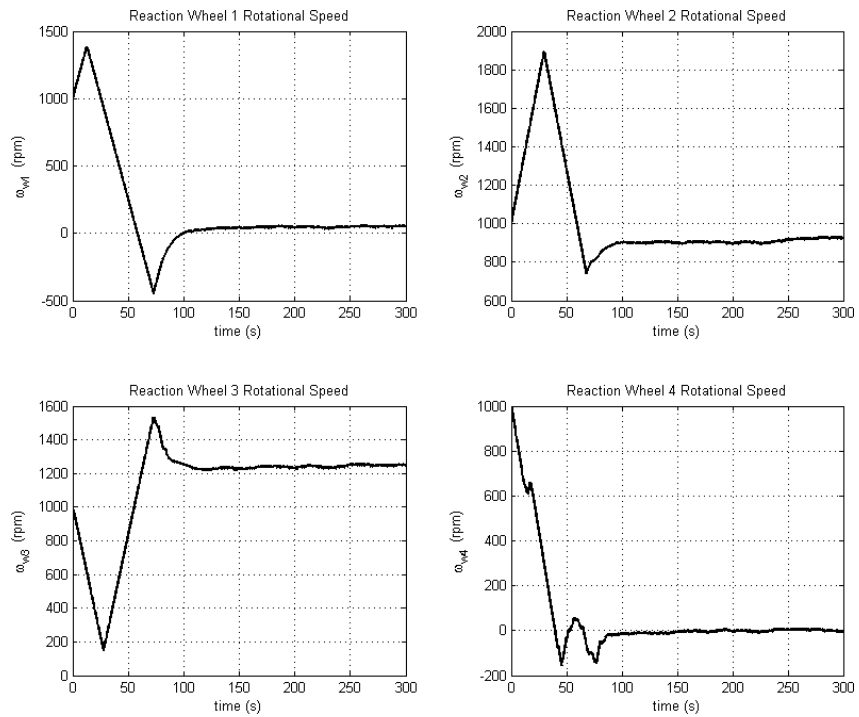


Figure 6.19: Reaction wheel angular velocities (QFB)

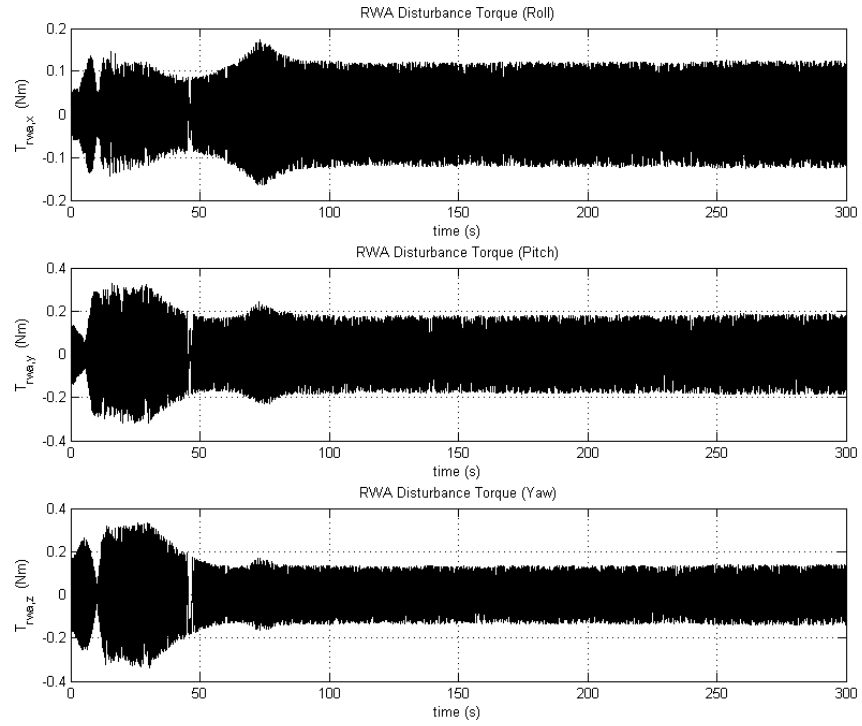


Figure 6.20: Disturbance torques due to reaction wheels acting on the satellite (QFB)

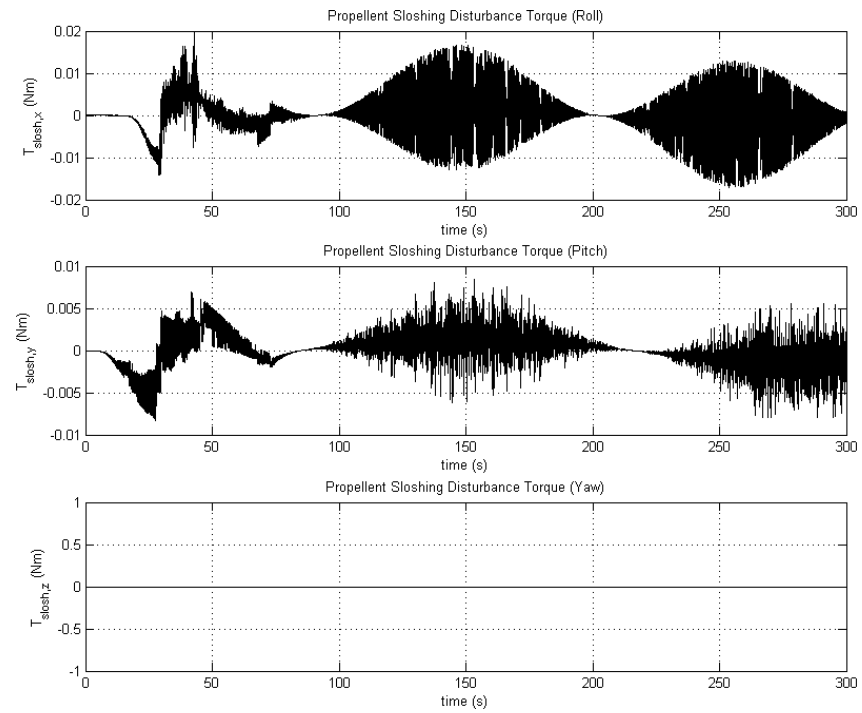


Figure 6.21: Disturbance torques due to propellant sloshing acting on the satellite (QFB)



Table 6.2: Pointing metrics for the SFB controller

Axis	$3\sigma_a$ (°)	$3\sigma_s$ (°)	$3\sigma_j$ (°/s)
Roll	0.0276	0.0259	0.0042
Pitch	0.0123	0.0116	0.0027
Yaw	0.0218	0.0199	0.0032

### 6.2.2 Results for SFB Controller

SFB controller also successfully reoriented the spacecraft. The relative importance coefficients introduced in equations 4.53 and 4.53 were chosen such that;  $w_{Q1} = w_{Q2} = w_{Q3} = 900$ ,  $w_{Q4} = \dots = w_{Q9} = 5$ ,  $w_{Q10} = w_{Q11} = w_{Q12} = 15000$ ,  $w_{Q13} = \dots = w_{Q18} = 1$  and  $w_{R1} = w_{R2} = w_{R3} = 31$ . Pointing metrics obtained from the simulation are presented in Table 6.2. Simulation data is available in the following plots.

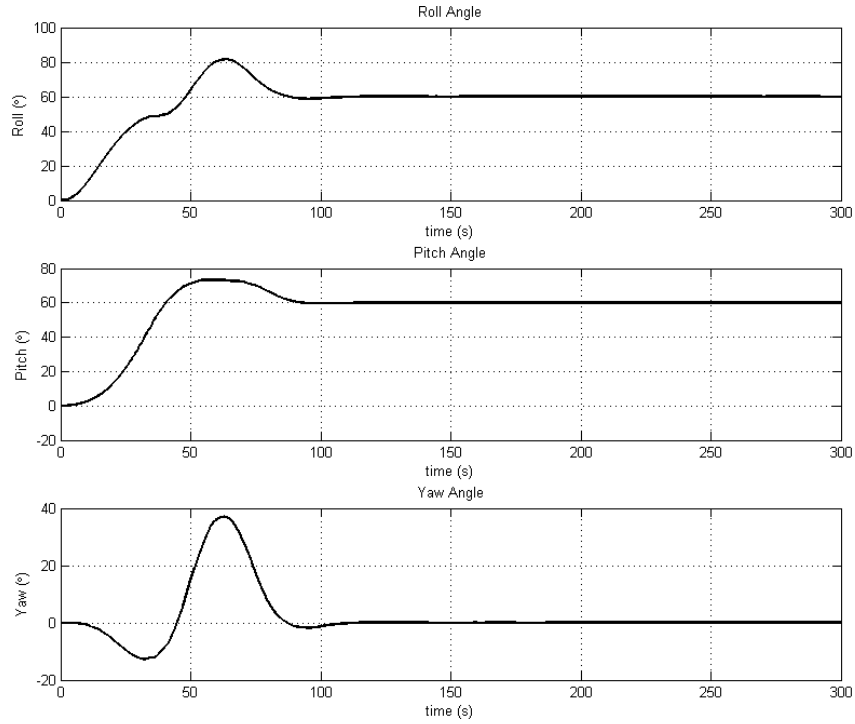


Figure 6.22: Attitude history of the satellite main body (SFB Controller)

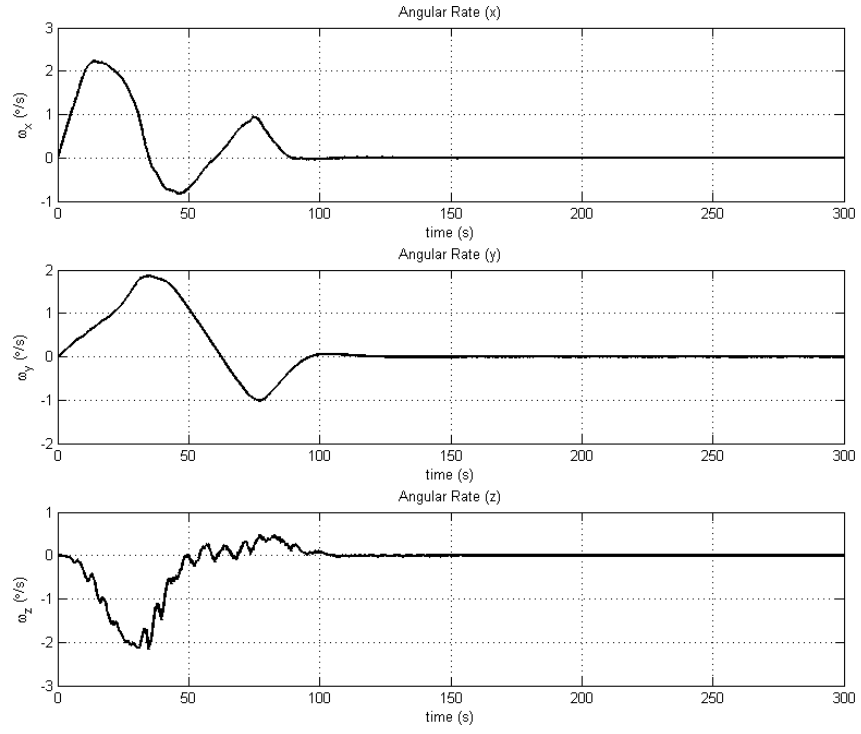


Figure 6.23: Main body angular rates for the duration of simulation (SFB)

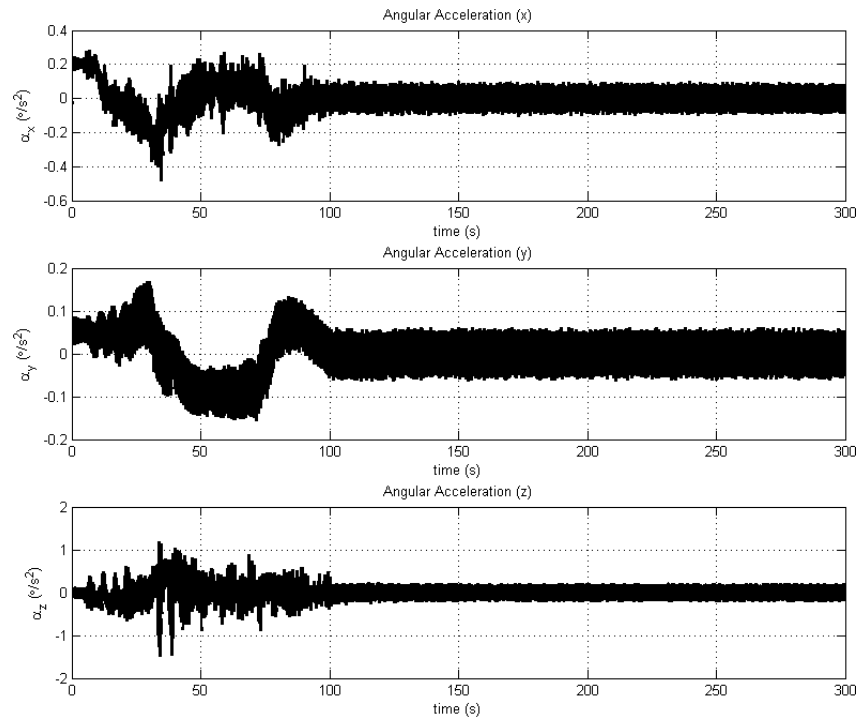


Figure 6.24: Main body angular accelerations for the duration of simulation (SFB)

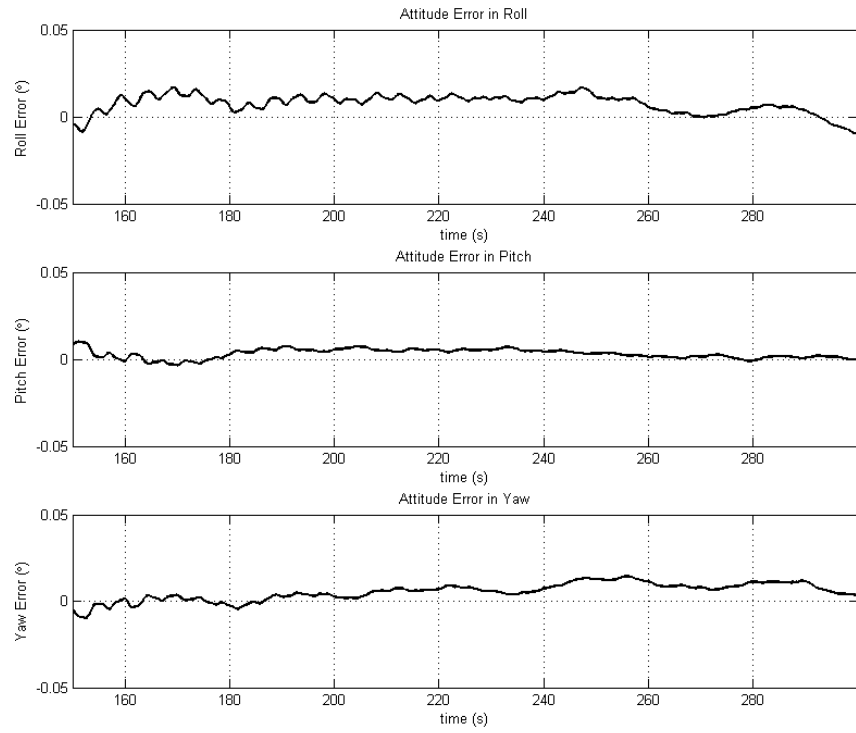


Figure 6.25: Detail from attitude error from the last half of the simulation (SFB)

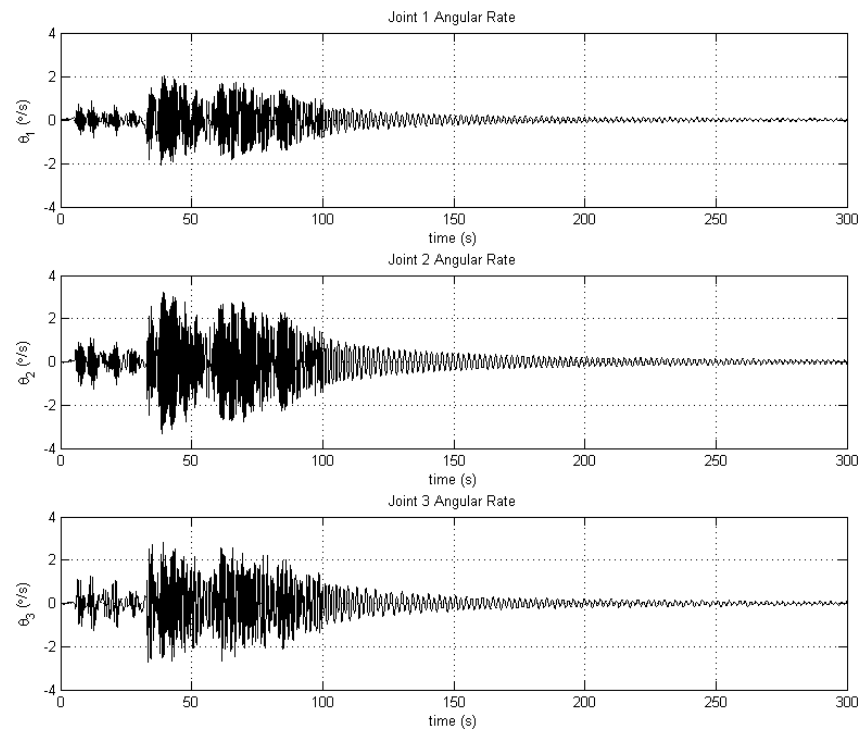


Figure 6.26: Joint angular velocities for the first solar array (SFB)

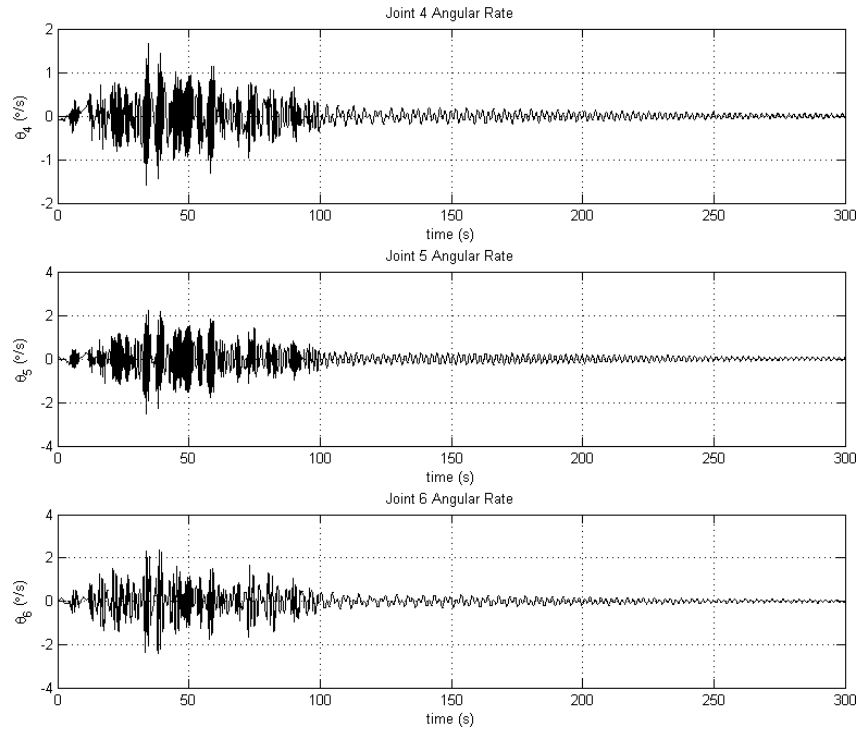


Figure 6.27: Joint angular velocities for the second solar array (SFB)

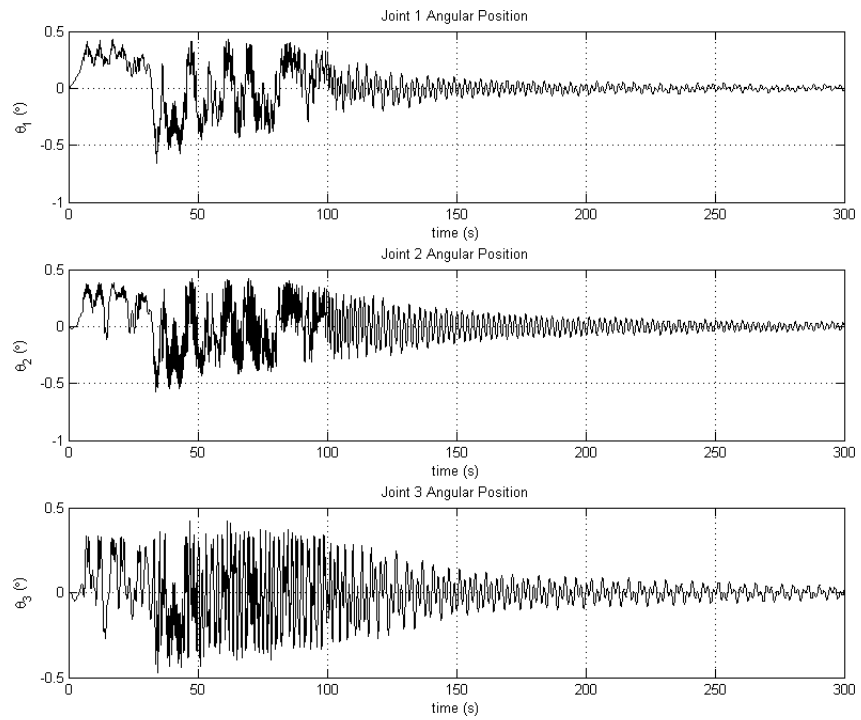


Figure 6.28: Joint angular positions for the solar array 1 (SFB)

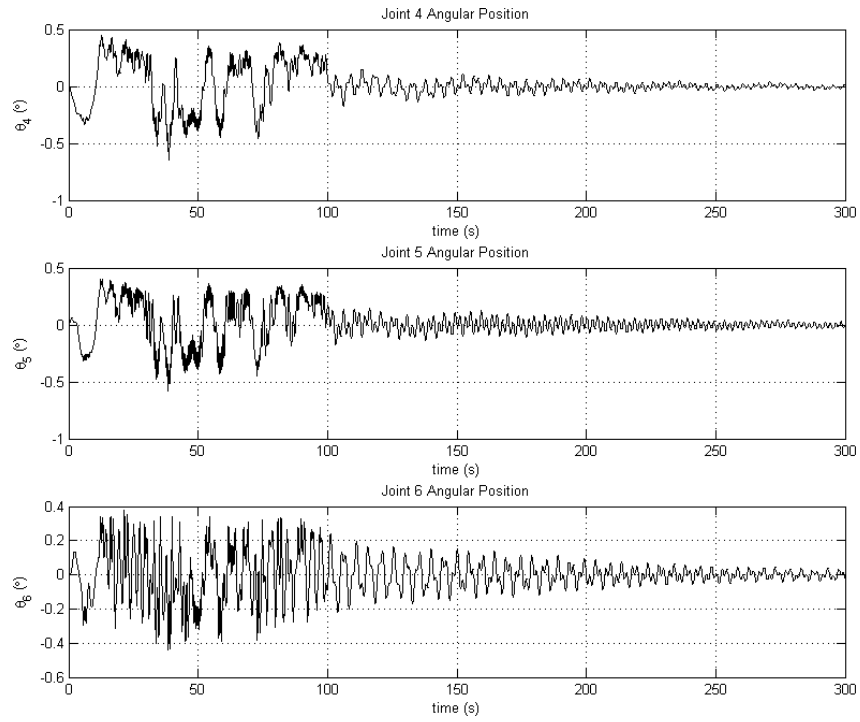


Figure 6.29: Joint angular positions for the solar array 2 (SFB)

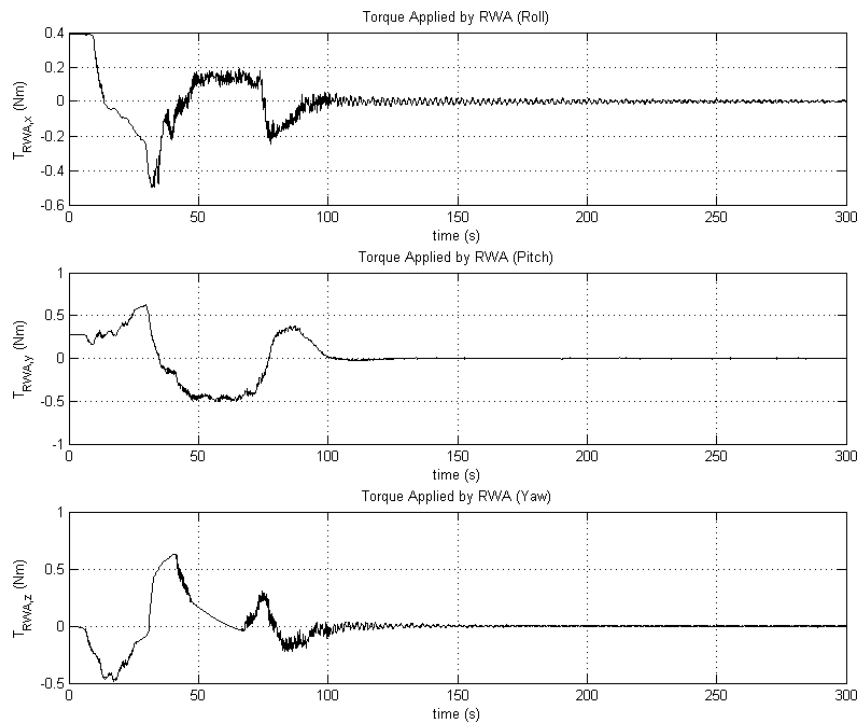


Figure 6.30: Actuator torque being applied on the satellite (SFB)

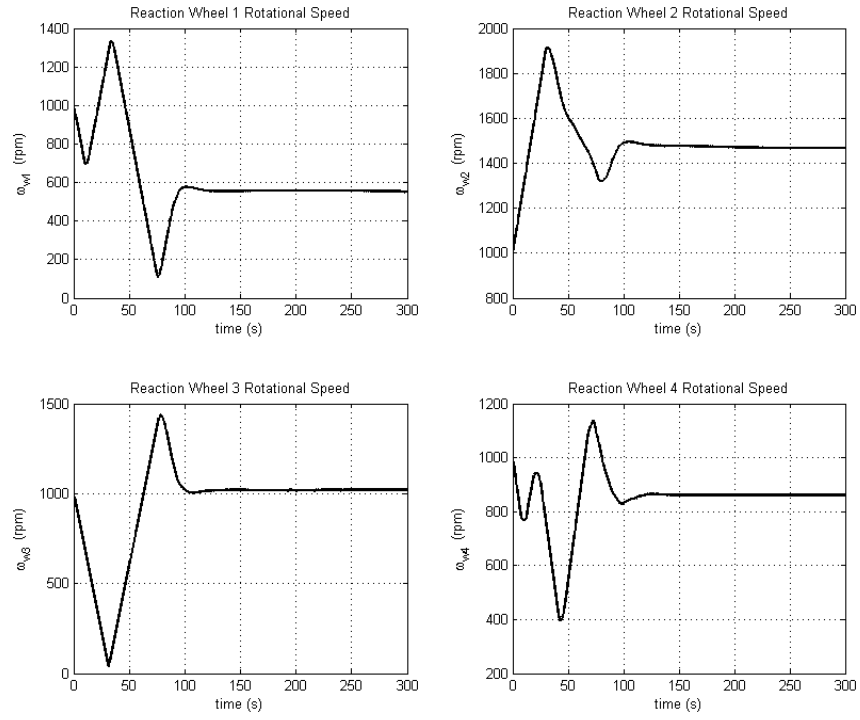


Figure 6.31: Reaction wheel angular velocities (SFB)

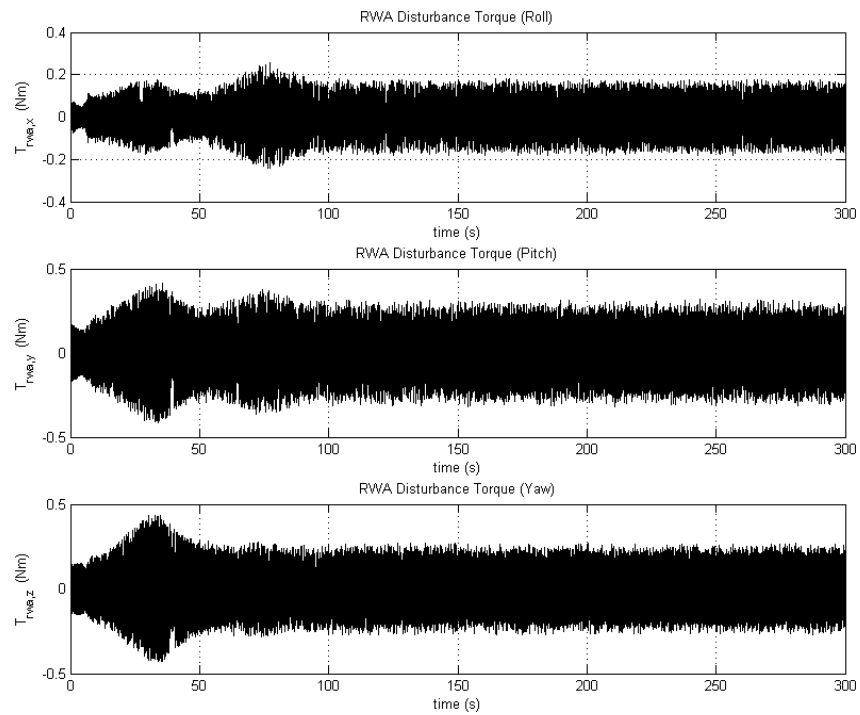


Figure 6.32: Disturbance torques due to reaction wheels acting on the satellite (SFB)

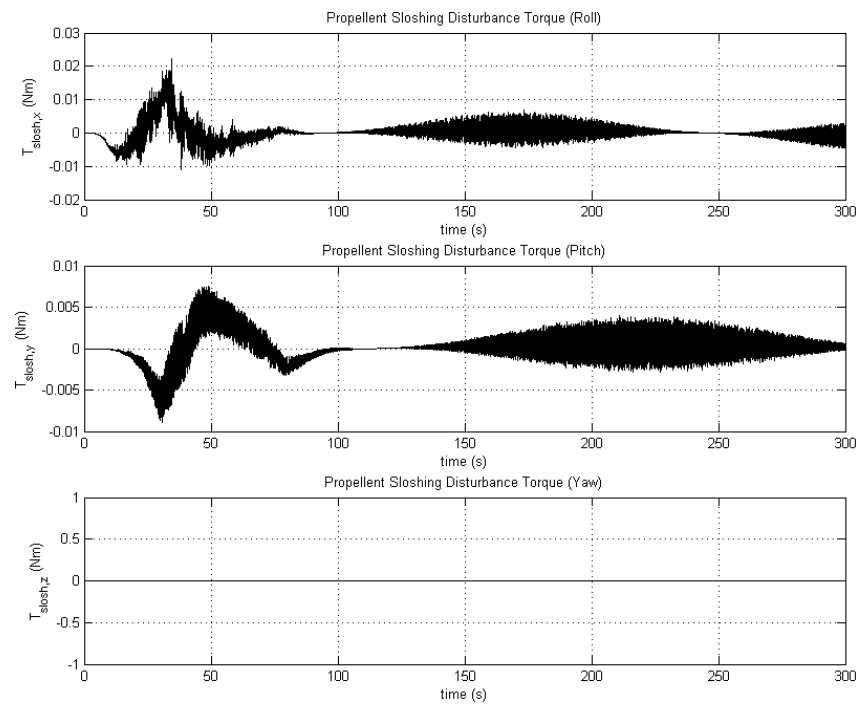


Figure 6.33: Disturbance torques due to propellant sloshing acting on the satellite (SFB)

### 6.3 Comparison of Results

Comparison of the results introduced in the previous section were made if categorized under the following subtopics.

*Attitude reorientation performance* Observing Figures 6.10 and 6.22, it may be noted that both of the controllers succeed in carrying out a slew maneuver and they both arrive at the vicinity of the target Euler angles around 100 s. However, SFB controller undergoes a higher overshoot especially in the yaw axis. Also, as observed from Figures 6.12 and 6.24, QFB undergoes severe angular accelerations when compared to SFB controller; especially after settling. Inspection of Figures 6.13 and 6.25 reveal that there is not significant difference in the settling attitude error for the two controller.

*Solar panel oscillations* By the inspection of Figures 6.14, 6.15, 6.26 and 6.27 containing plots of joint angle rates, it may be pointed out that SFB controller is more successful in attenuating oscillations than QFB controller. It is also noteworthy that there are no major differences in the magnitude of oscillations among solar arrays 1 and 2 as long as the same controller is concerned. Had the panels got different properties, this would not have been so. SFB controller proves its effectiveness in damping panel oscillations as it can be observed in Figures 6.16, 6.17, 6.28 and 6.29. When QFB controller is used, there exist oscillations and even collision with the hinge stops even after the spacecraft is settled in its new orientation.

*Pointing performance metrics* Comparing Tables 6.1 and 6.2, it may seem at the first glance that QFB controller has the upper hand in pointing accuracy and stability metrics. However, it must be pointed out that SFB controller had not undergone an extensive tuning process as QFB controller did. Additionally, SFB controller has a better jitter performance as expected from its oscillation damping ability.

*Control effort* Comparison of Figures 6.18 and 6.30 reveal that the control effort of QFB controller is much greater. It is likely that undamped oscillations stemming from propellant sloshing and solar panels contribute to the need of such high control effort in this case. Upon comparing Figures 6.19 and 6.31 reveals one critical shortcoming effecting both controllers; large angle slew maneuvers use much of the angular momentum capacity of reaction wheels (recall that wheel angular velocity saturation is at 2500 rpm). The extent of this is such that, the spacecraft will not able to perform another such large angle maneuver unless it dumps its



excess momentum.

*Disturbances* Observing Figures 6.20, 6.21, 6.32 and 6.33, it can be noted that disturbances is more severe for the QFB controller due the prevalence of oscillations that excite the sources of this disturbances.

## CHAPTER 7

### CONCLUSION

A complex spacecraft with appendages connected via flexible hinges was modeled by multi-body dynamics approach. Non-linearity of the hinge spring was also incorporated in the model. Detailed modeling of common spacecraft equipments such as star tracker, gyroscope and reaction wheels were also carried out, as well as the modeling of uncommon equipments such as proximity sensors. Both external and internal disturbances were included in the model. Internal disturbances were given a special emphasis due to their high magnitude, high frequency nature. Extensive modeling of propellant sloshing and reaction wheel static and dynamic imbalances were undertaken. Two different control schemes were implemented; Quaternion Feedback (QFB) Controller which provides ease of implementation and relatively complex State Feedback Controller (SFB). Pointing performance metrics were introduced in order to provide means of evaluation for the controller effectiveness. Defining a large angle slew maneuver scenario, performance of each controller was assessed.

It was found out that, QFB performs well despite its simplicity; attaining accuracies very close to that of SFB. However, it is not able to effectively attenuate the oscillations in appendages that result from the slew maneuver. On the other hand, SFB controller excels in damping the slew induced vibrations in solar panels. It was also found out that SFB controller spent less control effort when compared to the QFB controller. Thus, if a controller with an ease of implementation is required for an attitude control system of a satellite that does not house major flexible members, QFB controller scheme may be ideal. However, if that is not the case, implementing QFB would probably result in long term oscillations among the spacecraft flexible member after slewing maneuvers. It may also lead to rapid degradation of the actuator due to higher controller effort. On the opposite, if there exists a complex mission with minimum

allowance of appendage oscillations (such as astronomy or high-end earth observation missions); then the cost of adding proximity sensors can be justified and the implementation of the SFB scheme will become possible.

Another conclusion that can be drawn from this study is concerned with the internal disturbances. Reaction wheels and onboard fuel cause substantial amount of disturbance to spacecraft pointing. Mitigation of these disturbances are advised and encouraged. One temporary solution to reaction wheel vibration is reducing the wheel operating speed (whilst simultaneously avoiding the resonance frequencies of the satellite). Also, means of isolating these disturbance sources via using mountings with inherent damping is also possible.

## **7.1 Future Work**

From this point, several avenues for further research can be identified. These can be listed shortly as:

- Increasing the detail of the reaction wheel model. Modeling the reaction wheel together with its mounting which may involve inherent damping and flexibility
- Modeling another class of actuators; CMGs. Investigating the jitter characteristics of CMGs
- Determining other possible control schemes that may enhance the pointing performance. Comparing them with QFB and SFB.
- Much detailed modeling of propellant sloshing. Utilizing a three dimensional pendulum instead of several two dimensional ones in order to accurately represent the propellant sloshing in three dimensions
- Investigating methods that enable SFB to be implemented without the need for additional proximity sensors (estimation of panel joint positions)

## REFERENCES

- [1] L. C. Morena, K. V. James, J. Beck, "An introduction to the RADARSAT-2 mission", Canadian Journal of Remote Sensing, Volume 30, No. 3, June 2004, pp. 221-234
- [2] [http://directory.eoportal.org/get\\_announce.php?an\\_id=14767](http://directory.eoportal.org/get_announce.php?an_id=14767) (last accessed January 30, 2009)
- [3] [http://directory.eoportal.org/get\\_announce.php?an\\_id=8990](http://directory.eoportal.org/get_announce.php?an_id=8990) (last accessed February 1, 2009)
- [4] Allan Y. Lee et al, "Space Interferometry Mission Spacecraft Budget Pointing Error Budgets", IEEE Transactions on Aerospace and Electronic Systems, Vol. 38, No. 2, April 2002
- [5] Mark E. Pittelkau, "Definitions, Metrics, and Algorithms for Displacement, Jitter, and Stability", Flight Mechanics Symposium, NASA Goddard Space Flight Center, NASA/CP-2003-212246, 28-30 October 2003
- [6] David S. Bayard, "A Simple Analytic Method for Computing Instrument Pointing Jitter", JPL (internal document), JPL D-19967, November 2000
- [7] Tooraj Kia, David S. Bayard, Fernando Tolivar, "A Precision Pointing Control System for the Space Infrared Telescope Facility (SIRTF)", Advances in the Astronautical Sciences: Guidance and Control, Volume 94, AAS 97-067, 1997
- [8] Brij Agrawal, "Jitter Control for Imaging Spacecraft", 4th International Conference on Recent Advances in Space Technologies, 11-13 June 2009, Istanbul, Turkey
- [9] Bong Wie, "Space Vehicle Dynamics and Control", AIAA Education Series, Reston, VA, 1998
- [10] John L. Junkins, "Introduction to Dynamics and Control of Flexible Structures", AIAA Education Series, Reston, VA, 1993
- [11] Peter C. Hughes, "Spacecraft Attitude Dynamics", Dover Publications, 2004
- [12] Eric Stoneking, "Newton-Euler Dynamic Equations of Motion for a Multi-Body Spacecraft", AIAA GNC Conference, 20-23 Aug. 2007, Hilton Head, SC, United States
- [13] Marcel J. Sidi, "Spacecraft Dynamics and Control: A Practical Engineering Approach", 1st Edition, Cambridge University Press, New York, 2006
- [14] James R. Wertz, "Spacecraft Attitude Determination and Control", Kluwer Academic Publishers, Netherlands, 1990
- [15] Katshiko Ogata, "Modern Control Engineering", 4th Edition, Prentice Hall, New Jersey, 2001

- [16] Emre Yavuzoglu, "Steering Laws for Control Moment Gyroscope Used in Spacecraft Attitude Control", MS Thesis, Aerospace Engineering Department, Middle East Technical University, Ankara, Turkey, November 2003
- [17] Rafal Wisniewski and Piotr Kulczycki, "Slew Maneuver Control of Spacecraft Equipped with Star Camera and Reaction Wheels", *Control Engineering Practice*, Vol. 13, Issue 3, March 2005, Pages 349-356, Aerospace IFAC 2002
- [18] H. P. Aeby et al, "High Resolution Standard Proximity Sensor", *ESA Special Publication*, Pages 343-346, 2001
- [19] Charles D. Brown, "Elements of Spacecraft Design", *AIAA Education Series*, Reston, VA, 2002
- [20] <http://www.colorado.edu/intphys/Class/IPHY3730/image/figure8-28.jpg> (last accessed August 25, 2009)
- [21] Aykut Kutlu, "Design of Kalman Filter Based Attitude Determination Algorithms of a LEO Satellite and for a Attitude Control Test Setup", MS Thesis, Aerospace Engineering Department, Middle East Technical University, Ankara, Turkey, September 2008
- [22] Shigemune Taniwaki and Yoshiaki Ohkami, "Experimental and Numerical Analysis of Reaction Wheel Disturbances", *JSME International Journal Series C*, Vol. 46, No. 2 (2003), Pages 519-526
- [23] Rebecca A. Masterson, "Development and Validation of Empirical and Analytical Reaction Wheel Disturbance Models", MS Thesis, Department of Mechanical Engineering, Massachusetts Institute of Technology, Cambridge, MA, June 1999
- [24] IRD Balancing, "Balance Quality Requirements of Rigid Rotors: The Practical Application of ISO 1940/1", Rev. 2, IRD P/N E51267, 2009
- [25] Bong Wie and Peter M. Barba, "Quaternion Feedback for Spacecraft Large Angle Maneuvers", *Journal of Guidance, Control, and Dynamics*, 1985, 0731-5090 vol.8 no.3 (360-365)
- [26] Roland S. Burns, "Advanced Control Engineering", Butterworth-Heinemann, Oxford, 2001

## APPENDIX A

### SIMULINK MODELS

#### A.1 Simulink Model with Quaternion Feedback Controller

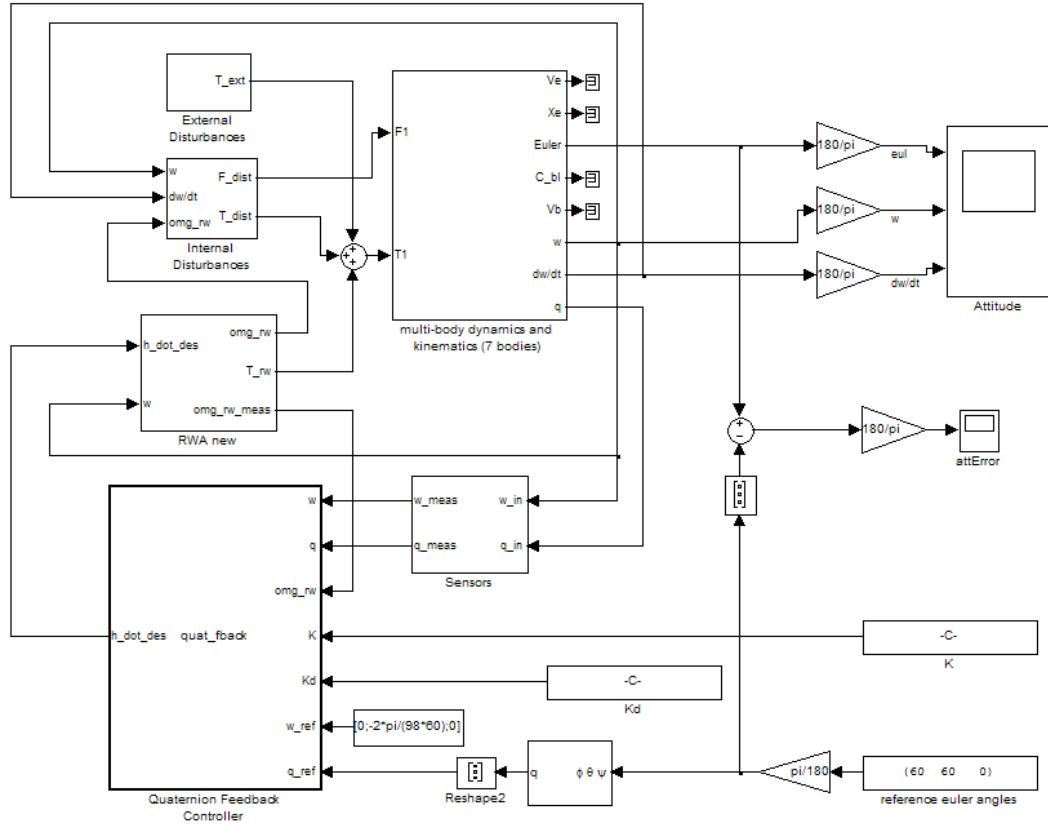


Figure A.1: Simulink model for multi-body satellite with QFB controller

## A.2 Simulink Model with State Feedback Controller

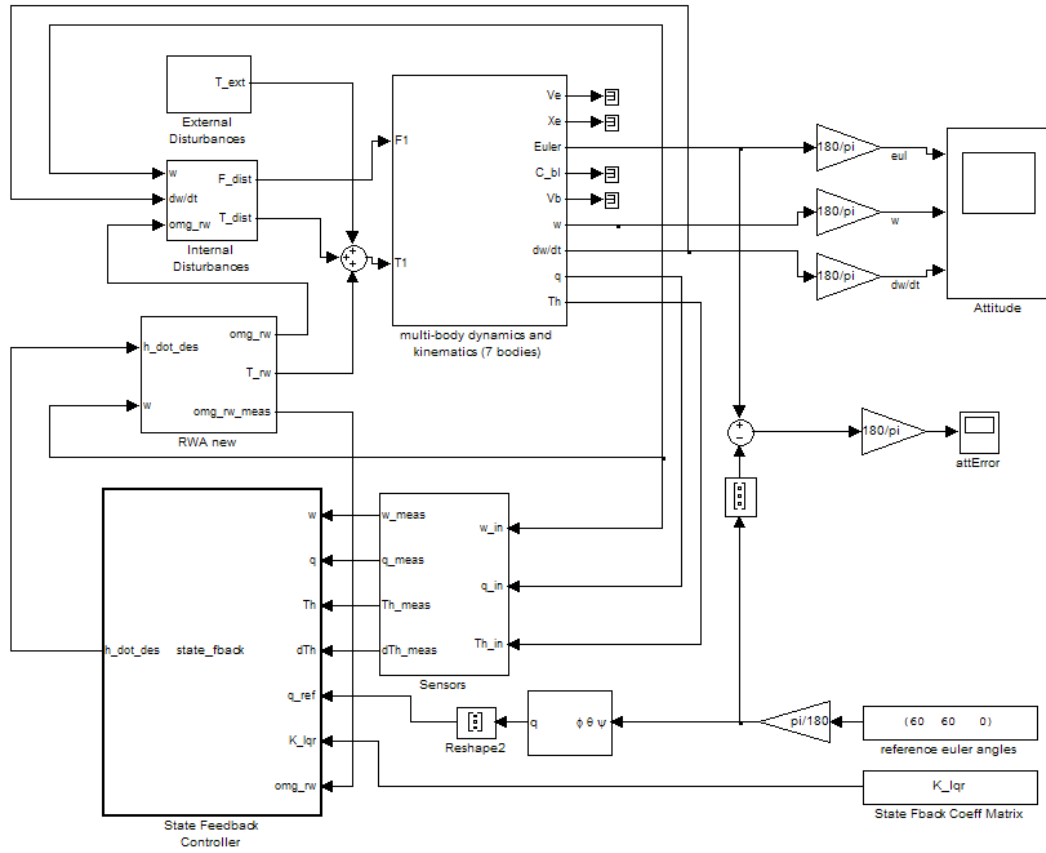


Figure A.2: Simulink model for multi-body satellite with SFB controller